ABSTRACT

HASAN, TAMIR SAFA. Microstructural Predictions of Crack Nucleation and Failure in Multiphase Materials Using Statistical and Machine Learning Methods. (Under the direction of Professor Mohammed A. Zikry).

The exposure of crystalline aggregates, such as zirconium alloys, to hydrogen can lead to hydride precipitation. Zirconium alloys are widely used in critical environments characterized by high temperatures, corrosive degradation, and radiation exposure. They are an important part of nuclear infrastructure, forming the cladding material within which reactive materials are housed. These alloys thermo-mechanically degrade due to hydride formation when exposed to harsh operating environments. The complex distribution of hydrides and their interaction with defects, such as populations of dislocations, play a significant role in crack nucleation and material failure.

To accurately model these materials at different physical scales, it is necessary to fully characterize them according to their material "fingerprint"–a combination of factors involving hydride geometry, parent material orientation, and the microstructure of these multiphase alloys that affect material behavior. Hence, this investigation will develop a reduced order modeling (ROM) approach, where a microstructural fingerprint is used to define critical fracture stress levels that are physically consistent with material fracture. 210 crystal plasticity finite element (FE) simulations based on a deterministic fracture model coupled to a dislocation-density based crystalline plasticity approach were used to develop a material database of crack initiation for a broad array of microstructural characteristics, including hydride volume fraction, hydride and matrix orientation, hydride length, and hydride spacing. These material parameters were sampled using Morris trajectories. This database was then mined to develop low-dimensional representations of extreme behavior using Extreme Value Theory (EVT).

Using this database, a Bayesian approach and Gaussian Process Regression (GPR) were then used to derive ROMs predicting the probability of crack nucleation. The proposed methodology provides a Bayesian-based framework for quantifying the likelihood of crack nucleation within hydrided zirconium alloys and is then used to investigate crack nucleation mechanisms at the microstructural scale. The predictions indicate that fracture probability is significantly influenced by hydride orientation and differences between dislocation densities in the hexagonal close packed (hcp) matrix and the face centered cubic (fcc) hydrides, and this affects ductility, fracture nucleation, and crack propagation. More generally, this approach can also be applied to predict failure in multiphase materials at different physical scales ranging from the nano to the macro.

Various methodologies were also used to describe the extreme components of fracture critical stress evolution within hydrided zirconium alloy materials based on the microstructural fingerprint. Multilayer perceptrons (MLP), or neural networks, provided the highest accuracy on held-out test sets across three predetermined strain levels of interest. These models were used to determine the relative importance of the five material fingerprint parameters. Hydride orientation, material orientation or texture, and hydride volume fraction had the greatest impact on fracture critical stress levels and had partial dependencies that were highly significant. These predictions indicated that hydride length and hydride spacing have less effect on predicted fracture probabilities.

Furthermore, the spatially dependent material response in the regions directly adjacent to the hydrides at the matrix-hydride interfaces was characterized using fat-tailed Cauchy distributions to obtain descriptors of the extreme events occurring in proximity to the hydrides. An MLP was found to be effective in learning the characteristics of the localized spatially dependent material response to predefined strain levels. The locations of fracture critical stress accumulation with respect to each hydride varied based on hydride and material orientation. Hydride volume fraction, a population-level parameter, had a significant impact on the local response, such as the width of the fracture critical stress distribution and on the accumulated immobile dislocation densities. Finally, the driving forces for these phenomena were identified by studying the dislocation-density response both within and external to the hydrides.

These interrelated machine learning approaches provide a verified framework that can be used to predict fracture nucleation and propagation for multiphase materials by identifying dominant microstructural mechanisms, such as dislocation-densities and hydride orientations, and can provide new fundamental predictive methodologies for material failure.

Microstructural Predictions of Crack Nucleation and Failure in Multiphase Materials Using Statistical and Machine Learning Methods

by
Tamir S. Hasan

A dissertation submitted to the Graduate Faculty of
North Carolina State University
in partial fulfillment of the
requirements for the degree of
Doctor of Philosophy

Mechanical Engineering

Raleigh, North Carolina
2022

APPROVED BY:

Professor Mohammed Zikry
Committee Chair

Professor Jeffrey Eischen

Professor Larry Silverberg

Professor Ralph Smith

BIOGRAPHY

Tamir Hasan was born in Linköping, Sweden on April 13, 1991. He grew up in Champaign-Urbana, Illinois and Concord, North Carolina. He graduated from the North Carolina School of Science and Mathematics in May 2009. Tamir attended North Carolina State University for his undergraduate and masters studies in Mechanical Engineering. As an undergraduate, Tamir interned with G.E. Aviation, RTI International, and Underwriters Laboratories. He also volunteered as a firefighter and EMT. After graduating from North Carolina State University in 2015, Tamir was employed by Eaton Corporation in the Engineering and Technology Leadership Development Program. There, he gained engineering design and operational experience in the aerospace and automotive industries while working in Kalamazoo, Michigan; Beltsville, Maryland; and Kings Mountain, North Carolina.

In August 2018, Tamir continued his graduate studies at North Carolina State University under the direction of Dr. Mohammed Zikry. His research focused on using the finite element method to investigate crystalline plasticity in zirconium-based multiphase systems. As part of a collaborative research effort through the Department of Energy, he worked at Los Alamos National Laboratory to pursue this research. The research related to this dissertation has generated the following research papers and proceedings:

T.S. Hasan, L. Capolungo, M.A. Zikry (2022). “Predictions of Crack Nucleation and Failure Using a Bayesian Microstructurally Predictive Framework.” Submitted.

T.S. Hasan, L. Capolungo, M.A. Zikry (2022). “Predictions of Material Response in Hydrided Zirconium Alloys.” To be submitted.

T.S. Hasan, L. Capolungo, M.A. Zikry (2022). “Machine Learning Predictions of Representative Hydride Distributions of Strain Responses in Zirconium Alloys.” To be submitted.

T.S. Hasan, L. Capolungo, M.A. Zikry (2022). "Predictions of Crack Nucleation and Failure in Multiphase Materials Using Statistical and Machine Learning Methods." *8th European Congress on Computational Methods in Applied Sciences and Engineering*.

T.S. Hasan, M.A. Zikry (2022). "Statistical Predictions of Failure in Hydrided Zirconium Materials." *The Minerals, Metals, and Materials Society*.

I. Mohamed, **T.S. Hasan**, and M.A. Zikry (2021). "Thermomechanical Predictions of Fracture Nucleation of Zircaloy-4 Alloys with δ and ε Hydride Distributions." *ASME Journal of Engineering Materials and Technology*.

T.S. Hasan, M.A. Zikry (2021). "The Thermo-Mechanical Fracture of Chromium-Zirconium Systems." *The Minerals, Metals, and Materials Society*.

T.S. Hasan, M.A. Zikry (2020). "The Thermo-Mechanical Fracture of Chromium Film-Zirconium Substrates." *Consortium for Advanced Simulation of Light Water Reactors Meeting*.

T.S. Hasan, M.A. Zikry (2020). "The Thermo-Mechanical Fracture of Chromium Film-Zirconium Substrates." *American Nuclear Society Winter Meeting*.

ACKNOWLEDGMENTS

I would like to acknowledge my family, friends, and colleagues who have supported me throughout my professional and educational endeavors. Special thanks to my parents, for their enthusiasm in my graduate pursuits; to Ali, for trying his hardest to explain novel and interesting concepts to me; and to Tiff, for endless support and encouragement.

Much gratitude goes to Dr. Mohammed Zikry for never faltering in believing in me, even after a decade, and for his guidance and support. Through the NCSU-LANL NEUP, I was able to collaborate with Dr. Laurent Capolungo. His insights, discussions, and advice were invaluable in advancing this project and publications. I look forward to continued collaboration with him. I would also like to thank my committee members: Dr. Jeffrey Eischen, Dr. Larry Silverberg, and Dr. Ralph Smith for their valuable comments and feedback. Additionally, many thanks to my coworkers for making the lab a welcoming and supportive place: Dr. Darrell LaBarbera, Dr. Letisha Lam, Dr. Judith Brown, Dr. Qifeng Wu, Dr. Bingxiao Zhao, Dr. Shoayb Ziaei, Dr. Matt Bond, Dr. Ismail Mohamed, Dr. Mohamed Elbadry, Muh-Jang Chen, and Matt Phillips. Special thanks to Dr. Darrell LaBarbera for patiently teaching me how to use Crystal2D.

Support from the Consortium for Advanced Simulation of Light (CASL) Water Reactors, an Energy Innovation Hub for Modeling and Simulation of Nuclear Reactors, U.S. Department of Energy, Contract No. DE-AC05-00OR227 and the DOE NEUP Integrated Research Project IRP-17-13708, Development of a Mechanistic Hydride Behavior Model for Spent Fuel Cladding Storage and Transportation is also gratefully acknowledged.

TABLE OF CONTENTS

LIST OF TABLES

LIST OF FIGURES

CHAPTER 1: Introduction

1.1 Overview

Zirconium alloys play a significant role as cladding and protective layers for high temperature applications, such as nuclear reactors, hypersonic systems, and marine systems. In nuclear reactors, they are used as cladding for uranium, where exposure to high temperature heavy water can cause defects caused by hydrogen accumulation within the microstructure [1], [2]. These alloys are generally corrosion resistant at high temperatures, possess favorable high-temperature mechanical characteristics, and are resistant to irradiation. However, during service, zirconium alloys can thermo-mechanically degrade through the formation of hydrides due to high temperature water exposure and long-term storage [1], [3], [4] and during loss-of-coolant accidents (LOCA) [5] for nuclear applications. The chemical reaction describing the interaction of zirconium alloys with steam resulting in the generation of hydrogen is given by:

$$Zr + 2H_2O \rightarrow ZrO_2 + 2H_2 \qquad 1.1$$

Some of the hydrogen generated by this reaction then precipitates into the zirconium alloy matrix and forms hydrides. These defects have been shown to negatively impact various material properties of the zirconium alloys including ultimate tensile stress, ductility, and cracking strain [6], [7]. Furthermore, these hydrides have different crystalline structures than the parent zirconium alloy [8], which renders these material systems as multiphase and heterogenous. Hydrides of the δ classification form with a face centered cubic (fcc) crystal structure within a hexagonal close packed (hcp) matrix defined by the zirconium alloy.

Critically, hydride orientation, morphology, distribution, texture, crystalline structures, spacing, and dislocation-densities all have interrelated effects on thermo-mechanical behavior at scales ranging from the nano to the micro [9]–[11], and collectively affect fracture nucleation and propagation [8]–[10]. Experimental literature has shown that zirconium alloys are significantly degraded due to hydride formation [8], [12]. Hydride nucleation has been found to occur differently based on temperature exposure levels and time [13]–[15]. The resulting hydrides have a wide range of geometric orientations, typically expressed as radial, circumferential, or mixed, based on the orientation of their longest axis with respect to the cladding tube. The impact of hydrides on material properties has been shown to change based on the orientation of the hydrides [14], [16]. Hsu *et al.* [11] investigated fracture toughness on thin-walled tubing for different temperatures. They determined that hydride orientation, hydrogen content, and temperature were all factors influencing fracture toughness in hydrided zirconium alloys. They concluded that the presence of radial hydrides reduces the fracture toughness at room temperature when compared with distributions of circumferential hydrides, with J_{max} values of pure circumferentially hydrided samples up to 40 kJ/m^2, and values for samples with 52.2% radial hydrides as low as 11 kJ/m^2. [11]. Kim *et al.* performed ring compression tests (RCTs) on both circumferentially and radially hydrided zirconium alloys. Their results indicate that radially oriented hydrides are more likely to fracture than circumferentially oriented hydrides because of the favorable crack propagation pathways associated with radial hydride arrangements [17]. Experiments by Pierron *et al*. [18] show that grain elongation associated with cold working had little impact on fracture toughness. They also observed void nucleation ahead of a crack in a hydrided material, which indicates that voids can be sites of multiple ductile crack nucleation regions, and this eventually can lead to crack propagation and material rupture [18]. Hydride lengths and hydride spacing have also been shown to affect fracture strengths. For lengths of less than 25 μm, ultimate tensile stresses in the in Zr-2.5Nb alloys can decrease by approximately 1.4 MPa for every 1 μm increase in average hydride length [6]. These results show that hydrides significantly impact the bulk material response, and that the variation of microstructural characteristics plays a significant role in material failure.

Other approaches for understanding the relationship between hydride behavior and fracture have focused on Delayed Hydride Cracking (DHC) [19], [20]. DHC occurs when hydrogen slowly diffuses to a preexisting crack tip region, thereby resulting in crack propagation. Hydride formation at preexisting crack tips leads to further fracture growth after a delay due to the steadily increasing presence of the formed hydrides at the crack tip. Shi and Puls found that the size and shape of the hydrides precipitated at the crack tip impacted the stress intensity factor, and thereby crack propagation [20]. Studies of fracture in hydrided materials have shown that hydrides tend to cause brittle failure at temperatures below 100°C, with the surrounding matrix exhibiting ductile failure [9] . Sharma *et al*. [21] investigated the fracture behavior of hydrided zirconium alloy tubing material using mechanical testing. They were able to change the hydride morphology by annealing a system with 100% radial hydrides. Varying the annealing temperature between 300°C, 325°C, and 350°C influenced the percentage of circumferential hydrides. Their findings indicate that a fully circumferentially hydrided material has more than four times higher critical crack length when compared with a fully radially hydrided material, at room temperature. At higher temperatures (250°C and above), the radially hydrided critical crack length increases to match that of the circumferential material. This indicates that the greatest variation between the fracture response of circumferential and radial hydrided materials occurs at room temperature or lower. They also found that fracture toughness was reduced with the formation of hydrides, and even more so in the case of radial hydride formation, with approximately an 80% reduction in the case of 100% radial hydrides when compared with circumferential hydrides.

In [22], fracture toughness in Zircaloy-4 sheet was experimentally shown to decrease as hydrogen content increased, and as the proportion of radially oriented hydrides increased. Higher temperatures were found to reduce the tendency for crack propagation within the material. Studies of fatigue in hydrided zirconium alloys have also shown a strong preference on microcrack formation in radially oriented hydrides [23].

These experiments provide a characterization of bulk material characteristics but lack a full understanding and quantification of microstructural characteristics, such as how texture and defects like dislocation-densities affect failure nucleation and evolution. Furthermore, most of these experimental investigations pertain to crack propagation in systems with preexisting cracks as opposed to crack nucleation in hydrided systems, since crack nucleation is difficult, if not impossible, to experimentally quantify. Thus, modeling efforts can provide further insights into fundamental fracture mechanisms.

Simulations of hydrided materials have been performed at various length scales, with phase field modeling (PPM) and density functional theory (DFT) used at atomic and meso length scales to study hydride formation [24], reorientation [25], embrittlement [26], and their effects on crack propagation. Finite element method (FEM) models are used at larger length scales from microstructural to the macro. Liu et al. examined a component level model informed by grain-scale simulations of hydrides and found that a linking effect between individual hydrides influenced fracture crack paths and material failure [27]. Therefore, it is necessary to examine populations of hydrides to fully understand their impact on larger scale systems. In [28], finite element (FE) models were used to understand how hydrogen embrittlement affects cracking and DHC for pre-cracked materials. Jernkvist [29] also investigated DHC for pre-cracked or notched zirconium and titanium alloys for different hydride orientations and volume fractions. Suman

[30] investigated the impact of crack and hydride lengths on crack propagation in simulated DHC. While these studies have provided valuable insights, the links between dislocation activity and fracture nucleation have not yet been understood. Other insights were provided from Olsson *et al.* [31], where fracture toughness was modeled with an ab initio-based approach using density functional theory (DFT). Their findings indicated that increasing hydrogen content reduced ductility by inhibiting dislocation nucleation. This provides a foundation on which to base larger scale fracture simulations. While these approaches all provide valuable insights, a comprehensive deterministic modeling approach that incorporates microstructural variation and can predict the impact of dislocation-densities on fracture at the microstructural scale is needed to provide insights and understanding of fracture nucleation that account for intergranular and transgranular failure. Furthermore, the question of how to obtain statistical information pertaining to deterministic fracture models has not yet been addressed.

As these various experimental and computational investigations indicate, the thermo-mechanical fracture behavior of hydrided zirconium alloys is dominated by the microstructural "fingerprint": hydride orientation, material orientation, grain morphology, texture, and hydride volume fraction. In addition to the material fingerprint, defects such as dislocation densities can collectively affect multiple crack nucleation and failure. Deterministic models have provided insightful understanding of how fracture at the microstructural scale leads to failure [cf. 19,20], but they have not yet yielded a comprehensive and quantitative description of microstructure-induced epistemic uncertainty.

Different statistical and machine learning (ML) methods have also been used to model material characteristics derived from deterministic models and experiments. Regression neural networks and reduced ordered models (ROMs) have been used to represent inelastic deformation in crystals. Defect models, such as dislocations and cracks, can be used to guide predictions of material response for different loading conditions [34]. One advantage of creating ROMs for material models is the ability to use the resulting insights with limited computational cost for larger scale simulations. For example, models predicting failure should account for local variabilities among material properties and behavior, in addition to geometrical effects. Hunter demonstrated the use of multilayer perceptrons (MLP; neural networks) on a dataset based on FE element simulations of a simple homogenous and elastic block-like material with pre-existing cracks [35]. Other approaches have attempted a more direct path of using deep learning methods to predict stress and other material properties when given a purely spatial input of stresses, strains, elastic strains, and plastic strains. These methods have shown promise in simplifying models related to the elastic solution of beam and plates [36], [37]. These methods alone, however, have not been used to obtain statistically significant predictions for complex material systems that span multiple physical scales, such as hydrided systems.

1.2 General Objectives

The objective of the present work is to characterize the material response of hydrided zirconium alloys, in particular Zircaloy-4, and to understand the microstructural characteristics that result in fracture at different physical scales. Due to the highly parametric nature of adequately characterizing these multiphase crystal structures, it is difficult or impossible to perform this work using experimental methods, especially because crystallographic characterization can only occur in the material's damaged post-testing state. Experimental studies additionally do not provide real time insight into dislocation behavior across all slip systems. These difficulties are compounded by the examination of a heterogeneous multiphase crystal structure. Other simulation techniques, such as molecular dynamics or phase field modeling, do not capture the large nonlinear deformation associated with material fracture while also maintaining insight into the inner workings of the crystal structures, such as dislocation density accumulation.

Therefore, in this work, the basis of the analysis will be a series of nonlinear finite element models with a multiple slip dislocation density based crystalline plasticity formulation and an advanced fracture nucleation and propagation model. A large database of simulations will be developed to characterize the multiphase hcp/fcc crystal structure of hydrided zirconium alloys. The components of this database will be material simulations with varying material "fingerprints", each describing a unique set of material and crystallographic properties. A method combining extreme value theory (EVT) and Bayesian analysis will be used to train Gaussian Process Regression (GPR) models describing the likelihood of fracture in localized material regions. Models developed to describe the extreme components of the material response will be interrogated to determine the relative importance of each parameter comprising the material fingerprint.

Finally, the interactions between the hcp matrix zirconium and the fcc hydrides will be examined more explicitly by examining the simulated regions directly adjacent to the hydrides using fat-tailed distributions to describe the material response in spatial terms. Models predicting distributions of fracture critical stress and shear slip in the hydride-adjacent regions will be developed, and the model output will be examined to learn about the impact that bulk material properties have on the hydride-adjacent regions and to provide insight to the expected range of properties in the hydride-adjacent regions.

1.3 Dissertation Organization

This dissertation is organized as follows: Chapter 2 presents the multiple-slip, dislocation density-based crystalline plasticity formulation, dislocation density evolution, thermo-mechanical coupling, orientation relations describing the interface between the zirconium alloy matrix and hydrides, the computational approach for dislocation density-based crystalline plasticity, and the methods used for fracture nucleation and propagation. Chapter 3 develops an extreme value representation of the simulated materials and expresses the likelihood of fracture using a Bayesian approach. The link from dislocation activity on individual slip systems to the probability of failure is developed. Chapter 4 investigates the importance of each material parameter by developing and interrogating models describing the variation of fracture critical stress given a set of material properties. Chapter 5 explores the interactions between the fcc hydrides and hcp matrix material by examining the areas directly adjacent to the hydrides and within the hydrides. Chapter 6 develops new models for systems of chromium-coated zirconium alloys and examines the conditions at the interface between the coating and the alloy that lead to fracture. Finally, recommendations for future research are given in Chapter 7.

CHAPTER 2: Numerical Method and Fracture Approach

2.1 Multiple Slip Plasticity Formulation

The dislocation-density crystalline approach used in the present work was developed by Asaro and Rice [38], Zikry [39], Zikry and Kao [40] and Shanthraj and Zikry [41]. The deformation gradient F_{ij} is used to calculate the velocity gradient tensor V_{ij}:

$$V_{i,j} = \dot{F}_{ij} F_{ij}^{-1} \tag{2.1}$$

This velocity gradient is decomposed into a symmetric deformation rate tensor (D_{ij}) and the anti-symmetric spin tensor (W_{ij}):

$$V_{i,j} = D_{ij} + W_{ij} \tag{2.2}$$

$$D_{ij} = \frac{1}{2}(V_{i,j} + V_{j,i}) \tag{2.3}$$

$$W_{ij} = \frac{1}{2}(V_{i,j} - V_{j,i}) \tag{2.4}$$

These tensors are in turn decomposed into elastic (^{e}) and plastic (^{p}) components:

$$D_{ij} = D_{ij}^{e} + D_{ij}^{p} \tag{2.5}$$

$$W_{ij} = W_{ij}^{e} + W_{ij}^{p} \tag{2.6}$$

where W_{ij}^{e} included rigid body spin. Shear slip rate $\dot{\gamma}$ is a measure of the accumulated plastic strain on a material that is related to the mobile dislocation activity in a material. It is used to define the plastic components of the deformation rate tensor D_{ij}^{P} and the spin tensor W_{ij}^{P} as follows:

$$D_{ij}^{P} = P_{ij}^{(\alpha)} \dot{\gamma}^{(\alpha)} \tag{2.7}$$

$$W_{ij}^{P} = \omega_{ij}^{(\alpha)} \dot{\gamma}^{(\alpha)} \tag{2.8}$$

where (α) indicates the summation over all slip systems and P and ω are the directions of deformation and spin with respect to an individual slip system. These tensors are defined in terms of slip plane normal unit vectors ($n_i^{(\alpha)}$) and slip plane direction unit vectors ($s_i^{(\alpha)}$) as:

$$P_{ij}^{(\alpha)} = \frac{1}{2}\left(s_i^{(\alpha)} n_j^{(\alpha)} + s_j^{(\alpha)} n_i^{(\alpha)}\right) \tag{2.9}$$

$$\omega_{ij}^{(\alpha)} = \frac{1}{2}\left(s_i^{(\alpha)} n_j^{(\alpha)} - s_j^{(\alpha)} n_i^{(\alpha)}\right) \tag{2.10}$$

The plastic component of the deformation rate tensor is used to calculate the effective plastic shear slip, representing the accumulation of plastic shear strain over time:

$$\gamma_{eff} = \frac{2}{3}\int \sqrt{D_{ij}^{p} D_{ij}^{P}} dt \tag{2.11}$$

To obtain a rate-dependent formulation, a power law formulation is used whereby the slip rates depend on the resolved shear stresses and the reference stress of the solid:

$$\dot{\gamma}^{(\alpha)} = \dot{\gamma}_r^{(\alpha)} \left[\frac{\tau^{(\alpha)}}{\tau_r^{(\alpha)}}\right] \left[\frac{\left|\tau^{(\alpha)}\right|}{\tau_r^{(\alpha)}}\right]^{\frac{1}{m}-1} \tag{2.12}$$

where $\tau^{(\alpha)}$ is the resolved shear stress on slip system α, $\dot{\gamma}_r^{(\alpha)}$ is the reference shear strain corresponding to the reference shear stress $\tau_r^{(\alpha)}$, and m is the strain rate sensitivity parameter, defined as:

$$m = \frac{\partial \ln \tau^{(\alpha)}}{\partial \ln \dot{\gamma}^{(\alpha)}} \tag{2.13}$$

The formulation for the reference shear stress $\tau_r^{(\alpha)}$ is a modification of other classical forms [42] and links reference stress to immobile dislocation density ρ_{im}:

$$\tau_{ref}^{(\alpha)} = \left(\tau_y^{(\alpha)} + G \sum_{\beta=1}^{nss} b^{(\beta)} \sqrt{a_{\alpha\beta} \rho_{im}^{(\beta)}}\right) \left(\frac{T}{T_0}\right)^{-\xi} \tag{2.14}$$

where $\tau_y^{(\alpha)}$ is the static yield stress on slip system α, G is the shear modulus, nss is the number of slip systems in the material system, $b^{(\beta)}$ is the magnitude of the Burger's vector, and $a_{\alpha\beta}$ are Taylor coefficients related to the strength of interactions between slip systems [43]. The Taylor coefficients are obtained using Frank's rule for determining energetically favorable interactions for immobile dislocation density junction formulation [41]. The impact of temperature on the reference shear stress is also considered, and the stress is modified by the ratio of the current temperature T to the reference temperature T_0 (293 K), raised to the thermal softening exponent ξ.

2.2 Dislocation Density Evolution

Following the approach of Zikry and Kao [40], it is assumed that, for a given deformed state of the material, the total dislocation-density of a particular slip system α, ρ^{α}, can be additively decomposed into a mobile and an immobile dislocation-density, ρ_m^{α} and ρ_{im}^{α}.

$$\rho^{(\alpha)} = \rho_m^{(\alpha)} + \rho_{im}^{(\alpha)} \qquad 2.15$$

Based on a conservation of mass for mobile and immobile dislocation densities, during an increment of strain on a slip system, a mobile dislocation-density rate is generated, and an immobile dislocation-density rate is annihilated [41]. Furthermore, the mobile and immobile dislocation-density rates can be coupled through the formation and destruction of junctions as the stored immobile dislocations act as obstacles for evolving mobile dislocations. These coupled differential equations are:

$$\dot{\rho}_m^{(\alpha)} = \dot{\rho}_{generation}^{(\alpha)} - \dot{\rho}_{interaction-}^{(\alpha)} \qquad 2.16$$

$$\dot{\rho}_{im}^{(\alpha)} = \dot{\rho}_{interaction+}^{(\alpha)} - \dot{\rho}_{annihilation}^{(\alpha)} \qquad 2.17$$

where $\dot{\rho}_{generation}^{(\alpha)}$ is the mobile dislocation density rate that is generated and $\dot{\rho}_{annihilation}^{(\alpha)}$ represents the annihilation rate of immobile dislocation densities. $\dot{\rho}_{interaction}^{(\alpha)}$ is the coupling term between immobile and mobile dislocation densities, and the + identifier is related to the formation of junctions and the – identifier is related to the annihilation of junctions.

Evolution equations for mobile and immobile dislocation densities can then be obtained by considering the generation, interaction, immobilization, and annihilation of dislocation densities. These equations are dependent on the plastic deformation rate and inform the evolution of mobile and immobile dislocation densities. The mobile dislocation density generation rate is related to the distance traversed, y_{back}, by an emitted dislocation from an immobile forest obstacle source with a density of ρ_{source}. The generation rate is determined using the ratio of the average velocity of mobile dislocations, $v^{(\alpha)}$, to the distance traversed:

$$\dot{\rho}_{generation}^{(\alpha)} = \rho_{source}^{(\alpha)} \frac{v^{(\alpha)}}{y_{back}} \tag{2.18}$$

The dislocation density generation rate can be expressed in a new form using the Orowan equation for shear slip rate:

$$\dot{\gamma}^{(\alpha)} = \rho_m^{(\alpha)} b^{(\alpha)} v^{(\alpha)} \tag{2.19}$$

$$\dot{\rho}_{generation}^{(\alpha)} = \frac{\phi \sum_\beta \sqrt{\rho_{im}^{(\beta)}}}{b^{(\alpha)}} \left(\frac{\rho_{im}^{(\alpha)}}{\rho_m^{(\alpha)}} \right) \dot{\gamma}^{(\alpha)} \tag{2.20}$$

where ϕ is a geometric parameter and $b^{(\alpha)}$ is the magnitude of the Burgers vector on slip system α.

The dislocation density interaction rates represent the rate at which mobile dislocation become immobilized. The frequency of interaction between the mobile dislocation densities in slip system α and the mobile dislocation densities in slip system β is defined as $\rho_m^{(\alpha)} \rho_m^{(\beta)} v^{(\alpha\beta)}$. The same frequency of interaction with the immobile dislocation densities in slip system β is defined as $\rho_m^{(\alpha)} \rho_{im}^{(\beta)} v^{(\alpha)}$. The Orowan equation can then be used to define the relative velocity between slip systems:

$$v^{(\alpha\beta)} = \frac{\dot{\gamma}^{(\alpha)}}{\rho_m^{(\alpha)} b^{(\alpha)}} + \frac{\dot{\gamma}^{(\beta)}}{\rho_m^{(\beta)} b^{(\beta)}} \tag{2.21}$$

The interaction forms a junction, with a length defined by the spacing of immobile dislocations:

$$l_c = \frac{1}{\sum_\beta \sqrt{\rho_{im}^{(\beta)}}} \tag{2.22}$$

The proportion of these junctions that are stable is represented by the fraction f_0. This fraction is used to modify the frequency of interaction between slip systems, and substitution then provides the following relation for $\dot{\rho}^{(\alpha)}_{interaction-}$, the rate of mobile dislocation density immobilization through interactions:

$$\dot{\rho}^{(\alpha)}_{interaction-} = f_0 \sum\nolimits_{\beta} \sqrt{a_{\alpha\beta}} \left(\rho_m^{(\beta)} l_c \frac{\dot{\gamma}^{(\alpha)}}{b^{(\alpha)}} + \rho_m^{(\alpha)} l_c \frac{\dot{\gamma}^{(\beta)}}{b^{(\beta)}} \right) + f_0 \sum\nolimits_{\beta} \sqrt{a_{\alpha\beta}}\, \rho_{im}^{(\beta)} l_c \frac{\dot{\gamma}^{(\alpha)}}{b^{(\alpha)}} \qquad 2.23$$

Frank's rule is used to determine energetically favorable interactions for immobile junction formation, which can be described as the following interaction tensor for junction formation on slip system α due to the interactions of slip systems β and γ:

$$n_{\alpha}^{\beta\gamma} = \begin{cases} 1 \; if \; \mu\left(b^{(\alpha)}\right)^2 < \mu\left(b^{(\beta)}\right)^2 + \mu\left(b^{(\gamma)}\right)^2 \; and \; b^{(\alpha)} = b^{(\beta)} + b^{(\gamma)} \\ 0 \; otherwise \end{cases} \qquad 2.24$$

The total addition of dislocation densities due to interactions becomes:

$$\dot{\rho}^{(\alpha)}_{interaction+} = f_0 \sum\nolimits_{\beta,\gamma} \left(\rho_m^{(\beta)} l_c \frac{\dot{\gamma}^{(\gamma)}}{b^{(\gamma)}} + \rho_m^{(\gamma)} l_c \frac{\dot{\gamma}^{(\beta)}}{b^{(\beta)}} \right) + f_0 \sum\nolimits_{\beta,\gamma} \left(\rho_{im}^{(\beta)} l_c \frac{\dot{\gamma}^{(\gamma)}}{b^{(\gamma)}} + \rho_{im}^{(\gamma)} l_c \frac{\dot{\gamma}^{(\beta)}}{b^{(\beta)}} \right) \qquad 2.25$$

For the hcp materials examined in this study, the dislocation density rates were calculated in accordance with the work of Ziaei and Zikry [44].

An Arrhenius type relation is used to represent the dislocation-density annihilation rate $\dot{\rho}^{(\alpha)}_{annihilation}$ [45] resulting from the recovery process:

$$\dot{\rho}^{(\alpha)}_{annihilation} = v^{(\alpha)} e^{\left(-\frac{H}{kT}\right)} \qquad 2.26$$

where $v^{(\alpha)}$ represents the attempted frequency of immobile dislocation intersection by mobile dislocations on other slip systems:

$$v^{(\alpha)} = f_0 \sum\nolimits_{\beta} \rho_m^{(\alpha)} l_c \frac{\dot{\gamma}^{(\beta)}}{b^{(\beta)}} \tag{2.27}$$

and H represents the activation enthalpy, which is defined using the immobile dislocation density and saturation dislocation density ρ_s:

$$H = H_0 \left(1 - \sqrt{\frac{\rho_{im}^{(\alpha)}}{\rho_s}} \right) \tag{2.28}$$

These terms can then be combined to develop a revised relation for $\dot{\rho}_{annihilation}^{(\alpha)}$:

$$\dot{\rho}_{annihilation}^{(\alpha)} = \left(f_0 \sum\nolimits_{\beta} \rho_m^{(\alpha)} l_c \frac{\dot{\gamma}^{(\beta)}}{b^{(\beta)}} \right) e^{\frac{-H_0\left(1-\sqrt{\frac{\rho_{im}^{(\alpha)}}{\rho_s}}\right)}{kT}} \tag{2.29}$$

The generation, interaction, and recovery relations can then be used to obtain coupled equations for the evolution of mobile dislocation densities (ρ_{mo}) and immobile dislocation densities (ρ_{im}). These evolution equations can be expressed using nondimensional coefficients as:

$$\frac{d\rho_m^\alpha}{dt} = |\dot{\gamma}^\alpha| \left(\frac{g_{sour}^\alpha}{b^2} \left(\frac{\rho_{im}^\alpha}{\rho_m^\alpha} \right) - g_{mnter-}^\alpha - \rho_m^\alpha - \frac{g_{immob-}^\alpha}{b} \sqrt{\rho_{im}^\alpha} \right) \tag{2.30}$$

$$\frac{d\rho_{im}^\alpha}{dt} = |\dot{\gamma}^\alpha| \left(g_{mnter+}^\alpha \rho_m^\alpha + \frac{g_{immob+}^\alpha}{b} \sqrt{\rho_{im}^\alpha} - g_{recov} \rho_{im}^\alpha \right) \tag{2.31}$$

where g_{sour} is the coefficient pertaining to an increase in the mobile dislocation density due to dislocation sources, g_{mnter} is the coefficient related to the trapping of mobile dislocations due to forest intersections, cross slip around obstacles, or dislocation interactions, g_{recov} is related to the rearrangement and annihilation of immobile dislocations, and g_{immob} is related to the immobilization of mobile dislocations. These coefficients, which have been nondimensionalized, are updated as functions of the material deformation as described by Shanthraj and Zikry [41]. They are summarized in Table 2.1, where f_0, and φ are geometric parameters. H_0 is the reference activation enthalpy, l_c is the mean free path of a gliding dislocation, b is the magnitude of the Burgers vector, and ρ_s is the saturation density. It should be noted that these coefficients are functions of the immobile and mobile densities, and hence are updated as a function of the deformation mode.

There were 24 slip systems modeled for the hcp crystal structure representing the matrix zirconium alloy, spanning the basal, prismatic, pyramidal <c>, and pyramidal <c+a> classifications. They are shown in Table 2.2, along with the indices that will be used to refer to them in graphics throughout the text for brevity. 12 fcc slip systems were modeled to represent the crystal structure for the δ hydride, and these are shown in Table 2.3.

2.3 Orientation Relationship (OR) between Zr4 Matrix and Hydrides

An OR is described as:

$$n_{matrix}//n_{hydride}, r_{matrix}//r_{hydride} \tag{2.32}$$

in which the plane and directions of the respective unit cells for an interface between two disparate crystallographic systems are defined, so that their orientations with respect to each other and the global axis can be calculated. Ziaei and Zikry have calculated 36 ORs describing the parallel slip directions and planes in the multiphase hcp and fcc system [46]. Of these, Ude. Et al. has demonstrated experimentally that the $(0001)_{hcp}//\,(111)_{fcc}\ and\ [11\bar{2}1]_{hcp}//\,(\bar{1}10)_{fcc}$ OR between the hcp zirconium matrix and the fcc δ hydride is observed most often [47], and the hydrides modeled in this work are δ hydrides that follow this OR. The transformation between the local hydride orientation to the global orientation is given by the following relation:

$$[X]_{global} = [T]_2[T]_1[X]_{local} \tag{2.33}$$

where the new global orientation is given by $[X]_{global}$, the initial orientation of the hydride is given by $[X]_{local}$, the transformation from the hydride to the parent matrix is given by $[T]_1$, and the transformation from the parent matrix to the global coordinate system is provided by $[T]_2$.

2.4 Fracture Criterion and Overlapping Element Method

Fracture occurs on the {0 0 1} family of planes for fcc materials [48] and on the basal (0 0 0 1) planes for hcp materials [46]. The fracture method is implemented by monitoring the maximum normal component of traction across all the material cleavage planes. Fracture was initiated when the component of traction on the cleavage planes (n_{cleave}) exceeded a critical fracture stress threshold, σ_{FC}:

$$max_{cleavage\ planes}(n_{cleave}^{T}[\sigma]n_{cleave}) > \sigma_{FC} \qquad 2.34$$

The fracture method used here is based on crack nucleation within a finite element mesh by splitting the element into two halves along the crack plane. The method to nucleate and propagate cracks was refined by Wu and Zikry [49] for microstructurally based fracture and extended by Bond and Zikry [50] to accommodate branching cracks. To avoid numerical instability from the instantaneous release of elastic energy within the newly cracked element, a traction-free surface is generated by reducing the nodal forces over a set time step interval until they reach zero. The crack is then nucleated by adding phantom nodes to elements aligned to the crack plane. A more detailed approach is given in [33].

2.5 Thermo-Mechanical Coupling

Thermal evolution can be decomposed into adiabatic and heat conduction components. Adiabatic heat generation can be determined using plastic work and a χ parameter indicating the fraction of plastic work converted to heat energy:

$$q_{mechanical} = \chi \sigma'_{ij} D^{P}_{ij} \qquad 2.35$$

where plastic work is represented by D^{P}_{ij} and the deviatoric stress is represented by σ'_{ij}. Combining this term with a relationship for heat conduction gives:

$$\rho c_p \dot{T} = \lambda \nabla^2 T + q_{mechanical} \qquad 2.36$$

where ρ is the material density, c_p is the specific heat capacity, and λ is the thermal conduction coefficient. $\dot{T}$ represents the rate of change of temperature. The discretized finite element heat conduction equation can then be given as follows:

$$[C]\{\dot{T}\} + [K]\{T\} = \{R_T\} \qquad 2.37$$

where $[C]$ and $[K]$ represent the matrices of coefficients proportional to the temperature rate of change and the temperature, respectively. $\{R_T\}$ is the vector of nodal input heat sources.

2.6 Numerical Methods

The rate-dependent crystalline plasticity formulation developed by Zikry [51] was used to update the total deformation rate tensor (D_{ij}) and the plastic deformation rate tensor (D_{ij}^{P}), which in turn are used to update the material stress state. D_{ij} was obtained using an implicit finite-element method with a quasi-Newton BFGS scheme for quasi-static deformation. Q4 quadrilateral elements were used to obtain nodal displacements and the total velocity gradient. 1-point integration of the elements was used to ensure simulation efficiency. Stiffness-based hourglass control was used to avoid numerical issues associated with 1-point integration [52]. To avoid numerical instabilities and error propagation associated with stiffness, a hybrid explicit-implicit method was used to obtain D_{ij}^{P} and to update the dislocation density evolution equations, where the g coefficients were presumed to be unknowns and part of the solution.

Table 2.1: Nondimensional coefficients describing dislocation density evolution.

Coefficient	**Expression**
g^{α}_{sour}	$\phi \sum_{\beta} \sqrt{\rho^{(\beta)}_{im}}$
g^{α}_{mnter-}	$f_0 l_c \sum_{\beta} \sqrt{a_{\alpha\beta}} \left[\frac{\rho^{(\beta)}_{m}}{\rho^{(\alpha)}_{im} b^{(\alpha)}} + \frac{\dot{\gamma}^{(\beta)}}{\dot{\gamma}^{(\alpha)} b^{(\beta)}} \right]$
g^{α}_{immob-}	$\frac{f_0 l_c}{\sqrt{\rho^{(\alpha)}_{im}}} \sum_{\beta} \sqrt{a_{\alpha\beta}} \rho^{(\beta)}_{im}$
g^{α}_{mnter+}	$\frac{f_0 l_c}{\dot{\gamma}^{(\alpha)} \rho^{(\alpha)}_{m}} \sum_{\beta,\gamma} \sqrt{a_{\beta\gamma}} \left[\frac{\rho^{(\gamma)}_{m} \dot{\gamma}^{(\beta)}}{b^{(\beta)}} + \frac{\rho^{(\beta)}_{m} \dot{\gamma}^{(\gamma)}}{b^{(\gamma)}} \right]$
g^{α}_{immob+}	$\frac{f_0 l_c}{\dot{\gamma}^{(\alpha)} \sqrt{\rho^{(\alpha)}_{im}}} \sum_{\beta,\gamma} n^{\beta\gamma}_{\alpha} \sqrt{a_{\beta\gamma}} \rho^{(\gamma)}_{im} \dot{\gamma}^{(\beta)}$
g^{α}_{recov}	$\frac{f_0 l_c}{\dot{\gamma}^{(\alpha)}} \left(\sum_{\beta} \sqrt{a_{\alpha\beta}} \frac{\dot{\gamma}^{(\beta)}}{b^{(\beta)}} \right) e^{\frac{-H_0 \left(1 - \sqrt{\frac{\rho^{(\alpha)}_{im}}{\rho_s}} \right)}{kT}}$

Table 2.2: HCP Slip Systems

Basal	1	$(0\ 0\ 0\ 1)\ [2\ \bar{1}\ \bar{1}\ 0]$
	2	$(0\ 0\ 0\ 1)\ [\bar{1}\ 2\ \bar{1}\ 0]$
	3	$(0\ 0\ 0\ 1)\ [\bar{1}\ \bar{1}\ 2\ 0]$
Prismatic	4	$(1\ 0\ \bar{1}\ 0)\ [\bar{1}\ 2\ \bar{1}\ 0]$
	5	$(0\ \bar{1}\ 1\ 0)\ [2\ \bar{1}\ \bar{1}\ 0]$
	6	$(\bar{1}\ 1\ 0\ 0)\ [\bar{1}\ \bar{1}\ 2\ 0]$
Pyramidal <a>	7	$(1\ 0\ \bar{1}\ 1)\ [\bar{1}\ 2\ \bar{1}\ 0]$
	8	$(0\ \bar{1}\ 1\ 1)\ [2\ \bar{1}\ \bar{1}\ 0]$
	9	$(\bar{1}\ 1\ 0\ 1)\ [\bar{1}\ \bar{1}\ 2\ 0]$
	10	$(\bar{1}\ 0\ 1\ 1)\ [\bar{1}\ 2\ \bar{1}\ 0]$
	11	$(0\ 1\ \bar{1}\ 1)\ [2\ \bar{1}\ \bar{1}\ 0]$
	12	$(1\ \bar{1}\ 0\ 1)\ [1\ 1\ \bar{2}\ 0]$
Pyramidal <c+a>	13	$(1\ 0\ \bar{1}\ 1)\ [\bar{1}\ \bar{1}\ 2\ 3]$
	14	$(1\ 0\ \bar{1}\ 1)\ [\bar{2}\ 1\ 1\ 3]$
	15	$(0\ \bar{1}\ 1\ 1)\ [1\ 1\ \bar{2}\ 3]$
	16	$(0\ \bar{1}\ 1\ 1)\ [\bar{1}\ 2\ \bar{1}\ 3]$
	17	$(\bar{1}\ 1\ 0\ 1)\ [2\ \bar{1}\ \bar{1}\ 3]$
	18	$(\bar{1}\ 1\ 0\ 1)\ [1\ \bar{2}\ 1\ 3]$
	19	$(\bar{1}\ 0\ 1\ 1)\ [2\ \bar{1}\ \bar{1}\ 3]$
	20	$(\bar{1}\ 0\ 1\ 1)\ [1\ 1\ \bar{2}\ 3]$
	21	$(0\ 1\ \bar{1}\ 1)\ [\bar{1}\ \bar{1}\ 2\ 3]$
	22	$(0\ 1\ \bar{1}\ 1)\ [1\ \bar{2}\ 1\ 3]$
	23	$(1\ \bar{1}\ 0\ 1)\ [\bar{2}\ 1\ 1\ 3]$
	24	$(1\ \bar{1}\ 0\ 1)\ [\bar{1}\ 2\ \bar{1}\ 3]$

Table 2.3: FCC Slip Systems

1	$(1\ 1\ 1)\ [\bar{1}\ 0\ 1]$
2	$(1\ 1\ 1)\ [\bar{1}\ 1\ 0]$
3	$(1\ 1\ 1)\ [0\ \bar{1}\ 1]$
4	$(\bar{1}\ \bar{1}\ 1)\ [0\ 1\ 1]$
5	$(\bar{1}\ \bar{1}\ 1)\ [\bar{1}\ 1\ 0]$
6	$(\bar{1}\ \bar{1}\ 1)\ [1\ 0\ 1]$
7	$(\bar{1}\ 1\ 1)\ [1\ 0\ 1]$
8	$(\bar{1}\ 1\ 1)\ [1\ 1\ 0]$
9	$(\bar{1}\ 1\ 1)\ [0\ \bar{1}\ 1]$
10	$(1\ \bar{1}\ 1)\ [0\ 1\ 1]$
11	$(1\ \bar{1}\ 1)\ [1\ 1\ 0]$
12	$(1\ \bar{1}\ 1)\ [\bar{1}\ 0\ 1]$

CHAPTER 3: Predictions of Crack Nucleation and Failure Using a Bayesian Microstructurally Predictive Framework

3.1 Introduction

To provide a direct and measurable link from microstructural mechanisms and characteristics to failure probability, we will introduce a ROM that is obtained by mining a database of crack responses of representative hydrided Zicaloy-4 structures. Specifically, the database is constructed using FEM simulations based on our previously detailed and validated microstructural deterministic fracture approaches that couple crystalline plasticity and a microstructurally based fracture nucleation framework. We will use a multiparametric ROM approach to generalize the results and determine the probability of material failure. Figure 3.1 shows the proposed approach to develop the fracture probability models. The starting points are the deterministic outputs from the dislocation-density based crystalline plasticity simulations, which are defined using material fingerprints drawn from a preconceived solution space of interest. The exploration and understanding of many dimensions of the parametric space, such as dislocation density accumulation, texture, shear-slip strains, and hydride distributions, structure, and orientation, which are difficult, if not impossible, to obtain experimentally, will provide the data necessary for this approach. Table 3.2 shows the parameters modified in these simulations and their range of values.

The method then consists of expressing the results in a compact form of a Gumbel distribution using Extreme Value Theory (EVT), a Bayesian approach for developing the fracture criteria for probability, and a modeling scheme based on Gaussian Process Regression (GPR) to obtain failure probabilities and the uncertainty associated with the predictions. The models were verified on data that was not used to train them using a test-train split method. The overall objective of this study is to provide a database of deterministic FE fracture approaches that explore a wide parameter space representing variations within hydrided zirconium alloy systems, and then to develop Bayesian models, based on these physically based datasets, to identify the dominant microstructural characteristics and mechanisms that result in the failure at different physical scales.

3.2 Approach

3.2.1 Fracture Stress Characterization

The univariate branch of Extreme Value Theory is a type of statistics that is focused specifically on large deviations of a parameter from the mean. Its practical form, the generalized extreme value (GEV) distribution, is a set of distributions that are designed to capture the distribution of these large deviations. The Gumbel formulation was chosen for this study because it has neither a finite upper bound nor a heavy tail, which is well-suited for fracture nucleation because elemental fracture stresses are neither expected to accumulate at the extremes without unloading (cracking) nor are large sections of material expected to uniformly aggregate at a particular limit. The Gumbel law is also known as the Type 1 GEV, and the associated probability density function (PDF) is described as follows:

$$P = \frac{1}{\beta} e^{-(z+e^{-z})}, \qquad where\ z = \frac{x-\mu}{\beta}. \tag{3.1}$$

To characterize element-wise stress in the form of a Gumbel distribution, individual element stress responses were recorded at incremental strain levels. The number of values at each stress level were then normalized by element size. The gumbel_r statistical function within the SciPy Python library was then used to fit a Gumbel distribution to the 95th percentile of stress results. [53]. This effectively reduced the most important data at the right tail extreme into the μ and β parameters.

To test the adequacy of the fit for the use of Gumbel distributions, the Pearson Coefficients for the individual Gumbel distribution fits were calculated. To do this, the probplot function from SciPy was used to generate both an estimate of the quantiles of the sample data and associated quantile predictions of the fitted Gumbel distribution. Filliben’s estimate was used to calculate the quantiles of the observed data. These data were compared and a “goodness of fit" was calculated using the coefficient of determination. A value of 1.0 indicates that the quantiles of both the fitted Gumbel distribution and the observed data match perfectly. 4943 total Gumbel fits were performed; one for every output print interval for each simulation. Figure 3.2 shows these coefficient of determination values together in histogram format. 90.4% of the values are between 0.75 and 1.0, which indicates that the Gumbel distribution is an accurate method to approximate the stress response of the system.

The μ parameters of the Gumbel distributions were individually calculated and used to represent the extrema within the hydride materials being modeled. The shape parameter also provides valuable information about fat-tailed characteristics, and this information may be used in future studies.

3.2.2 Bayesian Framework

Bayes' rule was used to generate a framework for linking stress levels with the associated probabilities of failure. Bayes' Rule is given by Equation 3.2:

$$P(A|B) = \frac{P(B|A) \cdot P(A)}{P(B)}. \tag{3.2}$$

For this study, $P(A)$ and $P(B)$ were the probabilities of a crack forming and of the existence of a stress state at a particular nominal strain level. $P(A)$ was generated by examining the percentage of the database population at a given strain level that had cracked and represents the prior assumptions about a group of simulations at a particular strain level. The probabilities of cracking at various stress states and strain levels were calculated and stored. To generate the crack probability at a particular level of strain ϵ and stress σ, the simulations are sorted based on whether a crack has nucleated and whether $\mu > \sigma$ or $\mu < \sigma$. These probabilities were calculated explicitly. The ratios between these values provided P(A), P(B), and P(B|A), which were then used to calculate the probability of crack formation given a fracture critical stress state.

3.2.3 Gaussian Process Regression

Gaussian Process Regression (GPR) was used to represent the Bayesian framework probabilities in a continuous manner. Different GPRs were trained for each strain level to reduce the resulting complexity of the models. The GaussianProcessRegressor function within the SciKit-Learn package was used to train the models. [54] The data were split into training and testing segments that comprised 80% and 20%, respectively, of the total data set size. The included scoring function was used to verify the accuracy of the resulting GPRs. An additive combination of the absolute exponential kernel and the radial basis function kernel were used to capture effects at high length scales and low length scales, respectively. High length scale effects include the steady rise of the cumulative density function as the value of μ increases. Length scales for each function were chosen using hyperparameter tuning.

3.3 Results and Discussion

3.3.1 Model and Database

A database of 210 crystal plasticity simulations was generated for this study to identify the variation of stress and fracture characteristics in hydrided zirconium alloys. Each simulation was performed both with and without crack nucleation, so that the localized material unloading associated with crack formation would not interfere with the bulk stress measurements performed for this study. The database was populated by randomly modifying five parameters of interest using 4 predefined levels between a minimum value and a maximum value. (Table 3.2) These parameters were chosen because they belong to two general categories of interest: 1) material orientation, 2) hydride population geometry and distributions. These categories influence both dislocation-density activity and material fracture [6], [8], [21], [32]. Together, they comprise the material *fingerprint* of individual simulations and are the only differentiating factor between them. The trajectory scheme from the Elementary Effects method implemented using the SAlib library and was also used to select random trajectories throughout the solution space made of all possible material fingerprints [55], [56].

These models were designed to emulate the material response of a cladding tube undergoing a uniform internal pressurization. Two roller boundary conditions were modeled along with one uniform displacement loading condition oriented tangentially to the circumferential direction of the tube. The loading diagram is shown in Figure 3.3. A new multigrain representation of a specific material fingerprint was developed for each simulation, with an average mesh size of approximately 60,000 elements and with 49 parent zirconium alloy grains modeled. A randomized grain-to-grain maximum misorientation of 10° was applied to the zirconium alloy hcp grains. The material properties were validated using the work of Mohamed and Zikry [32] and are presented in Table 3.1.

After 5 initial trajectories were developed for the database (a total of 30 completed simulations) the SAlib implementation of the Elementary Effects Method was used to perform a global sensitivity analysis of the sparse dataset that had been collected to determine the impact of each of the chosen parameters [55], [56]. The elementary effects were quantified for both the hydrides and parent material. All parameters were found to be significant, with the hydride spacing parameter showing the lowest effect value of 396 MPa. Given that the lowest elementary effect was approximately 40% of the material fracture stress, all material parameters were deemed significant.

3.3.2 Impact of Hydride Orientation on Crack Probability

Crack probabilities at 0.75% and 3.25% nominal strains were obtained to examine fracture characteristics at relatively low and relatively high strain levels. It should be underscored that these are the global nominal strains, and that the local shear slip associated with different slip systems are significantly higher. Three categories were used to define hydride orientations: circumferential, radial, and mixed. Circumferential hydrides are parallel to the loading direction, radial hydrides are perpendicular to the loading direction, and mixed hydrides occur in all other orientations (30° and 60°).

The outputs are shown in Figure 3.4. At 0.75% strain, the circumferentially hydrided zirconium alloy has reduced fracture probability when compared to mixed hydrided materials at the elevated stress levels. The probability of radial cracks nucleating at lower strains than circumferential hydrides is consistent with experimental observations (cf. [11], [17]). At 3.25% nominal strain, the difference between the fracture probabilities is lower because the impact of aggregate nominal strain on the material as a factor influencing fracture outweighs the impact of hydride orientation. The values of μ necessary for high crack probabilities increase with strain, indicating that the likelihood of fracture depends on the nominal strain level. This may be a result of wider distributions of fracture critical stress at lower strain levels, and a greater coalescence around critical values as the material reaches high nominal strains. This may also describe the tendency of different hydride orientations to make the most impact on fracture probability at low strain levels. Figure 3.9 additionally shows the number of cracks that can be expected in the 0.2 mm x 0.2 mm simulation area as a function of nominal strain and hydride orientation. Circumferentially hydrided material nucleates fewer cracks on average compared with radially hydrided material at similar nominal strain levels.

3.3.3 Models Describing Crack Probability as a Function of Strain and Fracture Stress

Gaussian Process Regressors (GPRs) were used to generate a uniform function approximation of the relationship between the probability of failure and the fracture stress at various strain levels. The regressor predictions, as a function of the training data, are shown in Figure 3.5. The output of a GPR returns a predictive distribution, so GPRs have the natural advantage of quantifying the uncertainty associated with their predictions. Two standard deviations of these predictive distributions are shown between the bottom and top edges of the shaded regions in Figure 3.5. At lower strain levels, such as 0.75%, fracture probability is low until large fracture stress levels develop in the material at approximately 600 MPa. This is compared with the 3.25% strain level, where any fracture stress level above approximately 800 MPa is predicted to result in failure. This suggests that fracture stress and nominal strain both play a significant role in material failure. The lower fracture stress for nucleation at lower nominal strains is due to the increased ductility associated with increased immobile dislocation density activity.

3.3.4 Statistically predicting the spatial distribution of fracture

To test the effectiveness of these statistical models, the test-set data were analyzed using the previously trained GPRs shown in Figure 3.5, such that the models were tested against data that had not been used to train them. The models were used to develop estimates for the probability of failure at actual failure sites to gauge their predictability. Ideally, the models would predict a 100% likelihood of failure at the strain levels that the individual test simulations indicated a failure. The individual probability outputs are shown as a histogram in Figure 3.6 to demonstrate the effectiveness of the modeling system on a population of input data. 13 out of 16 predictions demonstrated an acceptable level of accuracy. Significant material fingerprint variation within the test and training sets, such as the known distinction between the response of radial and circumferential hydrides, may account for this variation.

3.3.5 Models Describing Crack Probability as a Function of Strain and Shear Slip

Dislocation-densities play a dominant role in crack nucleation, particularly at the interfaces within multiphase materials, such as the hydrided zirconium alloys being examined. Dislocation densities can blunt crack growth directions and nucleation sites [57]. Hence, shear slip, which is the total accumulated plastic strain on all slip systems, was used to determine failure probability in the same manner as fracture critical stress. Figure 3.7 shows the predictions of failure probability given by the interrogated data. Even at high levels of strain, the levels of shear slip must reach a critical level before fracture probability begins to rise abruptly. This is consistent with hydrides, particularly with the fcc crystal structure, being dislocation sources within a material and allowing limited amounts of ductility and crack-blunting until the interface-induced effects become dominant at higher strain and shear slip levels [32], [58], [59]. The change in cracking characteristics at different strain levels can also be observed in Figure 3.8, where the average total crack length is calculated with respect to strain level by averaging the summed length of the cracks in each simulation and at each increment of nominal strain. A similar sharp inflection point is indicated at high strain levels.

All shear slip models predicted a 100% probability of failure when provided with the test-set data. This corroborates that a link exists between dislocation-density activity and fracture probability. This is likely because dislocation-density activity that occurs during material strain can is a driving factor in controlling failure through crack blunting effects but can also be an indicator of the excessive plastic work that leads to fracture, as indicated by Elkhodary and Zikry [60].

3.3.6 Heatmaps Predicting Probability of Failure

These GPRs can be used to generate cracking probability predictions on a spatial element within a mesh where fracture critical stress is known. The knowledge of where cracking is likely to occur is helpful for examining the impact of hydrides in a zirconium matrix and for adding additional functionality to simulations where crack nucleation is not modeled. In Figure 3.10, the process is visually demonstrated. The normal stress results from the simulation at the strain of interest and is used as element-wise input data to the GPRs. The resulting predictions are then plotted to the same elements, providing a spatial method for interpreting the results. In this case, hydrided regions of the mesh are most likely to crack due to factors such as hydride orientation and spacing. This is consistent with experimental observations and measurements and fracture predictions [6], [8], [21].

3.3.7 Slip System Response and Dislocation Density Evolution

The accumulation of dislocation-densities is an important microstructural characteristic that dictates material performance at high strain levels [32]. The level of immobilization generated in individual slip systems is indicative of the material's ability to deform on certain slip planes and directions. Therefore, this would be essential for understanding one of the root causes of crack nucleation. The dislocation-density data from all simulations in the database were segmented by orientation, and then further by material type (hydrided and non-hydrided). The maximum values of dislocation density from each simulation were developed into separate bar charts for mobile slip system activation and immobile slip system activation. (Figure 3.11a, b) Further, the dislocation density of regions where failure was predicted to be above 85% were compared to the maximums from all regions to determine how dislocation activity at crack initiation regions compared with dislocation activity elsewhere. (Figure 3.11c, d) Table 3 and Table 4 show which slip systems correspond to each slip system index referenced in the figures.

Figure 3.11 shows that the maximum values of ρ_{mo}, an indicator of dislocation movement and ductility within the material, do not occur at the locations with the greatest crack probability within the h.c.p. matrix. ρ_{mo} is shown to decrease by approximately an order of magnitude between the absolute maximum values of ρ_{mo} and the areas of high fracture likelihood. This contrasts with the f.c.c. hydride material, where the highest values of ρ_{mo} are directly observed at the defined high probability crack initiation regions; and little difference is observed between the two charts. While the h.c.p. matrix has higher maximum ρ_{mo} compared with f.c.c. hydride material in absolute terms, the reduction at likely crack initiation sites reduces ρ_{mo} such that it is approximately equal to that in the f.c.c. hydride. Furthermore, while both crystal structures exhibit preferred slip systems, the h.c.p. matrix exhibits a stronger orientation dependence, with the 0° case associated with comparatively lower ρ_{mo}. While the hcp system can evolve different configurations of ρ_{mo} owing to the greater number of slip systems, leading to increased ductility, hydrides can also serve as sources of dislocation activity and ductility within the material, and exhibit less orientation dependence in the areas of the material volume that are critically loaded. This improved mobile slip system response contributes to the hydrides role in crack blunting. The hcp parent material had concentrated dislocation activity across a relatively small number of slip systems. This indicates that the hcp parent material's ability to blunt cracks is limited to a small number of slip systems and directions that heavily depend on material orientation, whereas the fcc hydrides are more capable of serving as a dislocation source regardless of their orientation.

Mobile dislocation density activity is also a significant indicator of the ductility within a material. For the parent zirconium alloy material, the prismatic ($\bar{1}$ 1 0 0) [$\bar{1}$ $\bar{1}$ 2 0] and pyramidal <a> (1 $\bar{1}$ 0 1) [1 1 $\bar{2}$ 0] slip systems exhibited the highest ρ_{mo} values. The majority of hydride slip activity occurs on the ($\bar{1}$ $\bar{1}$ 1) [$\bar{1}$ 1 0] and ($\bar{1}$ 1 1) [0 $\bar{1}$ 1] slip systems.

Immobilized dislocation-densities can be representative of dislocation pileups within a material that reduce ductility and eventually lead to crack nucleation. For the matrix material, most active immobile slip systems correspond to the most active mobile slip systems and are a combination of prismatic and pyramidal <a> systems. The immobile dislocation densities at locations specific to fracture are shown in Figure 3.12. The highest activations in the matrix are ($\bar{1}$ 1 0 0) [$\bar{1}$ $\bar{1}$ 2 0] and (1 0 $\bar{1}$ 1) [$\bar{1}$ 2 $\bar{1}$ 0], a combination of prismatic and pyramidal <a> systems.

3.4 Summary

Crack nucleation predictions were obtained using a database of 210 deterministic hydrided zirconium fracture models and a Bayesian framework. The predictions were obtained using a dislocation-density based crystalline plasticity approach and a nonlinear microstructurally based fracture model. Extreme Value Theory was used to characterize the fracture nucleation critical stress and shear slip levels within the simulations, and a series of GPRs provided probabilities of fracture nucleation with uncertainty bounds for a myriad of microstructural characteristics, such as hydride orientations and distributions, texture, and crystalline structures, such that dominant mechanisms could be identified. Orientation relations between the material phases provided an accurate representation of the complex interaction between the fcc and hcp materials for these multi-crystalline and phase systems. The effects of fracture critical stress and shear slip on crack nucleation were investigated, and these were dominant characteristics related to fracture nucleation. These predictions can provide new approaches for determining new fracture nucleation criteria in multiphase materials. To summarize, we were able to determine that

- The coupling between deterministic modeling and the statistically based probability predictions was established using a Bayesian approach. The GPR machine learning method was used to quantify uncertainties in the resulting ROMs. Crack nucleation was accurately predicted using both shear slip and fracture critical stress as dominant output categories.
- Hydride orientation is a significant factor in the likelihood of failure at lower strain levels. At specified failure strains, radial hydrides have a higher probability of failure at similar stress levels than do circumferential hydrides.

- Models of failure probability were used to create heatmaps showing cracking likelihood in a visual manner.
- Gumbel distributions were demonstrated to be an appropriate form for describing the extrema of the stress response of a material.

These proposed predictions provide a needed link and coupling between validated deterministic and statistical based machine learning approaches for a comprehensive understanding of the crack nucleation and propagation of hydrided zirconium alloys. This approach can be used to predict failure in other multiphase materials, such as alloys with inclusions or precipitates and coated material systems, at different physical scales ranging from the nano to the micro, such that validated deterministic models can be used to generate physically accurate datasets for statistically based machine learning approaches.

Table 3.1: Material Properties

Property	Zircaloy-4	δ-hydrides
Young's modulus (GPa)	90	132
Static yield stress (MPa)	220	220
Poisson's ratio	0.349	
Rate sensitivity coefficient	45	
Initial immobile dislocation density (m^{-2})	1×10^{10}	
Initial mobile dislocation density (m^{-2})	1×10^{7}	
Burger's vector	1×10^{-10}	
Fracture stress (MPa) (N/mm^2)	700	1000
Applied tensile nominal strain (%)	12	800

Table 3.2: Hydride microstructural distributions

Parameter Name	Minimum Value	Maximum Value
Hydride Length	$0.5 \times 10^{-5}\ m$	$3.0 \times 10^{-5}\ m$
Parent Material Orientation	0°	90°
Hydride Volume Fraction	5%	20%
Hydride Orientation	0°	90°
Hydride Spacing	2.5E-6 m	1.0E-5 m

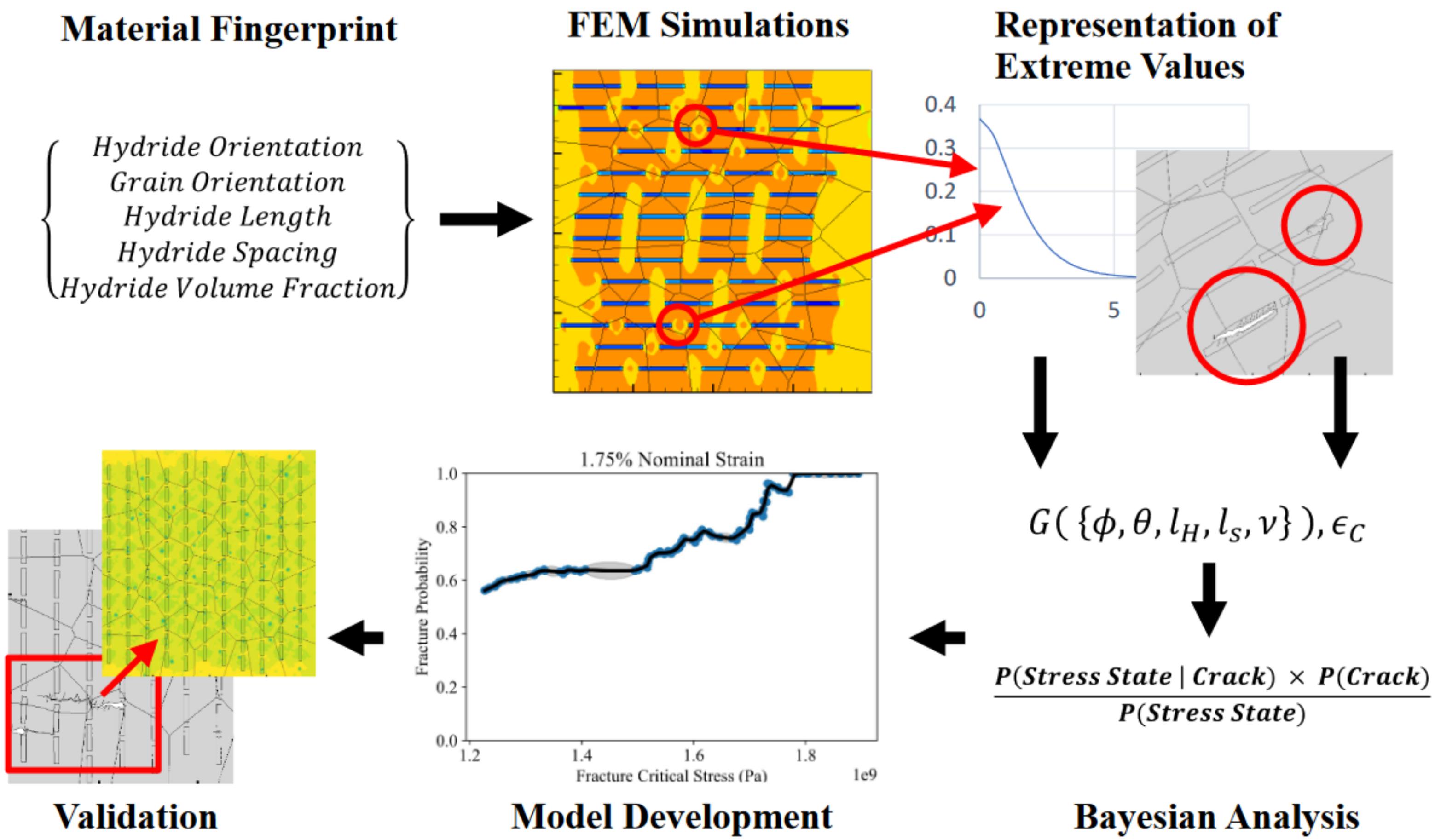

Figure 3.1. **Development of ROM describing failure probability.** An outline of the process starting at the database of simulations and ending with the verification of the final models.

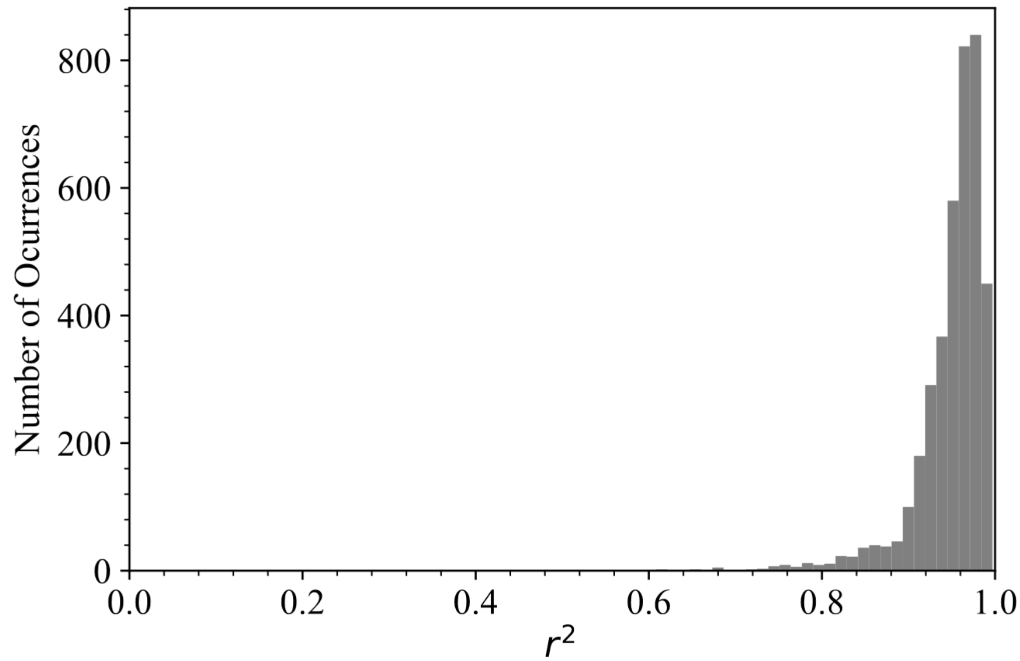

Figure 3.2. **Histogram of Gumbel Coefficients of Determination.** Pearson Coefficients for the trained Gumbel distributions, n = 3908.

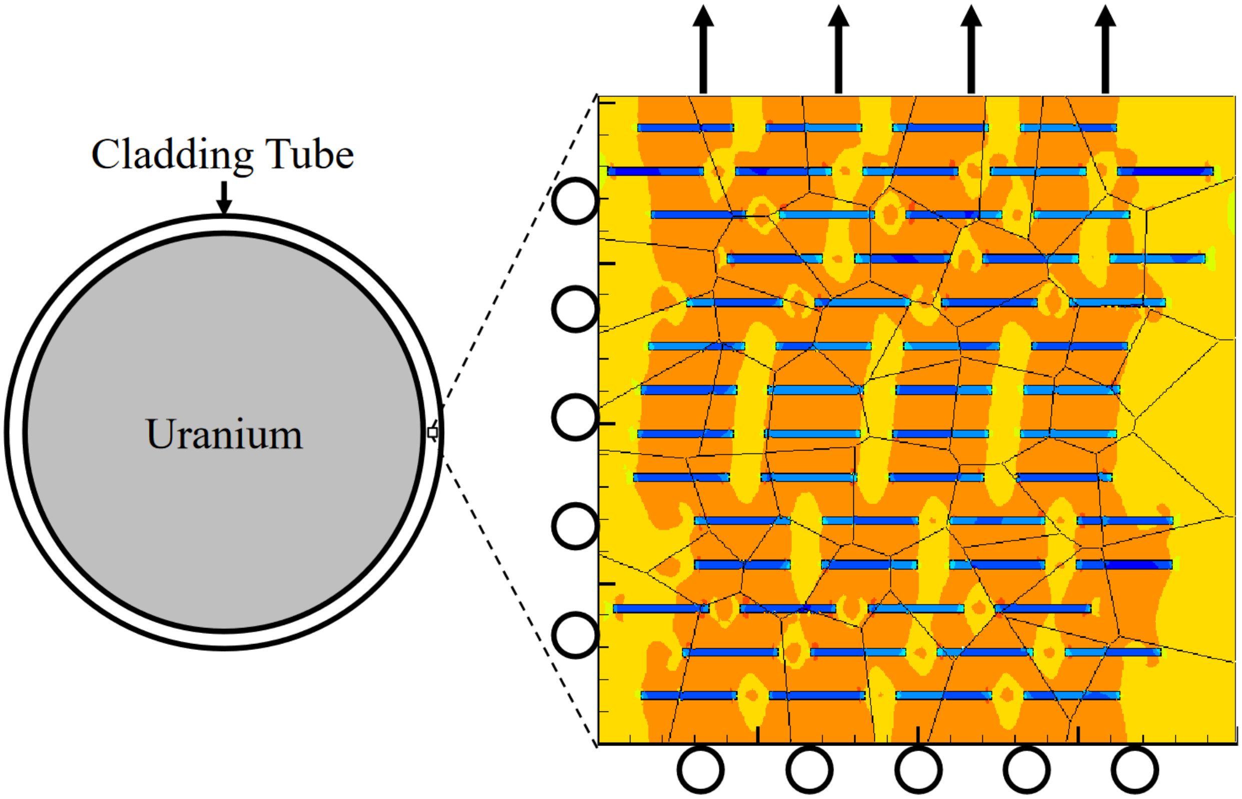

Figure 3.3. **A hydrided zirconium alloy volume.** A cladding tube and loading diagram of a typical multiphase hydrided zirconium alloy simulation used in this study.

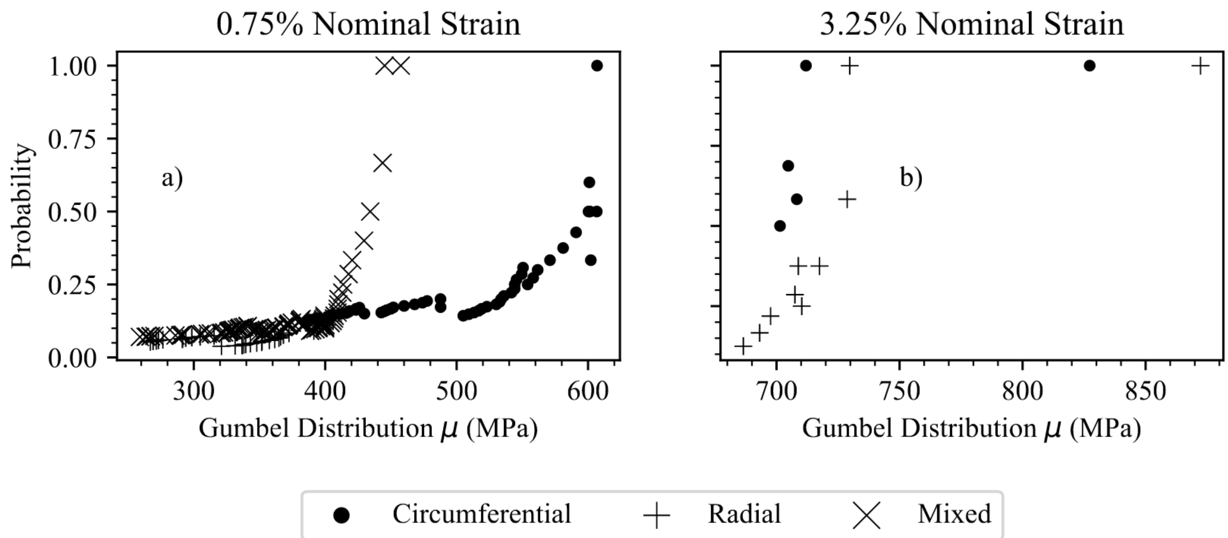

Figure 3.4. **Failure probability at 0.75% and 3.25% nominal strain.** Bayesian crack probability analysis differentiated by circumferential, radial, and mixed hydride orientation.

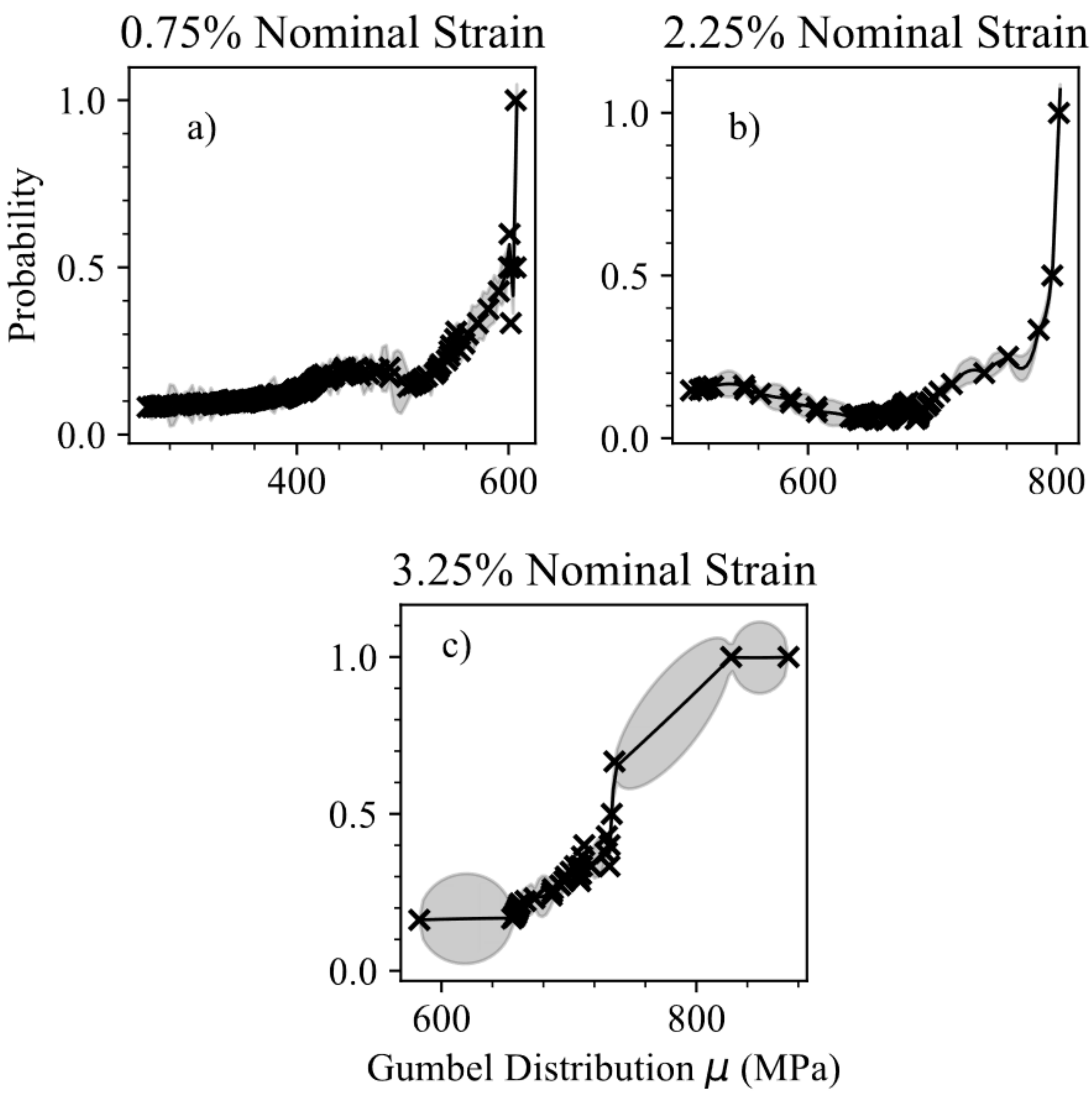

Figure 3.5. **Fracture probability model with fitted GPR.** Fitted GPR representing the failure probability for fracture critical stress levels at 0.75%, 2.25% and 3.25% nominal strains. Gray areas correspond to a single standard deviation of the predictive distribution in the GPR.

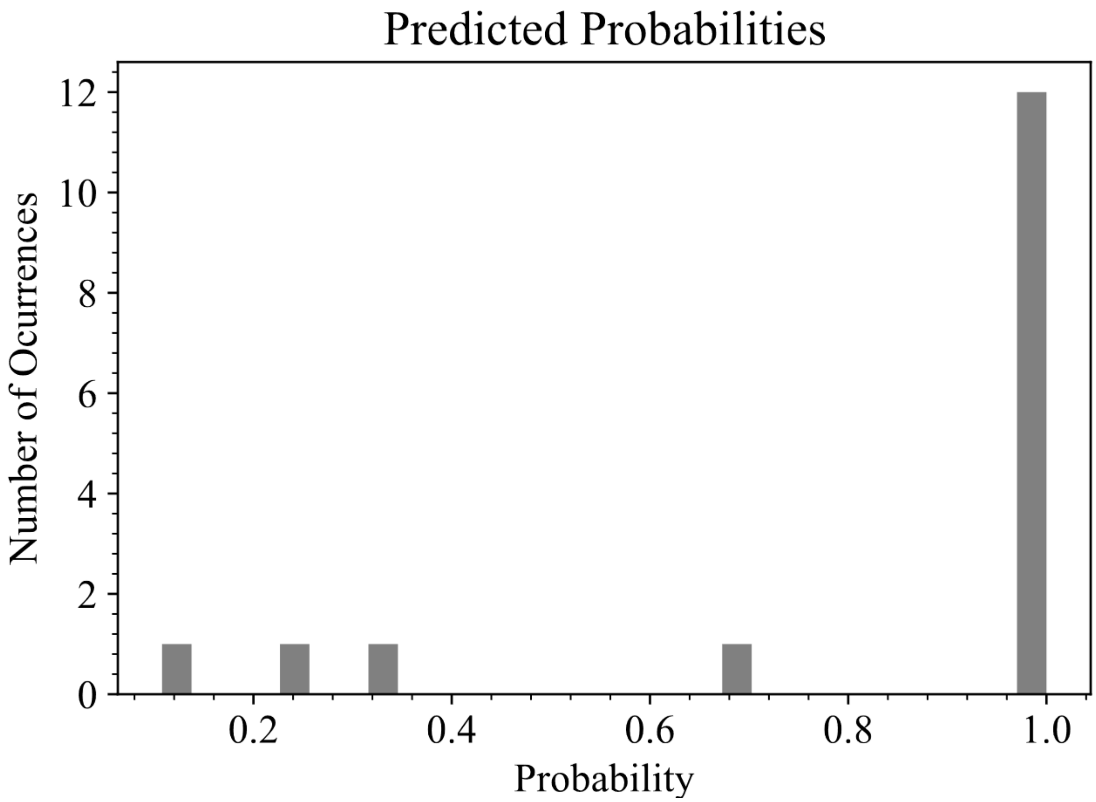

Figure 3.6. **Fracture critical stress model verification.** Predicted probability of failure on test-set data at 0.75%, 2.25% and 3.25% strains. The ideal value is 1.0, or 100% probability.

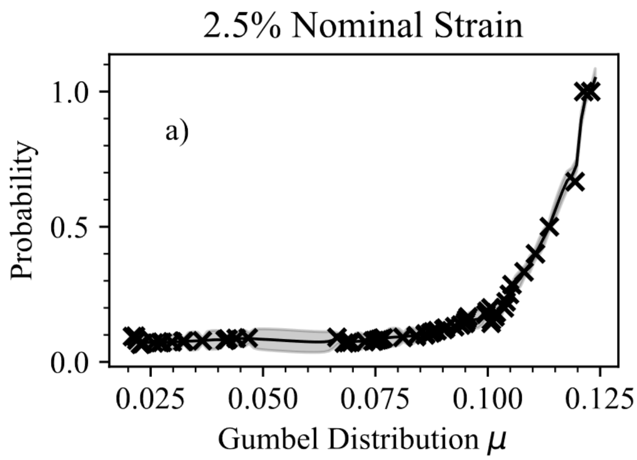

Figure 3.7. **Fracture probability model with fitted GPR.** Fitted GPR representing the failure probability for shear slip levels at 2.50% and 4.0% nominal strains. Gray areas correspond to a single standard deviation of the predictive distribution in the GPR.

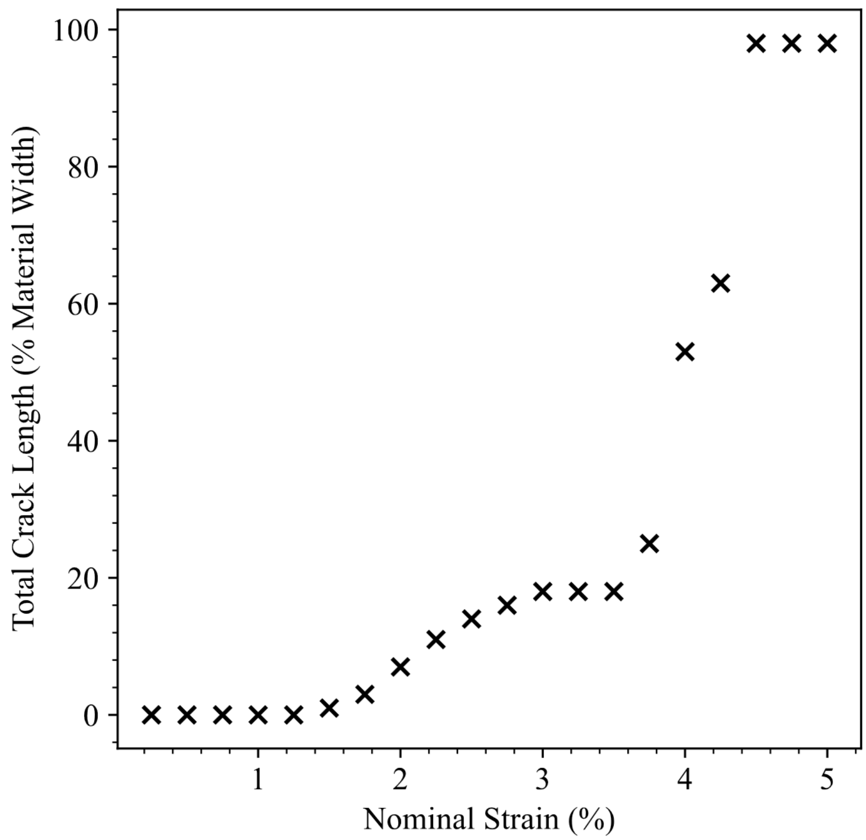

Figure 3.8: **Average of total crack length as a function of nominal strain.**

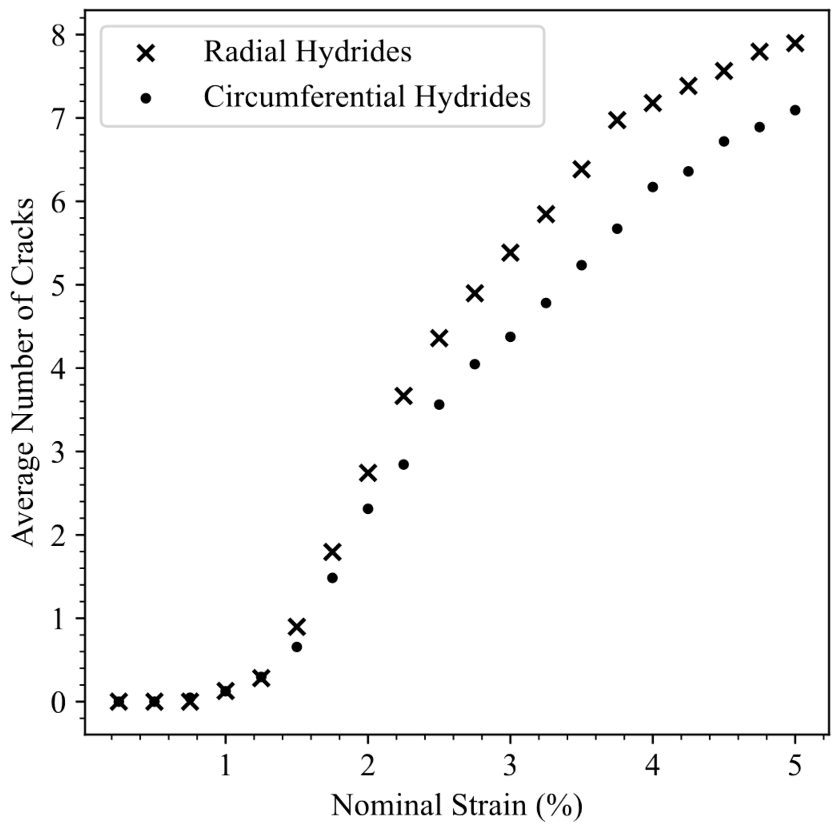

Figure 3.9: **Average number of cracks as a function of nominal strain.**

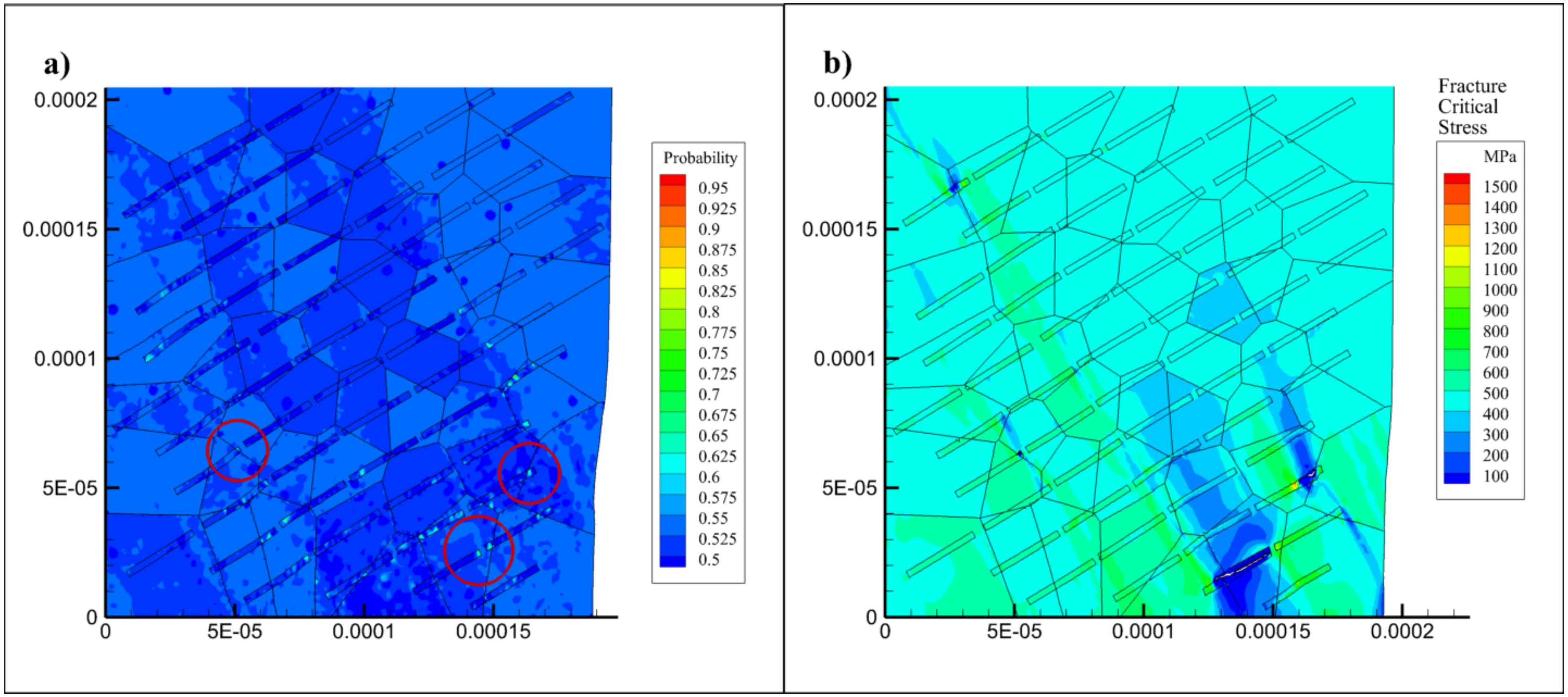

Figure 3.10. **Heatmap-based predictions of fracture locations.** a) A sample microstructure showing visual cracking probabilities as a heat map generated by the trained models, showing how cracks are most likely to initiate near hydride tips. Red circles indicate locations where crack development occurred. b) Crack development in areas with high probability of failure.

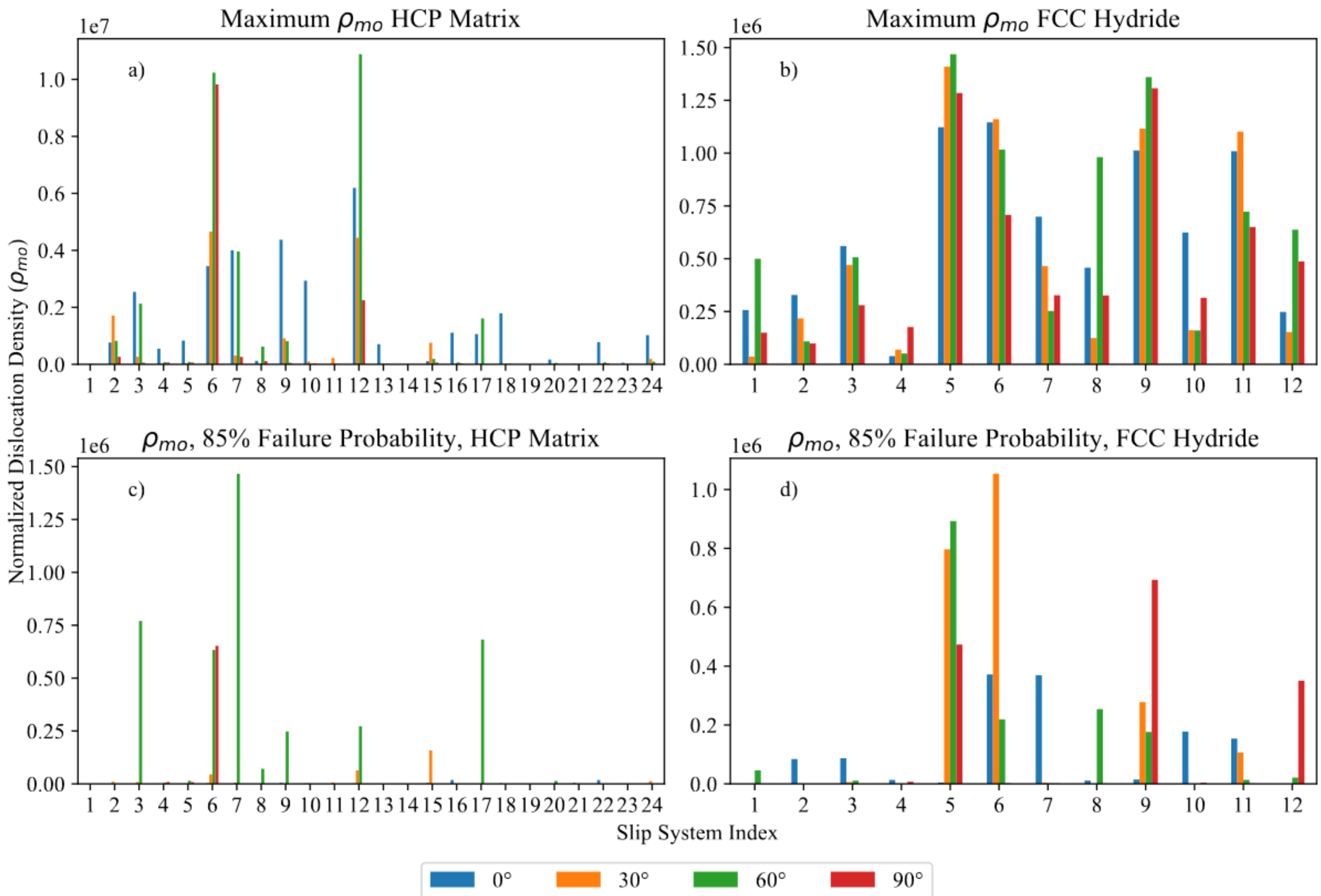

Figure 3.11. **Comparison of normalized ρ_{mo} between all areas (a, b) and locations with elevated failure probability (c, d) at 3.25% nominal strain.** a) Maximum ρ_{mo} in hcp matrix. b) maximum ρ_{mo} in fcc hydride. c) Average ρ_{mo} in hcp matrix at 85% failure probability. d) Average ρ_{mo} in fcc hydride at 85% failure probability.

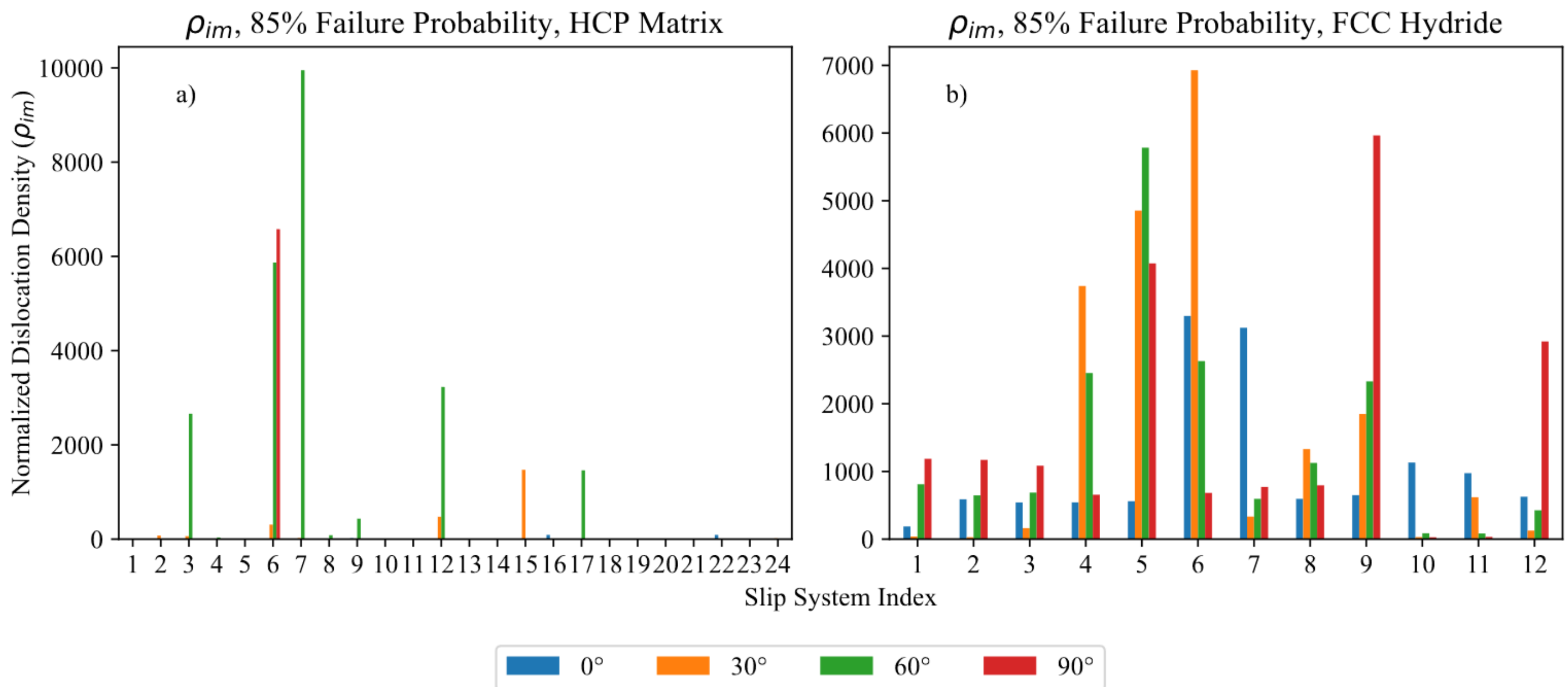

Figure 3.12. **Comparison of normalized ρ_{im} between h.c.p matrix (a) and f.c.c hydride (b) in locations with elevated failure probability.** a) Average ρ_{im} in hcp matrix at 85% failure probability. b) Average ρ_{im} in fcc hydride at 85% failure probability.

CHAPTER 4: Predictions of Material Response in Hydrided Zirconium Alloys

4.1 Introduction

A unified model describing the stress response across a set of parameters that describe the material fully is proposed, along with a statistically based ranking of the relative importance of material parameters. A major drawback to both experimental studies and simulations of hydrided zirconium alloys is the time and/or computational cost necessary to perform them. In response, various studies have proposed the use of reduced order models (ROMs) to characterize materials based on previously gathered data. These ROMs are not computationally expensive to query and provide a result that is a statistically significant representation of the data they were trained on. These approaches lack a sufficient reduced order expression for the spatial extreme phenomena that lead to material failure and crack propagation, and there are no such models that directly address the question of hydrided Zircaloy-4. Hence, a ROM that captures the tendency to fracture given a highly dimensional representation of the hydrided zirconium matrix is critical for understanding the characteristics of fracture in these materials and is also a necessary step to allowing the large-scale simulation of these materials by reducing the computational burden of modeling high fidelity materials at a macro scale.

In the present work, a dislocation density-based crystalline plasticity approach is used to model a representative solution space of the hydrided zirconium alloy problem. Various material properties were studied, comprising the material “fingerprint”: hydride orientation, material orientation, hydride volume fraction, hydride length, and hydride spacing. The resulting database was used to generate statistically significant models of fracture critical stress in the five-dimensional space that describes the material fingerprint. An extreme value theory (EVT) framework for reducing the dimensionality of a meshed model’s output was used to create a heavy-tailed representation of the material dynamics such that the resulting models best describe extreme failure events. Furthermore, these models were interrogated to determine the relative importance of each parameter comprising the material fingerprint. The process by which the raw data is processed via EVT, fit using various model types, and finally used to generate a probability of failure given a material fingerprint and strain level, is shown in Figure 4.1.

4.2 Approach

4.2.1 Model Setup

Each simulation was developed according to its own material "fingerprint" and consisted of a plane strain mesh with roller boundaries on two perpendicular sides and a uniform displacement boundary condition that displaced the material up to 5% nominal strain. The average mesh sizes were 60,000 elements and consisted of 49 zirconium alloy grains and approximately 50 hydrides, depending on the conditions such as hydride spacing and hydride length dictated by the fingerprint used to develop the model. A randomized maximum of 10° misorientation was incorporated from grain to grain. Mohamed and Zikry [32] validated the material properties used in the simulations, which are presented in Table 3.1.

4.2.2 Database Generation

To characterize the solution space of all possible fingerprints, a total of 210 simulations were simulated using FEM. The material fingerprints for each simulation consisted of 5 material parameters and were chosen according to uniform distributions bounded by the values in Table 3.2. The parameter values were chosen from a grid of 4 equally spaced values from within these bounds. These parameters have been found to influence dislocation activity and fracture, and the specific values used correspond to typical values found experimentally [6], [8], [21], [32]. To sample from the solution space, the trajectory method used in the Elementary Effects method (implemented in SAlib) was used [55], [56].

4.2.3 Model Development

To avoid numerical issues with the model input parameters being different length scales, the parameters were all processed by centering the mean of each feature around zero and scaling to unit variance using the StandardScaler function in Scikit-Learn [54]. The fracture critical stress values were also scaled by 100 MPa to avoid numerical issues with large numbers.

When training the models described in this work, the data was randomly split into an 85% training set and a 15% validation set. The training set was used to train model hyperparameters. The hyperparameters were randomly chosen for training within predefined ranges chosen for each model type. Typically, 50,000 iterations within the hyperparameter space were used along with a 5-fold cross validation technique to reduce overfitting to the data. After the best possible model hyperparameters were found, the model was tested on the validation set which comprised 15% of the original data, and which had not been used to train the model. The reported results indicating goodness of fit are the measurement of the model’s performance in predicting this validation set.

The exception to the above process is the symbolic regression method. This model type was trained using a genetic algorithm and as a result the iterations necessary for a successful randomized hyperparameter search would have been computationally limiting. However, the genetic algorithm mutates by definition, so this is not expected to have unduly impacted the results.

4.2.4 Ordinary Least Squares (OLS) Modeling Method

A linear regression using OLS was used to provide a benchmark for the other modeling methods explored in this work. Because the simulations are non-linear by nature, it was understood that there was only a small likelihood of attaining a high level of accuracy with this class of models. However, the linear regression provides the most interpretable model output of any of the other modeling systems, so it was included in this study. Scikit-Learn’s LinearRegression function was used to produce these models [54].

4.2.5 Random Forest Modeling Method

The random forest regression model is an ensemble of decision trees whose outputs are averaged. The result is a model that is both generalizable and complex enough to provide accurate predictions in high dimensional spaces [61]. Decision tree-based methods are also helpful because their output can be interrogated, as shown in the flowchart in Figure 4.3. In this work, 100 estimators were used for each regression model, corresponding to 100 decision trees, which would make this kind of interpretation difficult. Other methods exist to interpret the output of a random forest regressor, and they are implemented here. The importance of each input parameter can also be determined using methods like recursive feature elimination. Scikit-Learn's RandomForestRegressor was used for this purpose [54].

4.2.6 Neural Network Modeling Method

A multilayer perceptron, or neural network, was fitted to the data. While neural networks are the least interpretable method presented in this study, they have also been shown to be powerful estimators for highly dimensional data. The models presented here were comprised of 3 hidden layers with 5 neurons each. Scikit-Learn's MLPRegressor function was used to train and test these estimators. [54]

4.2.7 Gaussian Process Regression

Gaussian Process Regression (GPR) was chosen as a model type because of its built-in measure of uncertainty. A combination kernel comprised of a Matern kernel and an exponential sine squared kernel were used for training. The sinusoidal attribute of the exponential sine squared kernel was a result of the prior understanding that material properties tend to follow a sinusoidal path as a non-isotropic material is rotated. The Matern kernel additionally allowed the model to effectively capture discontinuities in the solution space. The GaussianProcessRegressor function within the SciKit-Learn package was used to train the models, and a cross validated randomized search was used to find length scale, the Matern ν parameter, and the periodicity parameter for the exponential sine squared kernel. [54]

4.2.8 Symbolic Regression

The most interpretable of models is a function, so a symbolic regression estimator was investigated as a possible method for expressing the data. While a closed-form solution is ideal for interpretability, a highly dimensional feature set can also lead to complex relationships that can be difficult to understand from a practical perspective. The genetic programming implementation of symbolic regression was provided by the gplearn Python library. The genetic component of the method works by creating successive mutations of randomly generated relationships between the independent and dependent variables and choosing the best estimators at each generation to mutate.

4.2.9 Application to Fracture Probability

The aim of this study is to develop reduced-order models that describe the stress state of a material given its material fingerprint and strain level. Doing so allows a user to determine critical information about the material without needing to expend the computational cost to solve an FEM model or to develop an experimental study. The fracture critical stress information recovered from these models can then be used in conjunction with the results of our previous work to determine the likelihood of failure. Figure 3.5 shows the probability corresponding to fracture critical stress levels for the 3 strain levels that the models in this paper were trained to. This study completes the link between the material fingerprint and the fracture probability for that material at a certain strain level.

4.3 Results

The five modeling methods were fit to the training data using a cross validation technique and randomization to tune hyperparameters in all cases except symbolic regression, as described previously. The coefficient of determination values resulting from testing the models against the validation set are shown in Table 4.1. The coefficient of determination, or r^2, makes a comparison between the errors at each data point and the variation observed in the data points. A small ratio between the squared quantities indicates that the model error is less than the average variation in the data points, and results in an r^2 value closer to 1. The most robust results came from fitting neural networks to the data, but the GPR and Random Forest methods also provided excellent results. The ordinary least squares method is included as a benchmark and reasonable predictability was not expected owing to the nonlinear nature of the problem.

In addition to developing models specifically at individual strain levels, the MLP, GPR, and random forest methods were used to develop additional models with strain as a dependent variable in addition to the features of the material fingerprint. Incorporating strain as an additional parameter created a 6-dimensional input parameter space, but also increased the number of data points available for training by orders of magnitude. The scale of the distribution was also included as a second output variable. Table 4.1 also contains the r^2 values for these models. The values improved over those of individual strain levels, owing both to the large variation in material response during large increments in strain and the additional data available for training and testing. The model verifications were performed on a held-out test set. Figure 4.9 and Figure 4.10 show comparisons between FEM database values and predicted model values for selected material fingerprints and variations in both strain and material orientation for the MLP. The predictions from the model provide a continuous representation of the solution, as opposed to the FEM data which was developed using the Morris trajectory scheme and therefore only exists in predefined intervals within the parameter space.

Because the material dependency on nominal strain level is already well established, the models trained to specific strain levels were used to examine the dominant microstructural fingerprint features in the following sections. The neural network-based models were used for this analysis because the r^2 values consistently higher than the GPRs, and the ability of the model to describe the solution space was determined to be more valuable than the measure of uncertainty that the GPRs provide.

4.3.1 Feature Elimination

Recursive feature elimination (RFE) was applied to determine which features can be eliminated from a given model without an impact on the model's predictive power. Features are randomly removed, and recursion is used to drive towards the smallest set of possible features. 5-fold cross validation was used to test the smaller feature sets to ensure that the model's continued efficacy was not random. This method of feature tuning is only available for models that assign weights to features, and the random forest model was the only such type considered in this work. Applying RFE to the random forest models previously described at 3 strain levels resulted in the feature importance ranking described in Table 4.2. Material orientation and hydride orientation are consistently the highest ranked features, followed by volume fraction. Hydride spacing is consistently ranked the least important parameter. This is likely because spacing between hydrides on the axis perpendicular to the hydrides was also controlled by the hydride volume fraction.

4.3.2 Feature Importance

To determine the importance of individual features, a permutation scheme was used. Each parameter was randomly permuted to determine the resulting impact on the model output, measured in the amount by which the coefficient of determination (r^2) decreased when the model was scored against the training dataset with one parameter permuted. Each parameter was permuted a total of 10 times, and the results showing the impact on the coefficient of determination are shown in boxplot form in Figure 4.4. This was calculated for the 2.75% strain neural network model, but similar plots produced for all strain levels indicated similar information, as did the random forest model set. The results correspond to the feature importance ranking for the 3 random forest models shown in Table 4.2. Hydride orientation and material orientation have the highest impact on the model's ability to explain the variation of fracture critical stress in the data. Hydride volume fraction, hydride length, and hydride spacing all had considerably reduced impact on the outcome.

A partial dependence study was also performed to determine the impact of changing various features on the resulting values of fracture critical stress. The average model output at different constant values of the target feature is determined while varying the values for the other features. Figure 4.5 shows the individual dependencies for the three highest ranked parameters: material orientation, hydride volume fraction, and hydride orientation. As material orientation increases, the average fracture critical stress decreases and then increases again. As hydride volume fraction increases, so too does the fracture critical stress, as expected. Finally, as hydride orientation changes from radial to circumferential, the fracture critical stress levels tend to increase.

A contour plot of the partial dependence that incorporates both the material orientation and the hydride orientation is shown in Figure 4.7. This plot indicates that the highest fracture critical stress values tend to occur at both radially and circumferentially hydrided materials with low misorientation with respect to the loading axis, and that the lowest values tend to occur with mixed hydrides and medium misorientation with the loading axis.

Global sensitivity analysis was performed using the Sobol method on the 3.25% nominal strain MLP model. A Saltelli sampler was used with 5000 data points. The SAlib implementation in Python was used for sampling and analysis. [56] The results are shown in Figure 4.8. They indicate a similar result to the previous parameter studies, with the highest indices attached to grain orientation, hydride orientation, and hydride volume fraction. Only small variations between the first-order indices and total-order index are shown, indicating that most of the model variance is attributed to single parameters. Hydride spacing was the least impactful parameter, as also shown in the feature importance study. If 0.05 is taken as the cutoff for an influential parameter [62], then interactions with the grain orientation (texture) parameter are the only second order indices where the upper 95% confidence intervals fall within an influential range. The interactions observed between grain orientation and hydride volume fraction or hydride orientation are reasonable because material texture will impact dislocation accumulations within the material, thereby influencing the degree to which hydride orientation or volume fraction impact the material response (this effect can be observed in Figure 5.9).

4.3.3 Factors Influencing Dislocation Activity

To further understand the role of trapped dislocations in accelerating fracture, the immobilized dislocation density response was also modeled and analyzed to determine the relative importance of different features in the material fingerprint. The same method used to train a neural network for the fracture critical stress predictions was also used to train a model describing the maximum immobile dislocation density response, $\rho_{im,max}$, comprising of the maximum response level observed over all the modeled slip systems for the parent grain material. The training process resulted in a holdout test-set coefficient of determination of 0.98, indicating that the universal function approximator was able to capture the nonlinearities associated with the dislocation density evolution equations effectively. Figure 4.11 shows the results of a feature importance study on this model. Grain orientation is by far the most important parameter and hydride orientations do not seem to influence the maximum activation. This shows that the orientation of the hydrides plays a role in the fracture critical stress predictions because of the geometric interaction between hydride orientations and trapped dislocations, and that the severity of the impact of dislocation accumulations on fracture critical stress can be influenced according to the hydride orientations. The material degradation caused by hydrides spanning the radius of the cladding tube, i.e., radial hydrides, is exacerbated by the accumulation of immobilized dislocation densities at preferential grain orientations.

4.4 Summary

In this work, a database of deterministically modeled crystalline structures was used to find relationships between material fingerprints and stress response. Ordinary least squares, Gaussian Process Regression, symbolic regression, random forest, and multilayer perceptron modeling techniques were evaluated for their performance in representing material fracture critical stress response. The advantages and disadvantages of each kind of model were discussed. The parameters were evaluated to determine their contribution to the models, and to quantify their importance to the stress response more generally. Specifically:

1. Multilayer perceptrons (neural networks) demonstrated the best overall average performance, based on the coefficient of determination.
2. Material orientation and hydride orientation were shown using feature importance to be the most important parameters, as did hydride volume fraction to a lesser extent.
3. Grain orientation had the greatest impact on immobile dislocation density activity.
4. Hydride length and hydride spacing had relatively low impact on the model's ability to predict fracture critical stress, suggesting that future studies might use a coarser representation of these parameters without loss of accuracy.

Table 4.1: Validation Set r^2 Values for Fracture Critical Stress

Model Type	0.75% Strain	2.25% Strain	3.25% Strain	All Strains
GPR	.87	.61	.85	.98
Neural Network	.86	.88	.93	.98
Random Forest	.86	.80	.88	.46
Symbolic Regression	-.03	.06	.31	
Ordinary Least Squares	.50	.44	.51	

Table 4.2: Feature importance ranking for 3 random forest models

Feature	**1.25% Strain**	**1.5% Strain**	**2.75% Strain**
Hydride Length	3	3	2
Material Orientation	1	1	1
Hydride Volume Fraction	2	2	1
Hydride Orientation	1	1	1
Hydride Spacing	4	4	3

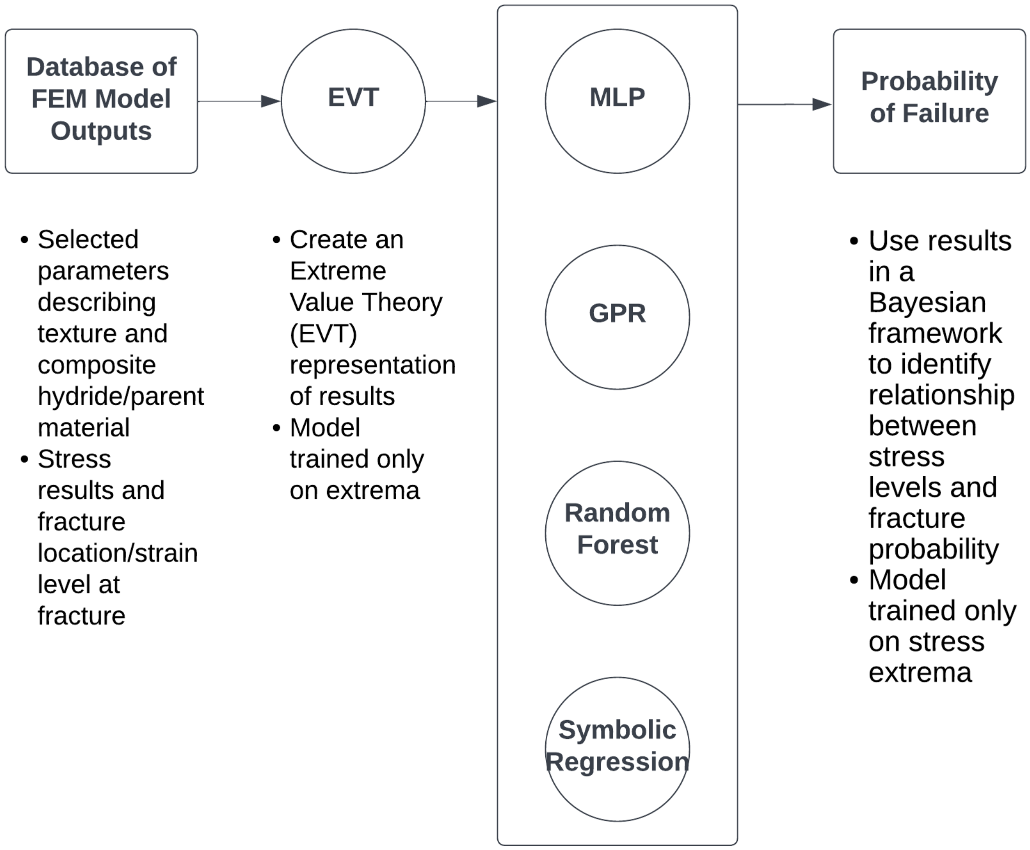

Figure 4.1: **Modeling Process.** The FEM results are distilled into a representation of their extrema, and then various model types were tested to determine which was best suited to model this data.

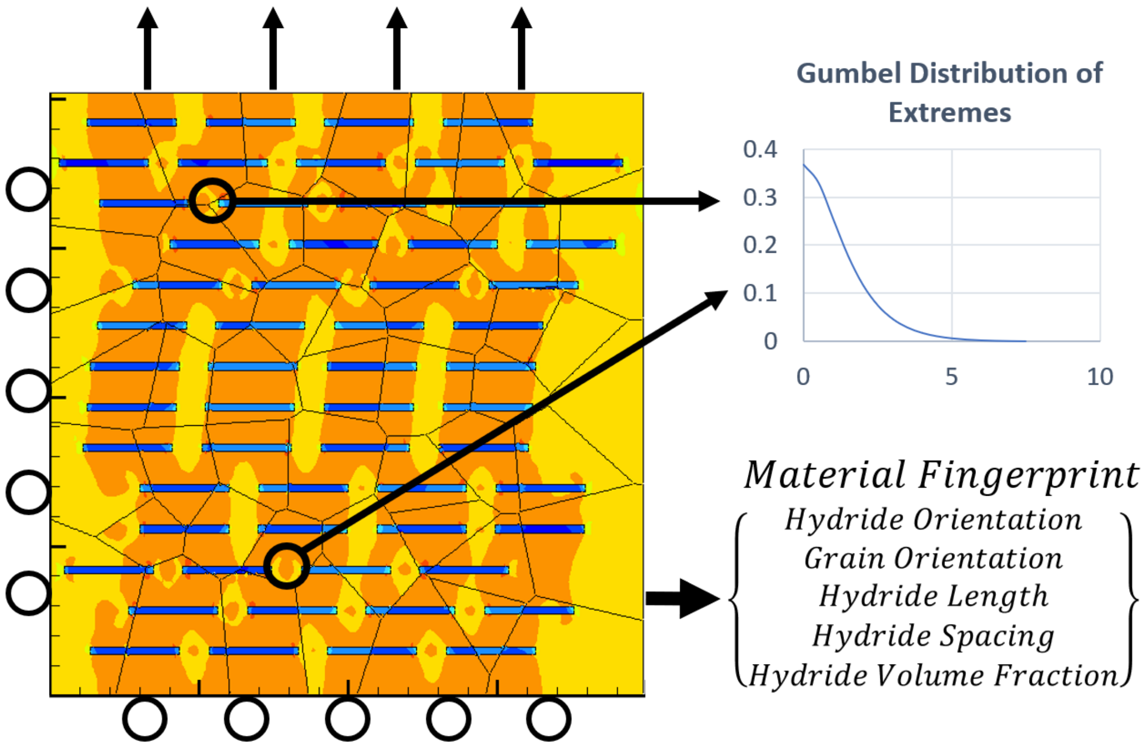

Figure 4.2: **A loading diagram of a typical multiphase hydrided zirconium alloy model.** The material fingerprint and an EVT distribution are extracted from each mesh data point.

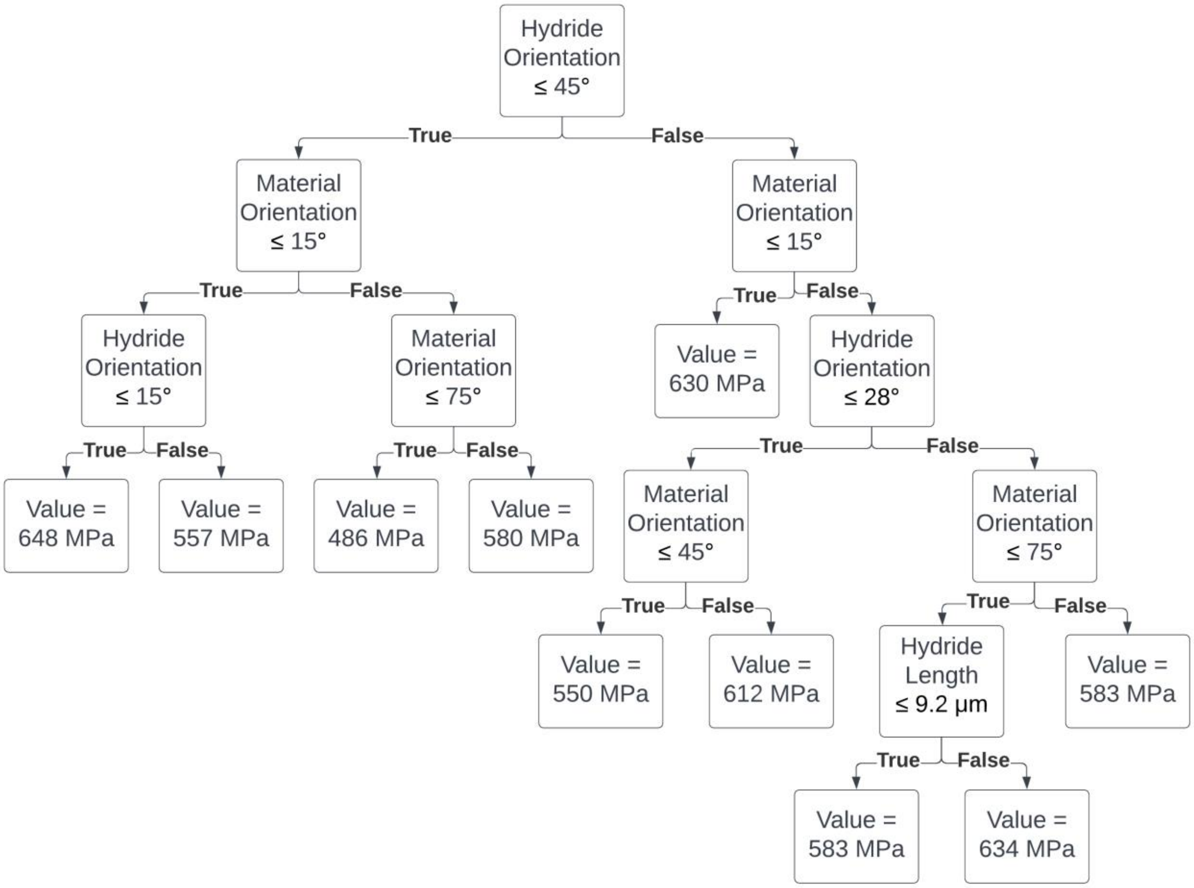

Figure 4.3: **Sample decision tree.** One decision tree from the ensemble used in the 3.25% strain model.

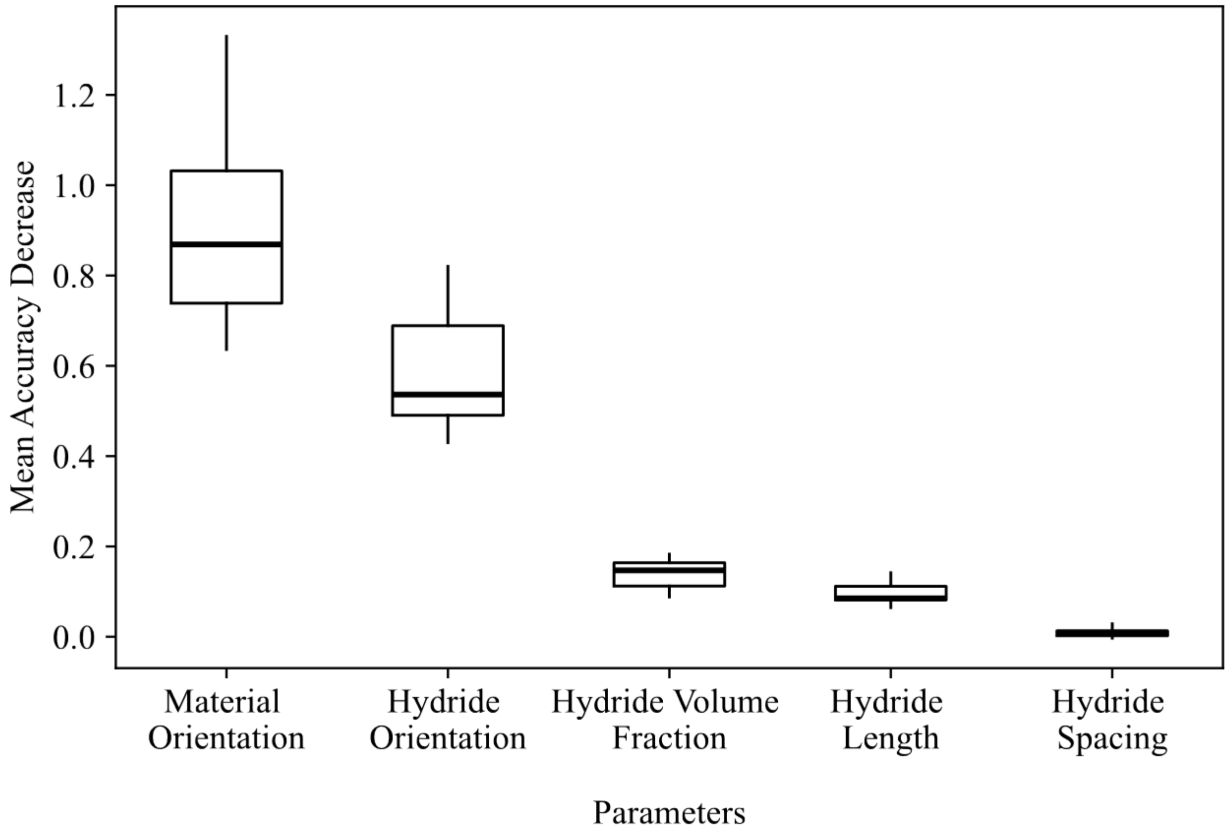

Figure 4.4: **Permutation importance for all parameters.** Calculated for the 3.25% nominal strain MLP model.

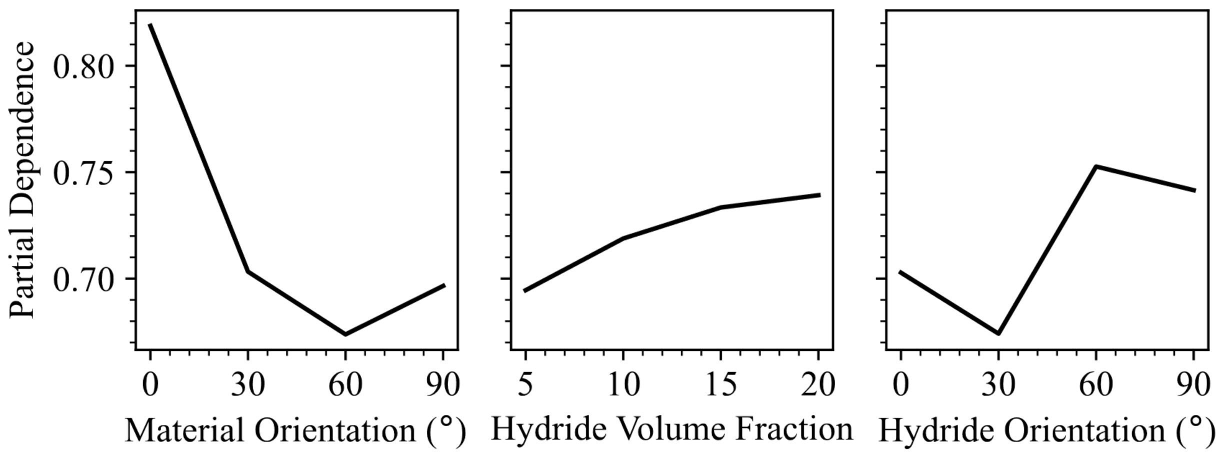

Figure 4.5: **Partial dependence plots for material orientation, hydride volume fraction, and hydride orientation**. Generated for the 3 highest ranked features normalized by fracture stress.

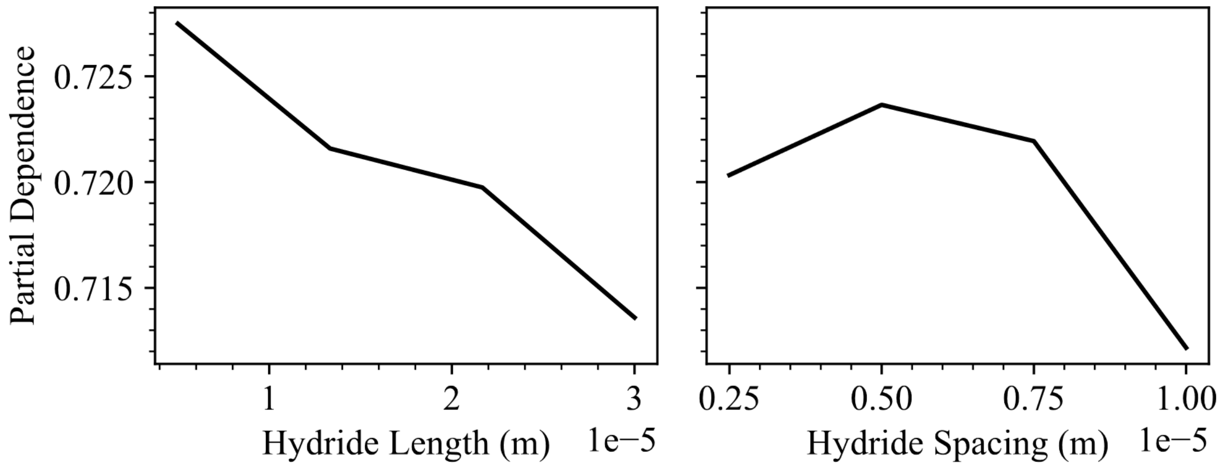

Figure 4.6: **Partial dependence plots for hydride length and hydride spacing.** Normalized by fracture stress.

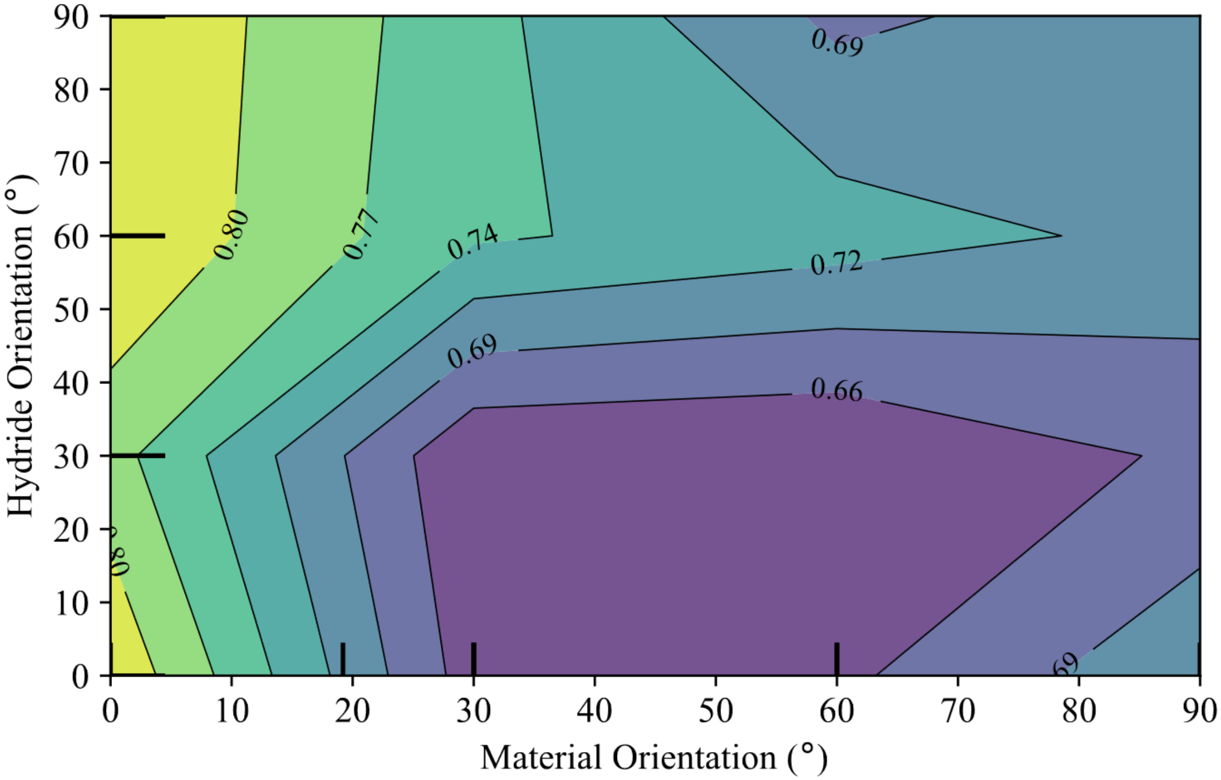

Figure 4.7: **Partial dependence contour plot.** The combined impact of material orientation and hydride orientation are displayed.

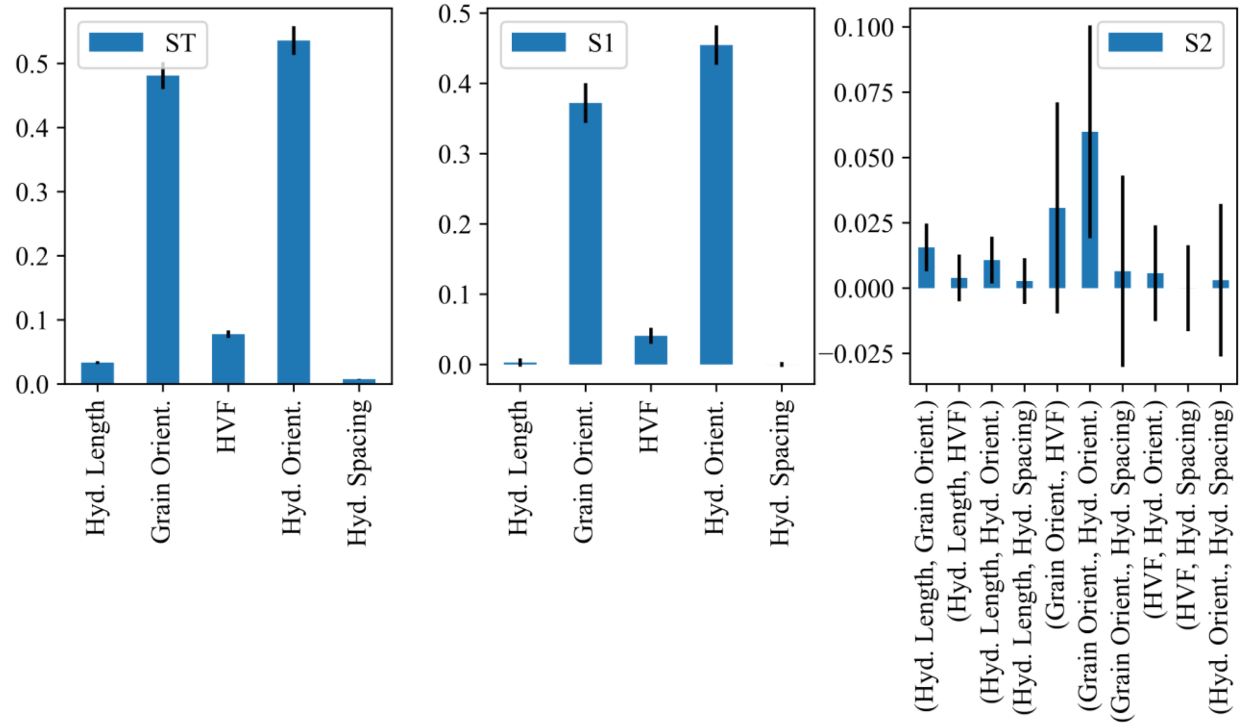

Figure 4.8: **Sobol analysis for material fingerprint showing total effects, first order effects, and second order effects**. Calculated for the 3.25% nominal strain MLP model. 95% confidence intervals are indicated by the vertical black lines.

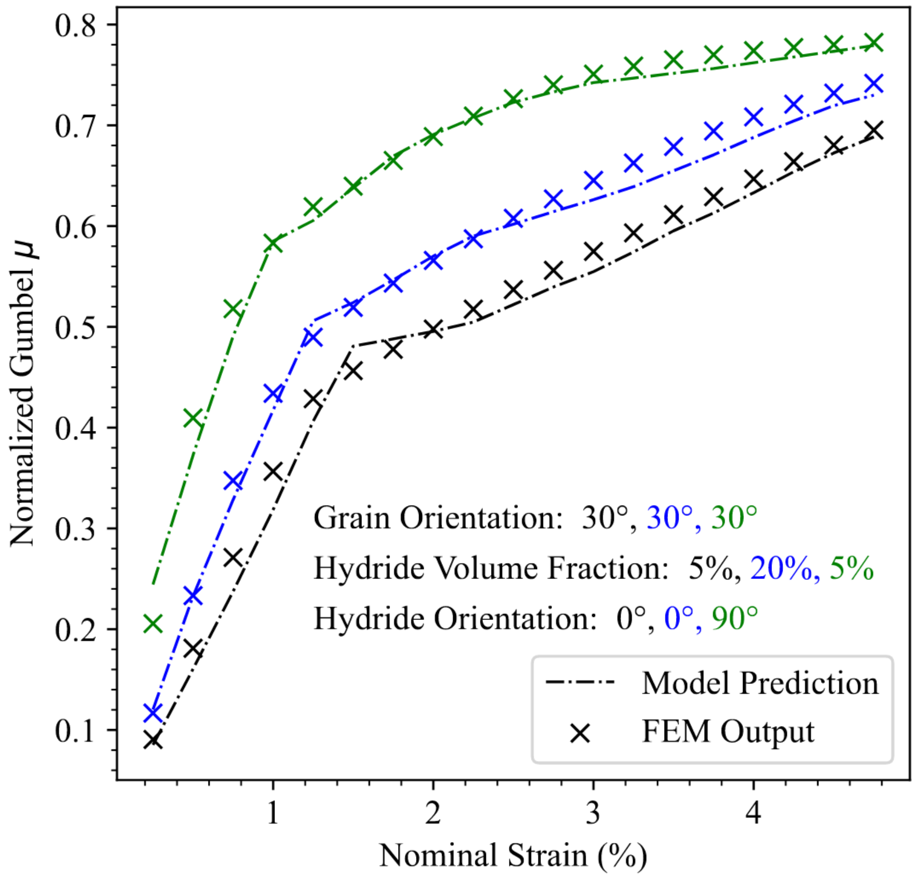

Figure 4.9: **Model verification against strain response for different material fingerprint parameters.**

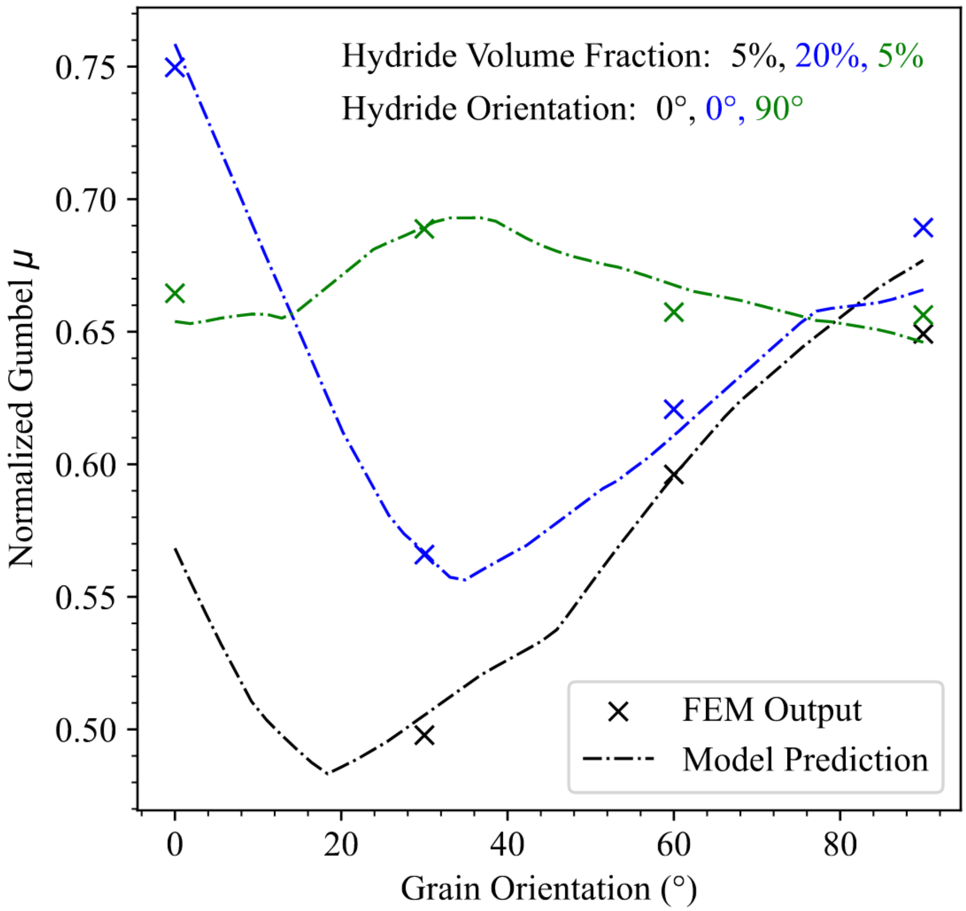

Figure 4.10: **Model verification against variations in hydride volume fraction, hydride orientation, and grain orientation.**

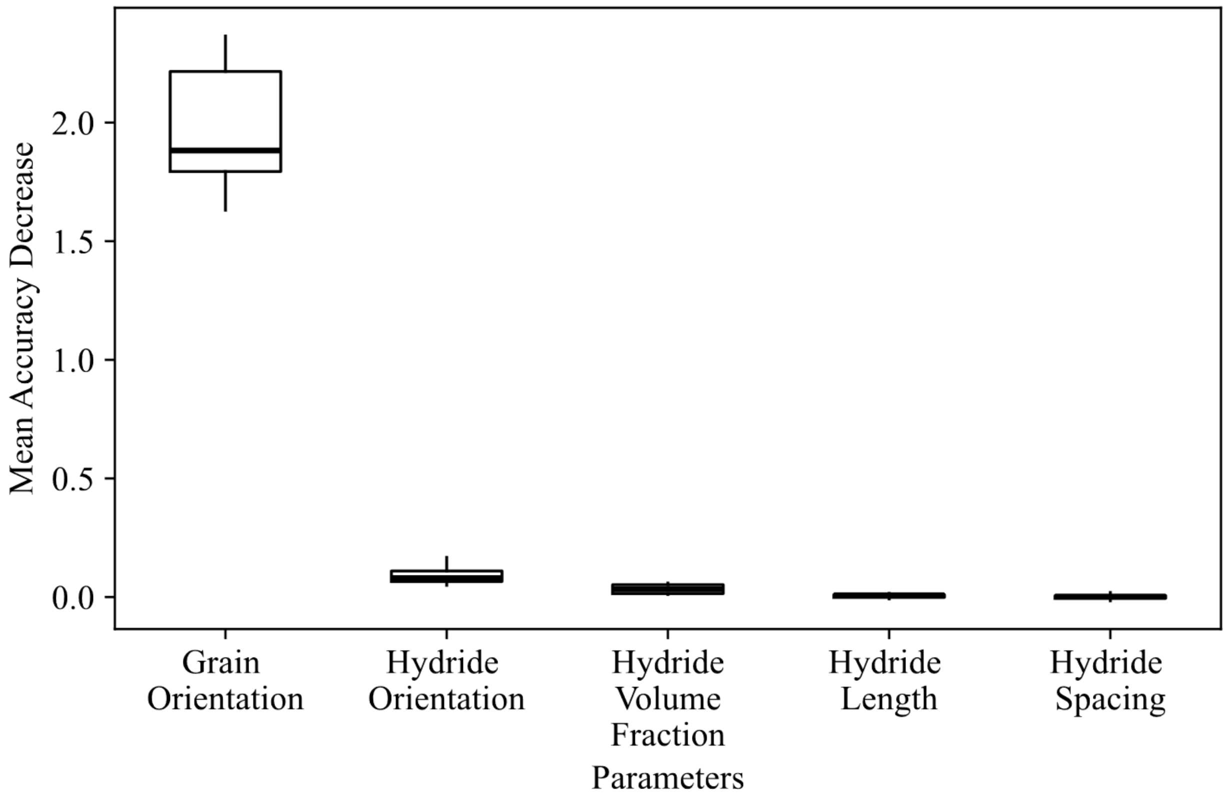

Figure 4.11: **Feature importance study.** Developed for a model trained to predict $\rho_{im,max}$.

CHAPTER 5: Predictions of Representative Localized Hydride Distributions of Strain Responses in Zirconium Alloys

5.1 Introduction

The impact and contribution of individual hydrides on the overall material state has not yet been quantified, and ways in which the material state changes according to variations in bulk material properties such as grain orientations have also not been adequately explored. Furthermore, a statistical framework necessary for describing the material state in the region adjacent to the hydride in a way that can be utilized in larger-scale simulations has never been developed.

Hence, we propose the creation of a database of finite element method (FEM) simulations that characterize a multidimensional solution space of known impactful material properties (a material "fingerprint"). We then examine the regions adjacent to the hydrides using a statistical fat-tailed approach. We fit a neural network to spatially predict distributions of fracture critical stress and shear slip in the hydride-adjacent regions, and we demonstrate the model's efficacy against a hold-out training set. This process is described in Figure 5.1. Finally, we examine the model output to learn about the impact that bulk material properties have on the hydride-adjacent regions. We harness our statistical predictions to provide insight to the expected range of properties in the hydride-adjacent regions.

5.2 Approach

A secondary database was generated by sampling the regions adjacent to each individual hydride within the finite element mesh. Each mesh element whose centroid fell within a region of interest defined by an area extending around the hydride of the same width as the hydride. These centroids were sorted by their angle to the hydride's longest axis. A diagram of the relevant geometric items is shown in Figure 5.2 overlaid on a segment of a finite element mesh used in this study. This process was repeated for every hydride and for every simulation. Meshes typically held approximately 50 hydrides, with variations due to hydride length, spacing and volume fraction. Points from all 4 quadrants around the hydrides were treated individually. The points were grouped in 1^{o} increments and the points corresponding to each group were fit to a Cauchy distribution. The μ and σ values of the fitted distribution were saved as the spatial representation for one angle within one material fingerprint.

The Cauchy distribution was chosen because it is a fat-tailed stable distribution, and therefore better able to model the extreme events at the right tail that can lead to material fracture when compared with a distribution with smaller tails. Prior work has shown that fracture nucleation within hydrided zirconium alloy systems occurs at selected points within a bulk system, and fracture propagation then occurs until material rupture [32]. Therefore, accurately characterizing these anomaly regions is critical to understanding the behavior at the extremes that leads to fracture. The SciPy Python package was used to fit these distributions [53].

To characterize these datapoints, a multilayer perceptron, or neural network, was used. The data was split into test and training sets using 80% of the data for training and the remaining 20% for testing. The training set was used to train the models using a randomized cross validation technique, and the test set was used as a holdout set to verify the model accuracy after fitting was complete. The neural network was trained using the Scikit-learn package in Python [54], and consisted of 3 hidden layers of 64 nodes each. The network had a composition as follows:

$$\mu, \sigma = \mathcal{N}(\theta, \phi_G, \phi_H, \nu) \qquad 5.1$$

where θ represents the angle around the hydride from the longitudinal axis of the hydride. Although hydride length and hydride spacing are used to generate the database, prior work has shown that their importance in the material response is minimal when compared with the other parameters.

5.3 Results and Discussion

One multi-output neural network was trained to predict the location parameter μ and scale parameter σ parameter for the Cauchy distribution. The r^2 value for the model against the holdout test set was .86. To query this model, an array of values representing the material fingerprint and angle of interest were used to gather the μ and θ of the Cauchy distribution. The percent point function as used to determine the relevant values (e.g., of normalized fracture critical stress) at a percentile of interest, such as the 90^{th} percentile.

The effect on fracture critical stress in the hydride adjacent areas of variations in grain orientation were studied. Figure 5.3 shows the plotted μ location parameters surrounded by an area bounded by the 90^{th} and 10^{th} percentile values for a HVF of 5%. This provides an estimate of the expected bounds of the normalized fracture critical stress values for each material. The representation of the radial hydride is almost universally higher than that of the circumferential hydride for the 0º and 30º cases, which is consistent with experimental literature reports that materials containing radial hydrides have lower fracture toughness when compared to those with circumferential hydrides [11]. Both the normalized stress levels and the variation to the 90^{th} percentile of the distributions are shown to vary with respect to the grain orientation. Preferential orientations for the lowest normalized stress levels are 30º and 60º.

Contour plots were developed to visualize the normalized stress levels in the hydride adjacent regions. Figure 5.4 shows the effect of changing both grain orientation (in the vertical direction) and hydride orientation (in the horizontal direction). Clear preferences for stress regions depending on grain orientation and hydride orientation can be observed, and it is likely that a hydride's tendency to crack in either the tip region or along its longitudinal axis is determined by these two parameters. The highest fracture stresses around the circumference of a hydride occurred mostly in the crack tip region for radial hydrides at higher grain orientations, and for circumferential hydrides generally.

The variations in individual hydride response as population-level parameters changed was also studied. Figure 5.5 shows the difference between two identical material predictions, in all aspects except for the hydride volume fraction. Both stress levels and the observed changes in the expected stress values near the extreme were studied. The 5% HVF case illustrates that lower variations and extrema in stress can be expected when compared to the 20% HVF case. The location parameters, μ, indicated that typical stress levels can be expected to increase by approximately 15% at the hydride adjacent region as hydride volume fraction changes, and the variation in those stresses because of the impact of greater hydride volume fraction can be expected to increase substantially.

Figure 5.6 and Figure 5.7 repeat the previous analysis for shear slip, or the sum of dislocation activity across all slip systems. A similar neural network was trained on the parameters of a Cauchy distribution, with a resulting r^2 value of .89 on the held-out test set. Figure 5.6 shows that the dislocation activity for circumferentially oriented hydrides tends to be equal to radial hydrides, except for localized accumulations along the longitudinal axes of the hydrides. This holds for all grain orientations except for 90°, where a broad increase of dislocation activity near the hydride tips is present for radial hydrides. The increased shear slip allows greater relaxation of stresses in the hydride adjacent area and allows circumferential hydrides to be less likely to nucleate cracks.

Figure 5.7 provides more spatial context for the previous results. Zones of high shear slip concentration are observed at the crack tips for both radial and circumferential hydrides, with additional concentrations for mixed hydrides alongside the longitudinal axis. This may be indicative of additional misfit strains for hydrides that are not parallel to the loading axis and shows that these hydrides are a source of dislocations for the parent grain structure. This idea is further elucidated in Figure 5.8, where the maximum values of shear slip are plotted for selected material configurations both within the hydrides and external to them at different grain orientations. The accumulated plastic strain increases with grain angle and displays some preference along the longitudinal axis of the hydrides. Although the gradient across the boundary is minimal, the shear slip in the matrix is typically higher than that of the hydride, indicating that most of the deformation due to misfit and interface effects occurs within the matrix. This is likely a result of reduced mobile dislocation generation in the 12 fcc slip systems, compared with the 24 h.c.p. slip systems that are more easily able to accommodate ductility, in addition to the OR between the hydride and matrix materials.

To better understand the effect of each material type on fracture nucleation and to provide the context needed for understanding the link of hydrides to crack nucleation, the crack initiation sites were examined for each simulation in the database to determine if selected material parameters impact the crack nucleation location. Overall, there was a 3:1 ratio of cracks initiating in the hydrides as opposed to within the matrix material. A more granular description of crack formation is provided in Table 5.1, where the percentage of cracks that nucleate within the hydrided areas is provided for different values of hydride orientation and grain orientation. Grain orientation is highly impactful in this metric, with 30° and 60° grain orientations associated with near certain crack nucleation within the hydrides, and 0° and 90° grain orientations associated with crack nucleation outside of the hydrides. This is a result of the hydride cleavage planes being more closely aligned with the loading direction, given their OR with respect to the matrix grains, in the 30° and 60° cases. The basal plane is oriented towards the loading axis in the 90°

case, creating greater preference for ductility and shifting the likelihood of cracking towards the matrix material.

To provide further context for the spatially dependent phenomena observed in the modeling of fracture critical stress and shear slip, the maximum immobilized dislocation densities, $\rho_{im,max}$, across all slip systems in the hydride adjacent region were examined. Cauchy distributions were fitted to specific angular ranges, and the resulting 90th percentile data points are shown in Figure 5.9 for a grain structure with varying orientations and radial hydrides. The figures clearly indicate that the greatest dislocation activity occurs in the vicinity of the hydride tips. Hydride orientation was not shown to significantly impact dislocation response. The dislocation pileups near the hydride tips are the driving force behind excess stress development and translate into an increased susceptibility for crack nucleation. The matrix material exhibited the greatest $\rho_{im,max}$ values in the 90° grain orientation, in which the basal plane is parallel to the loading axis and immobilized pileups are most likely to cause fracture in the matrix. When taken in context with the results in Figure 5.8, the results show that hydrides and the immediately surrounding material are sources for mobile dislocation activity that can contribute to crack blunting, and that the matrix material in vicinity of the hydrides tends to exhibit the greatest dislocation immobilization regardless of grain orientation, which reduces the fracture toughness of the parent material.

5.4 Summary

To understand the link between local hydrides and populations of hydrides, a statistical approach was undertaken to examine the impact of the material fingerprint on the response of singular hydrides. The single hydrides were statistically represented using spatially defined Cauchy distributions in the region directly adjacent to the hydrides. Neural networks were used successfully to describe the spatial and material parameter dependencies of the hydride response. The results were examined to learn about the response of single hydrides and the link between single hydrides and populations of the same. In particular:

1. Hydride volume fraction was found to influence the both the fracture critical stress response and the immobilized dislocation density evolution, with immobilized dislocation densities increasing threefold as HVF changes from 5% to 15% for radial hydrides.
2. Buildups of fracture critical stress levels were spatially observed at either the hydride tip or along the longitudinal axis of the hydride depending on both grain orientation and hydride orientation, indicating that these material parameters drive a preference for where crack nucleation might occur.
3. Dislocation activity was identified as being similar in magnitude within the hydride and external to the hydride, with matrix activation slightly higher. This indicates that hydrides may serve as dislocation sources within the bulk material.
4. An analysis framework was developed that can be used to characterize any multiphase or composite material system.

Table 5.1: Percentage of cracks nucleating within hydrides for different material properties.

		Hydride Orientation			
		0° Radial	30°	60°	90° Circumferential
Grain Orientation	0°	33%	66%	69%	38%
	30°	100%	100%	92%	96%
	60°	100%	100%	100%	87%
	90°	43%	80%	22%	38%

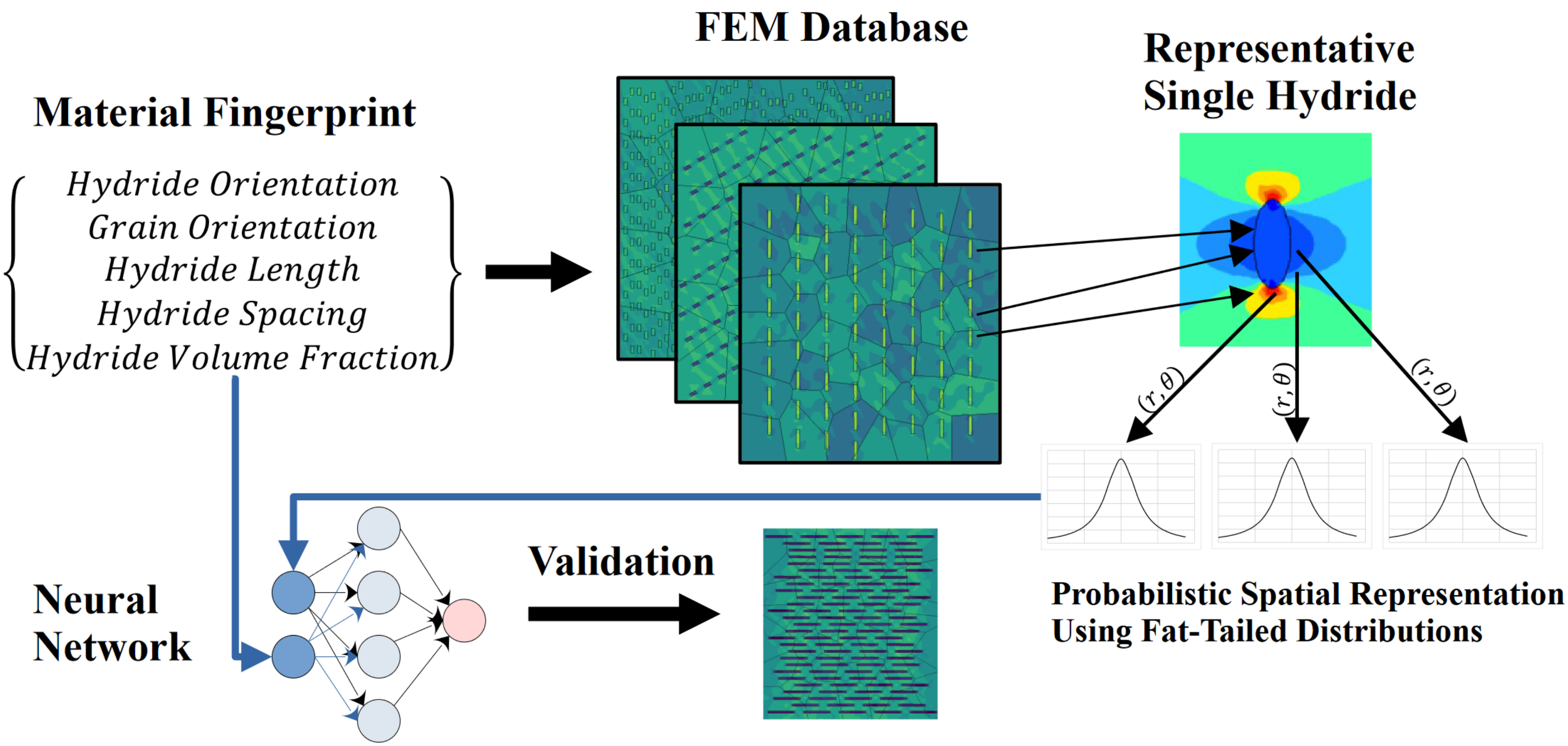

Figure 5.1: **Diagram of method used to sample data and train a model representing spatial hydride response.**

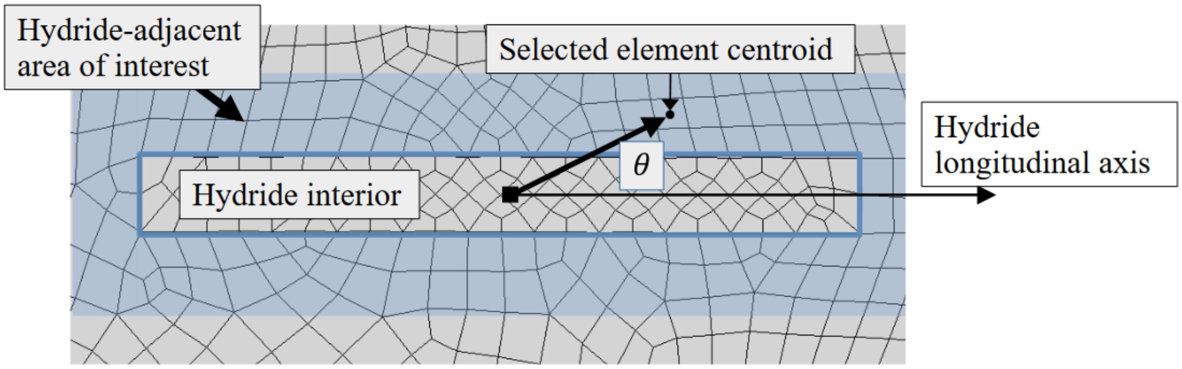

Figure 5.2: **Hydride adjacent area sampling method.** Elements were sampled within a hydride-adjacent area defined by the hydride width.

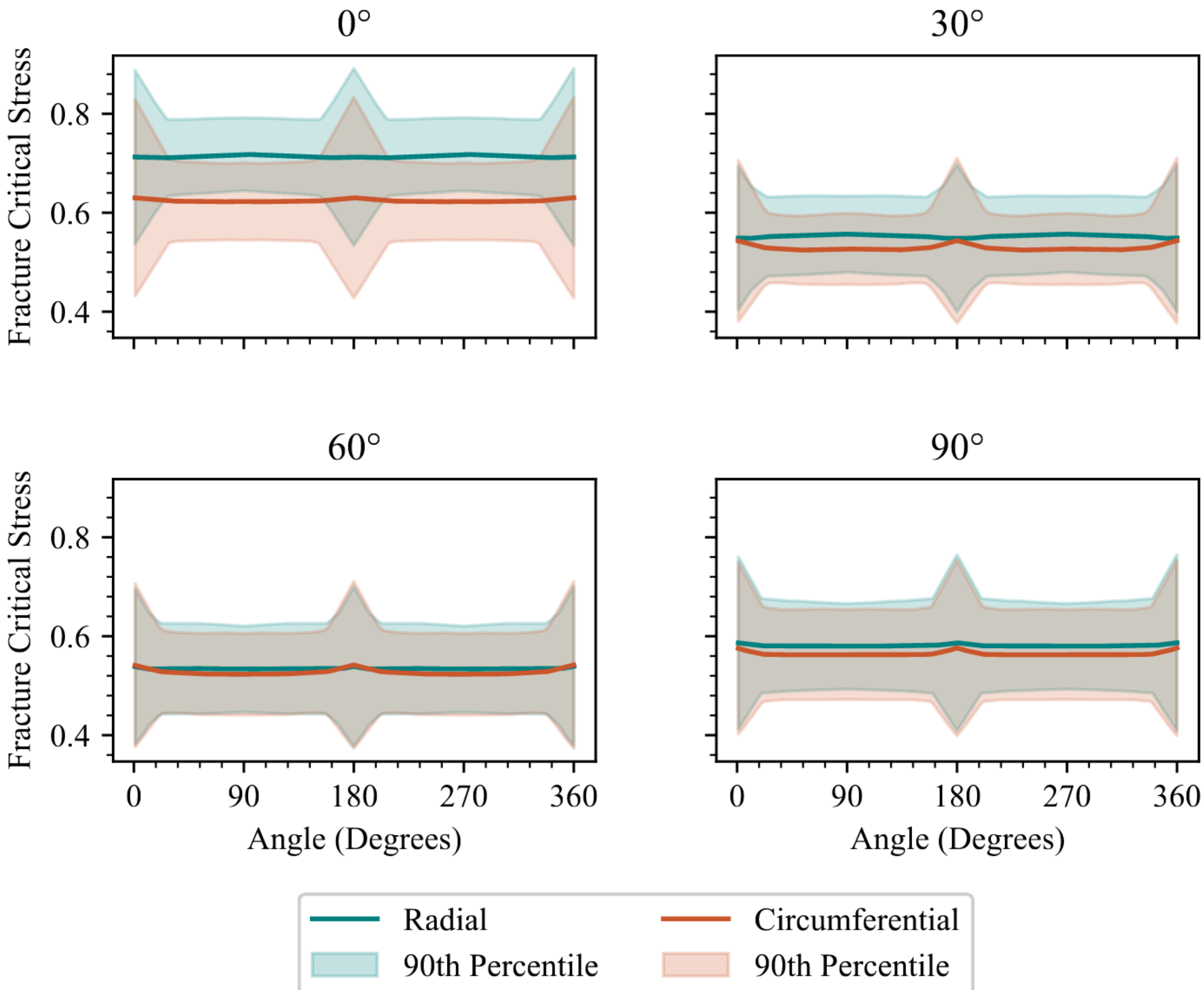

Figure 5.3: **Comparison of normalized fracture critical stress between radial and circumferential hydrides**. A representative sample with 5% HVF normalized fracture critical stress response at 3% nominal strain and at 4 different grain orientations: 0º, 30º, 60º, and 90º. Upper shaded limits indicate the 90% percentile of the fitted Cauchy distribution, and lower shaded limits indicate the 10% percentile.

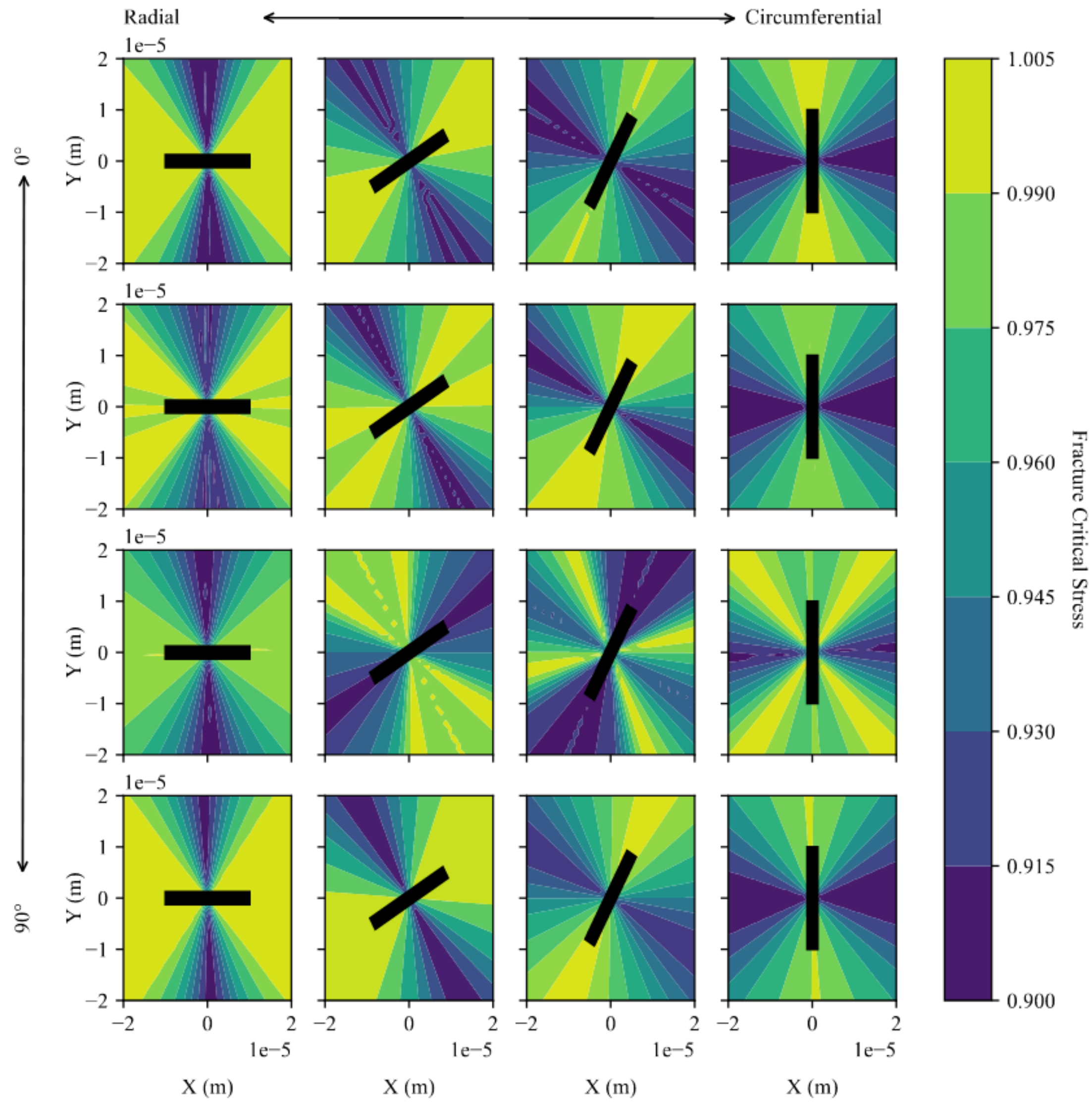

Figure 5.4: **The 95th percentile contours of spatially fitted Cauchy distributions.** Hydride orientation and material orientation variations displayed for a 5% HVF case. Hydride orientations span from radial on the left side to circumferential on the right side. Although the model was trained on radially defined data points within a region within one hydride width from any point on the hydride, the plots are purposefully expanded for clarity.

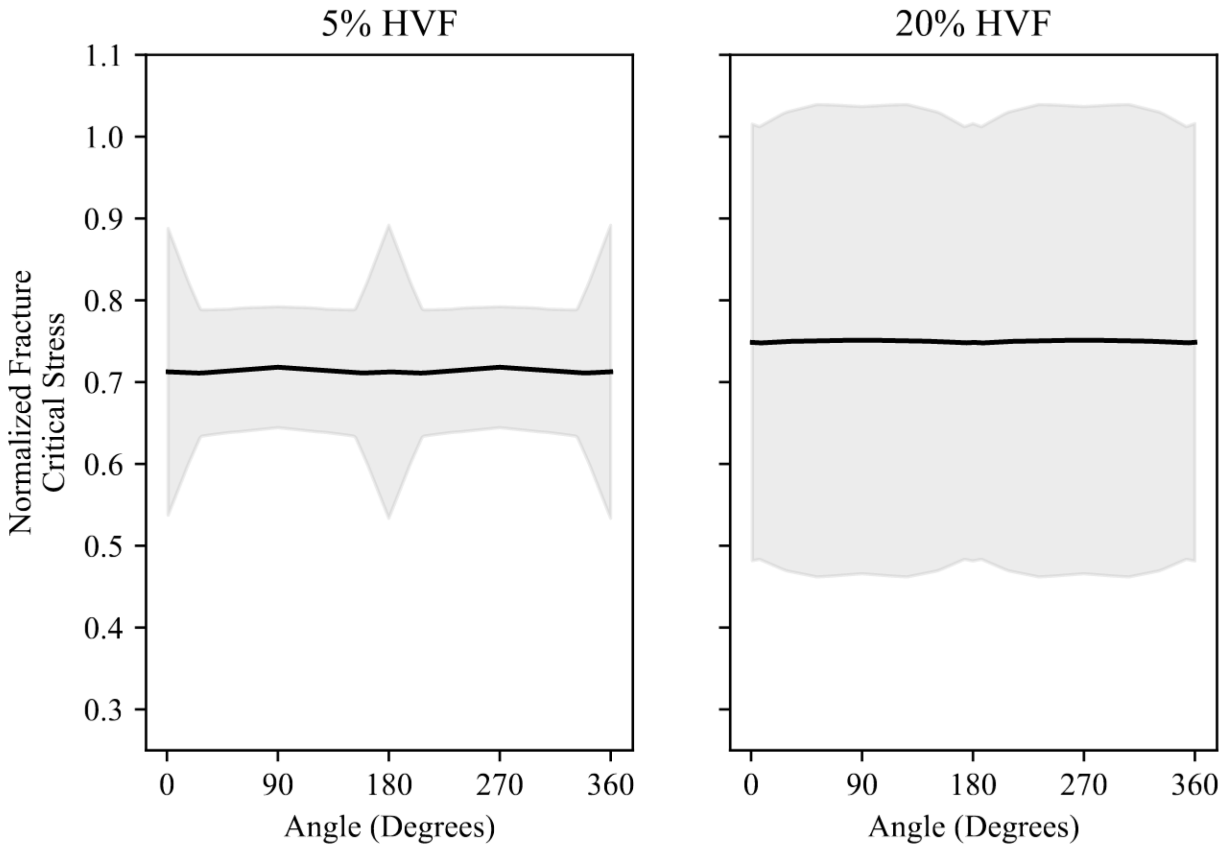

Figure 5.5: **Differences between distribution-derived predictions of normalized fracture critical stress for variation of hydride volume fraction (HVF) from 5% to 20%.** Grain orientation 0º, hydride orientation 30º. The upper and lower edges of the gray regions correspond to the 90th percentiles and 10th percentiles of the predicted normalized fracture critical stress distributions.

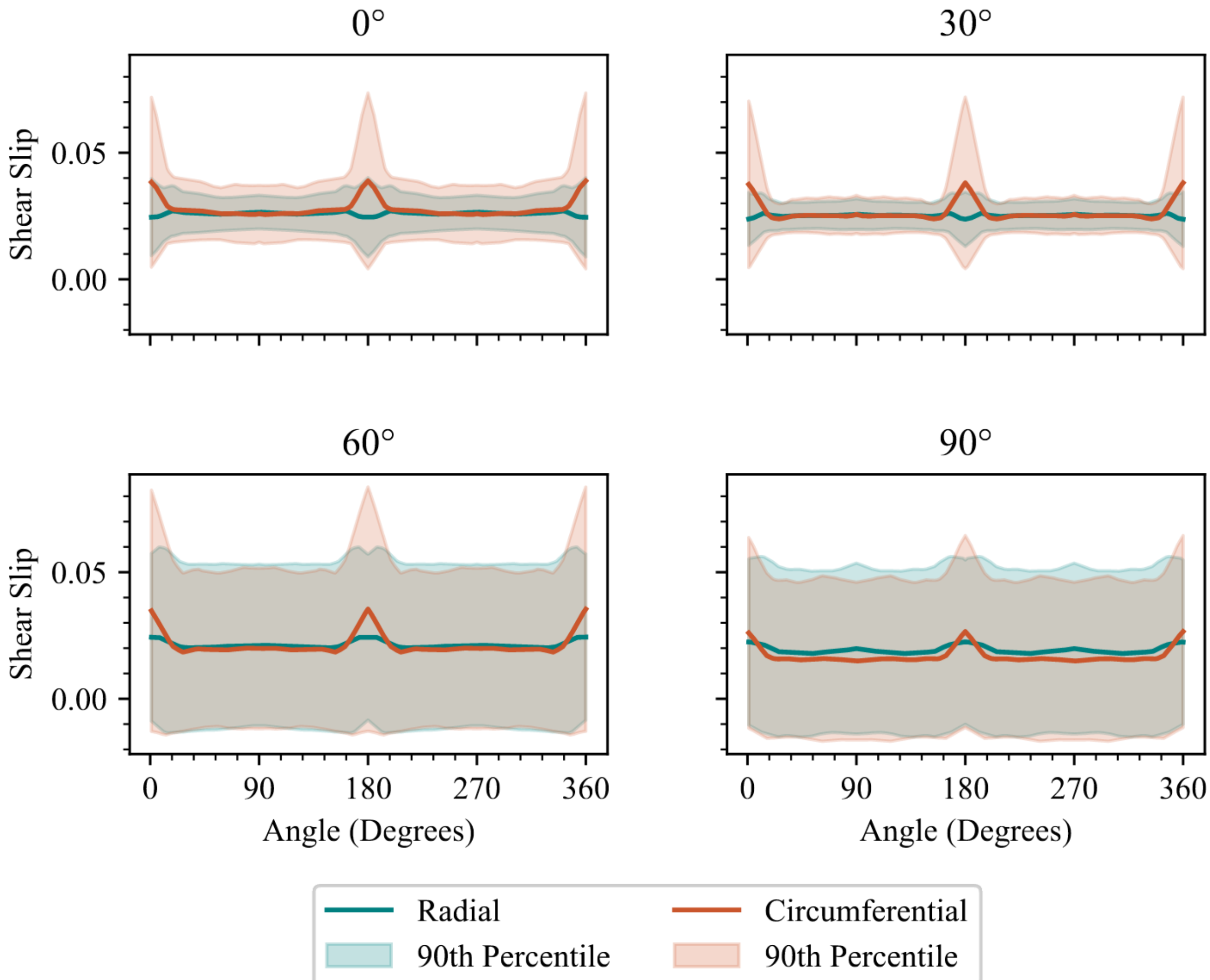

Figure 5.6: **Comparison of shear slip between radial and circumferential hydrides.** 5% HVF shear slip response at 3.25% nominal strain and at 4 different grain orientations: 0º, 30º, 60º, and 90º. Upper shaded limits indicate the 90% percentile of the fitted Cauchy distribution, and lower shaded limits indicate the 10% percentile.

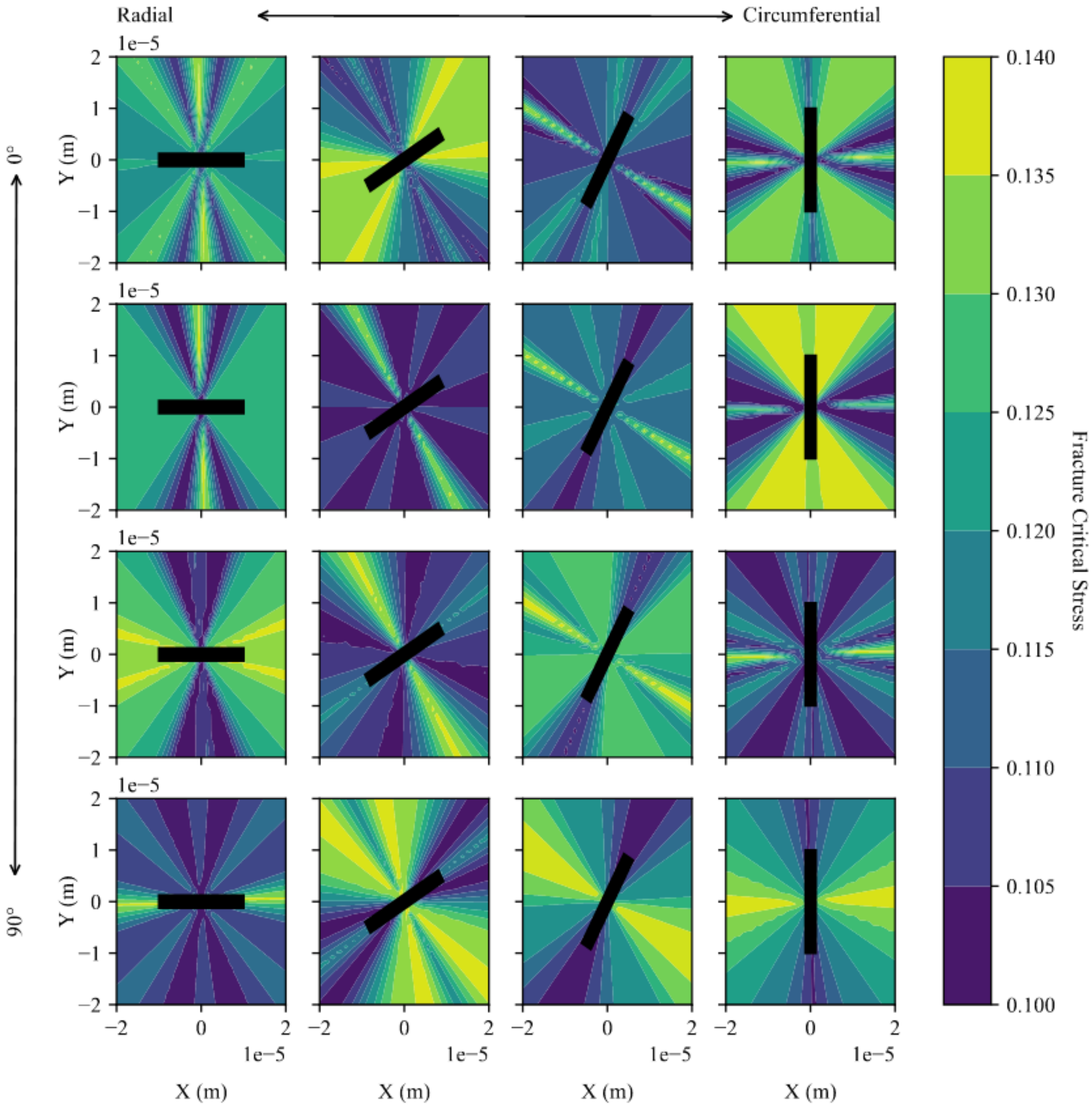

Figure 5.7: **The 95th percentile contours of spatially fitted Cauchy distributions**. Variation in shear slip is shown as both hydride orientation and material orientation change for 5% HVF. Hydride orientations span from radial on the left side to circumferential on the right side. Although the model was trained on radially defined data points within a region within one hydride width from any point on the hydride, the plots are purposefully expanded for clarity.

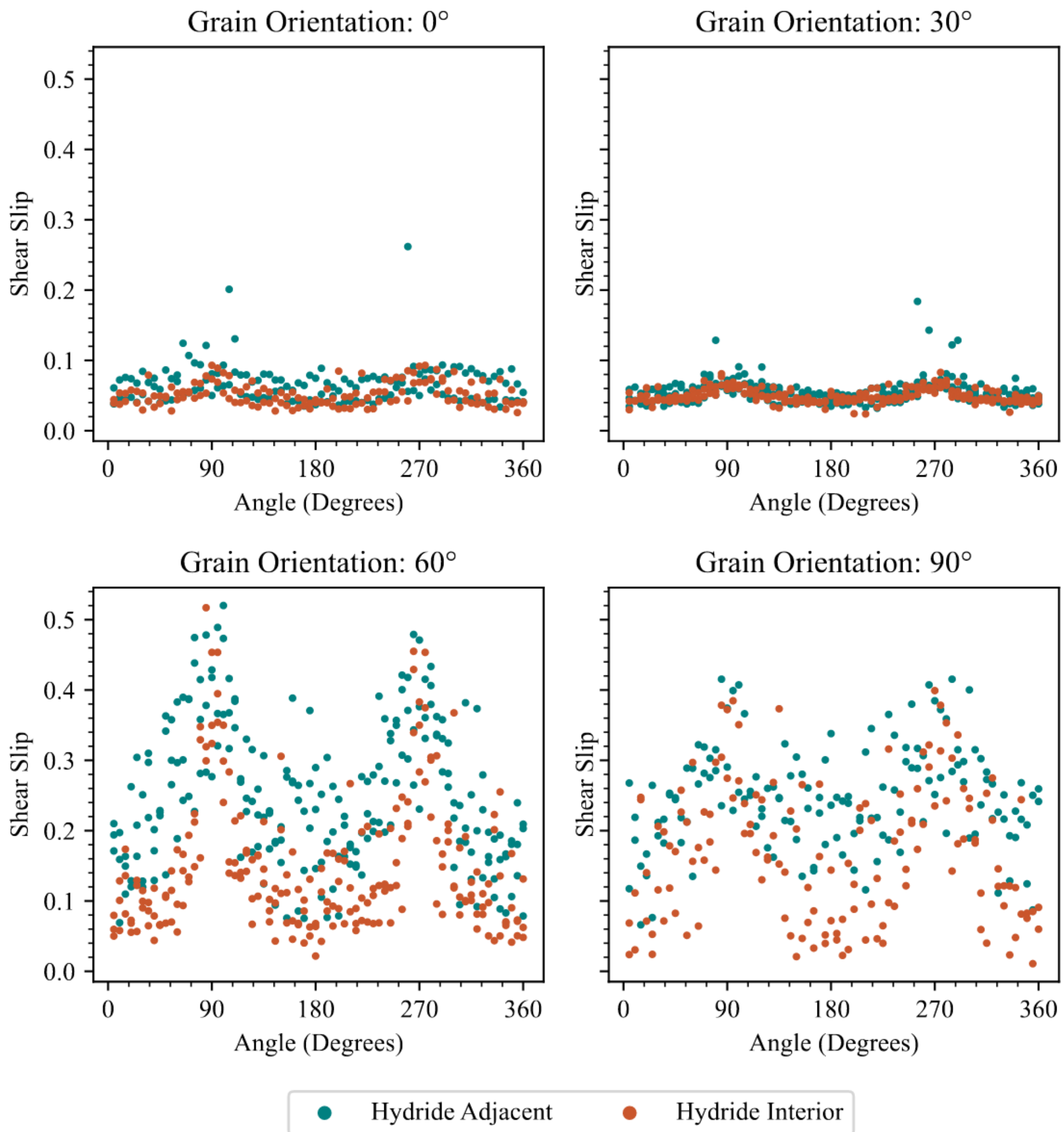

Figure 5.8: **Comparison of shear slip at different grain orientations.** Maximum values of shear slip at each angle from the hydride centroid are displayed in the data. Separate colors representing the hydride adjacent and interior regions are shown to indicate generally higher accumulated plastic strain in the regions surrounding the hydrides compared with the hydride interiors.

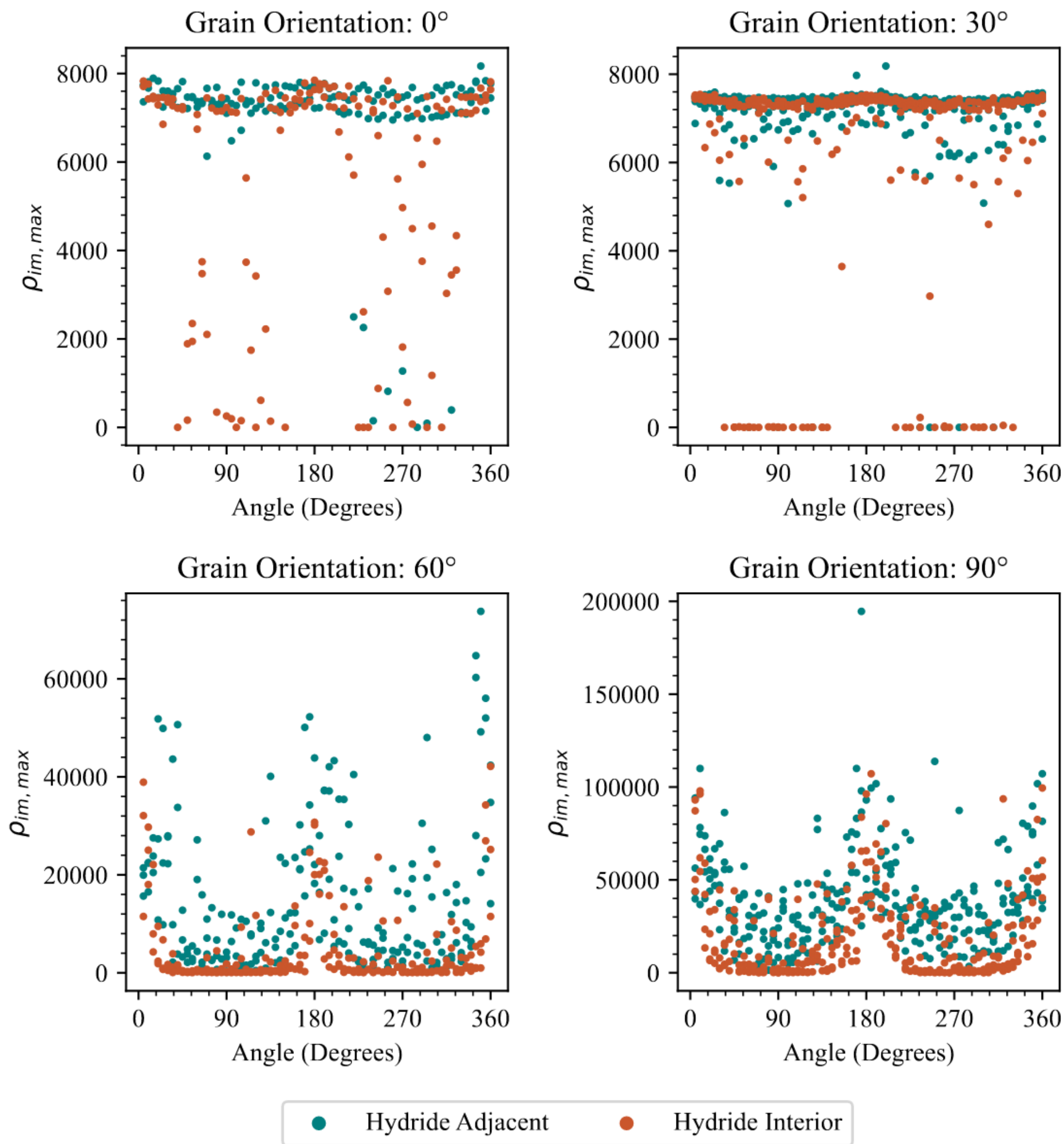

Figure 5.9: **Data showing the fitted Cauchy distributions of the 90th percentiles of $\rho_{im,max}$ as a function of angle around the hydride, for radial hydrides.**

CHAPTER 6: The Thermo-Mechanical Fracture of Chromium Film-Zirconium Substrates

6.1 Introduction

The development of fuels with enhanced accident tolerance can mitigate the loss of active cooling in a reactor core for a considerably longer period of time and to higher temperatures than current fuel system while maintaining or improving fuel performance during normal operations. Key requirements for any proposed advanced fuel material system should result in nuclear fuel cladding with slower reaction kinetics with steam (reaction rates and heat of oxidation), slower hydrogen generation rates, and significantly improved cladding thermo-mechanical properties than existing zirconium-alloy monolithic system [63]. One possible approach to address these challenges is the modification of monolithic zirconium-based alloy claddings with phase vapor deposited (PVD) chromium coatings to inhibit the rapid oxidation that occurs during elevated-temperature steam exposure [1-2].

Different chromium-based coatings, such as FeCrAl, for thicknesses, ranging from 4000 to 7000 Å, that have been layered on zircaloys, have shown significant oxidation delays of up to three hours in comparison with monolithic zircaloys (see, for example, [3]). These preliminary experimental results have been based on four-point bending tests, high-temperature steam exposure, and autoclave testing. However, the specific material mechanisms that result in these oxidation effects still require investigation. It is also not clear what the ideal layer thicknesses for high temperature environments would be, and how cooling losses would be affected by film stability and cohesion for zircaloy substrates with different hydride populations. These hydrides can result in zircaloy substrate cracking, which would also affect coating cohesion. Furthermore, all of these interrelated failure modes would be significantly affected by the thermo-mechanical mismatches between the bcc chromium-based coating structure and the hcp zircaloy substrate. In this chapter, we introduce a validated computational framework to understand how chromium-based coating fractures occur for different mechanical loading conditions due to the different crystalline structures pertaining to the chromium (bcc) film and the zirconium (hcp) substrate. We further investigate how to control coating adhesion at high temperatures to avoid delamination through tracking how simultaneous and multiple coating and substrate cracks can interact and affect interfacial behavior. Finally, our models provide insights to how the higher strength and moduli of chromium-based coatings influence the overall thermo-mechanical response of coated cladding tubes when tested in LOCA conditions, such that optimal thicknesses can be determined to avoid cladding rupture**.**

6.2 Results and Discussion

A microstructurally based finite-element approach that incorporates the dislocation-density crystalline plasticity and fracture methodologies was used to understand and to predict the fracture behavior of Cr coated samples [64]. We validated the model with the experiments of [64]. A 1 millimeter by 1 millimeter sample was modeled with a 10 μm thick chromium layer. The same dimensions and grain morphology were maintained as the experimental sample. The average Zr4 grain size was approximately 10 μm, which is consistent with experimental aggregates. [49] The model is shown in Figure 6.1. A more detailed scale model was also developed that allowed further investigation into the interactions between the chromium coating and Zr4 substrate. A key difference was the addition of Voronoi tessellations to model the grain structures of both the Zr4 substrate and the chromium coating. In comparison with the model pertaining to the experimental validation, where a homogenous material representation was chosen for the chromium coating, this scaled model includes the individual chromium grains and their axially elongated features.

Based on the results of the first aggregate model, the results indicate a good correlation with the experimental values obtained by Brachet et al. [64] Figure 6.2 shows a comparison of the experimental and simulated stress/strain curves. The material response is accurately represented through the nonlinear region and to failure. The cracking characteristics of the simulated material were also found to be consistent with the observations of [64]. These results demonstrate that the cracks tend to form in the coating and then propagate through the material.

After the model accuracy was validated, the smaller scaled version of the model with the elongated chromium grain aggregate was investigated. The calibrated material properties were utilized for a detailed representation of the interface between the chromium coating and Zr4 substrate. This included elongated chromium grains with structures typical of PVD chromium. [64] At approximately 3.7% nominal strain, one crack had propagated throughout the entire coating material (Figure 6.4). Only one crack appeared in the small-scale model while the larger scale model cracked in multiple locations at once. This indicates that grain morphology and orientation have a significant effect on failure nucleation. Microcracks additionally formed at some of the Zr4 substrate grain boundaries that were within 30 microns of the substrate surface. The results indicate that the chromium layer is a key contributor to crack development and material failure in PVD coated Zr4. The chromium grains were elongated perpendicular to the loading direction, which leads to a brittle material response. Furthermore, some cracks form in the substrate material close to the surface and then propagate through the outer layer. (Figure 6.5)

To further understand the mechanisms behind the crack nucleation of this material, a larger scale model was studied with idealized representations of both the Zr4 and the chromium coating. Shear slip (Figure 6.6) and dislocation density on a pyramidal <c+a> slip system (Figure 6.7) are depicted. Shear slip is a measure of the accumulation of plastic strain in the material, and a gradient is evident between the chromium coating and the Zr4 substrate. This indicates that accumulations of dislocations are likely in the coating region, and the immobilization of these dislocations can lead to dislocation pileups and crack nucleation. The pyramidal <c+a> $(0\ \bar{1}\ 1\ 1)$ $[\bar{1}\ 2\ \bar{1}\ 3]$ immobile slip system (existing only in the hcp Zr4 substrate) is unevenly distributed at the interface between the substrate and coating, indicating uneven plastic strain near the interface. This indicates that the coating influences the response of the substrate material even before crack initiation and could be the driving force behind the microcracks observed at the boundary between the substrate and coating.

6.3 Summary

A microstructurally based finite element modeling system was used to predict and understand the fracture characteristics at different length scales of thin chromium film on a Zr4 substrate. The predictions were validated with experimental observations and measurements. Transgranular fracture modes first nucleated in the chromium layer and propagated to the substrate. Gradients of accumulated plastic strain (shear slip) were observed between the chromium coating and Zr4 substrate, and are a driving force for crack nucleation at the interface. These results indicate that the chromium coating can delay the onset of failure in zirconium substrates or claddings.

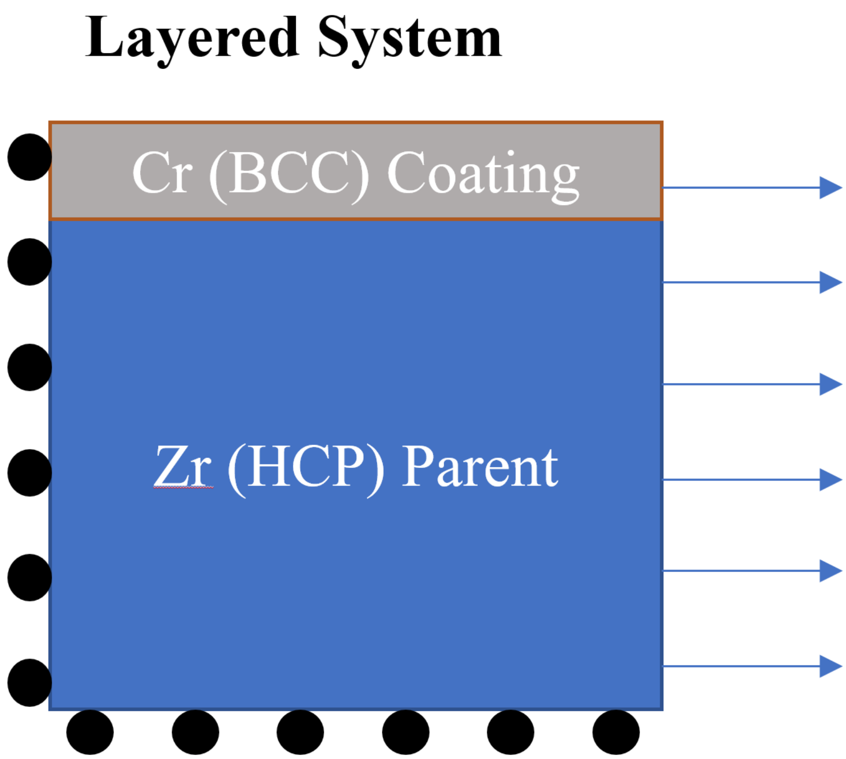

Figure 6.1: **Coated system description.** Not to scale.

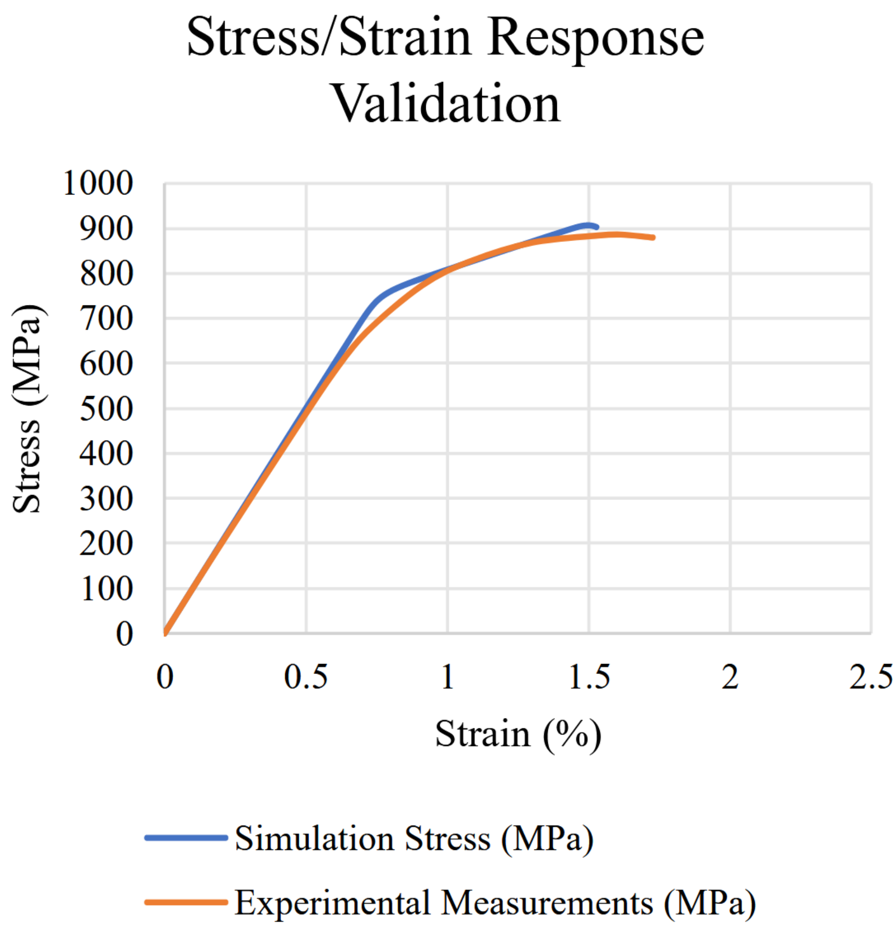

Figure 6.2: **Simulated stress/strain response compared with experimental results.**

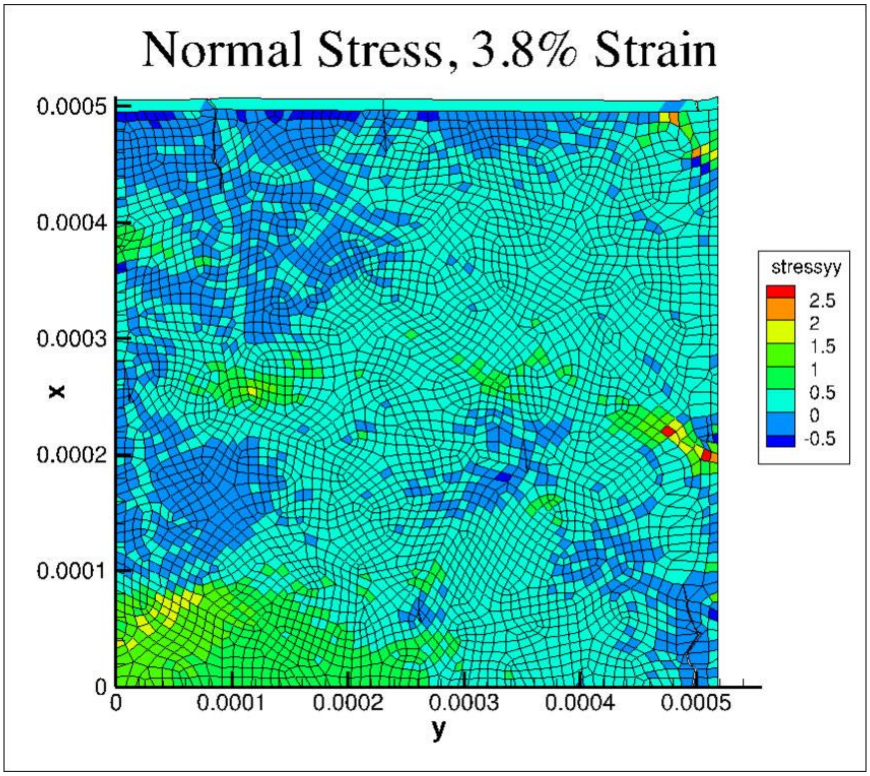

Figure 6.3: **Stress levels normalized by yield stress of constituents, post fracture.**

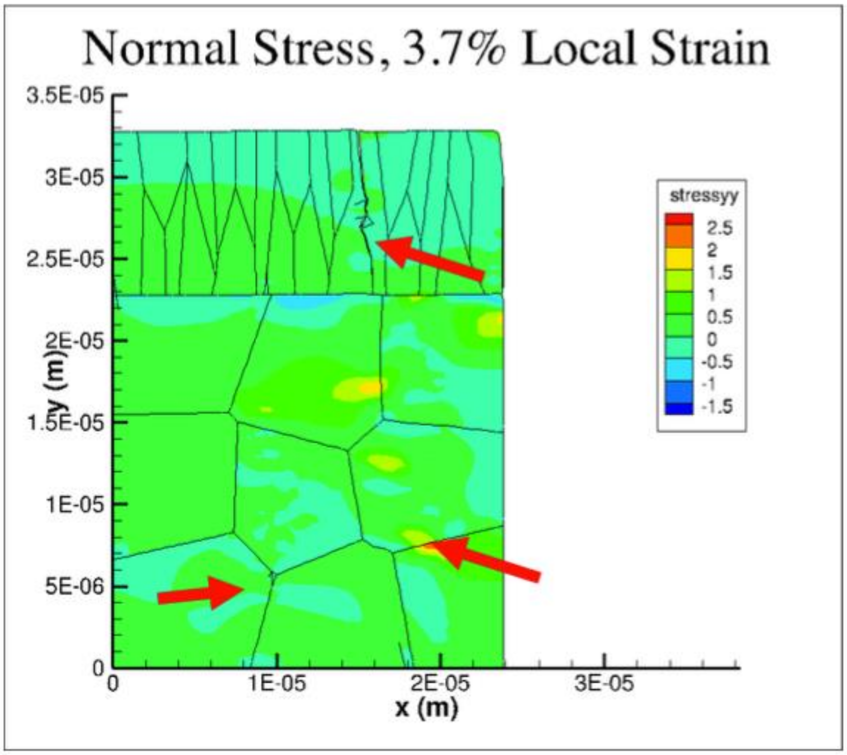

Figure 6.4: **Crack propagation in Cr coating and initiation sites in grain boundaries.** Stress levels are normalized by the yield stress of the constituents.

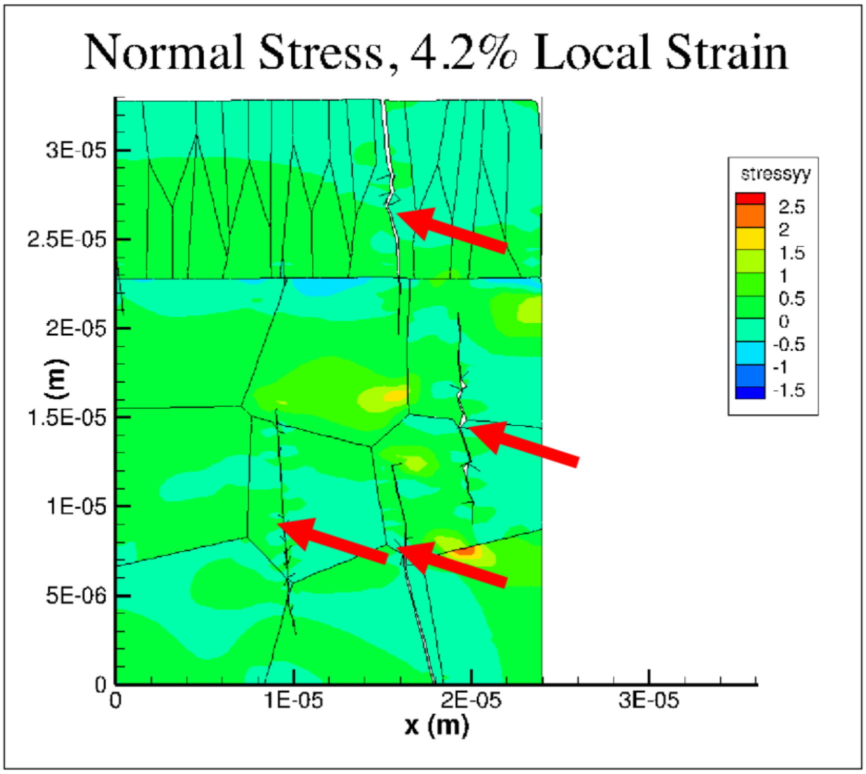

Figure 6.5: **Further crack propagation at 4.2% strain.** Stress levels are normalized by the yield stresses of the constituents.

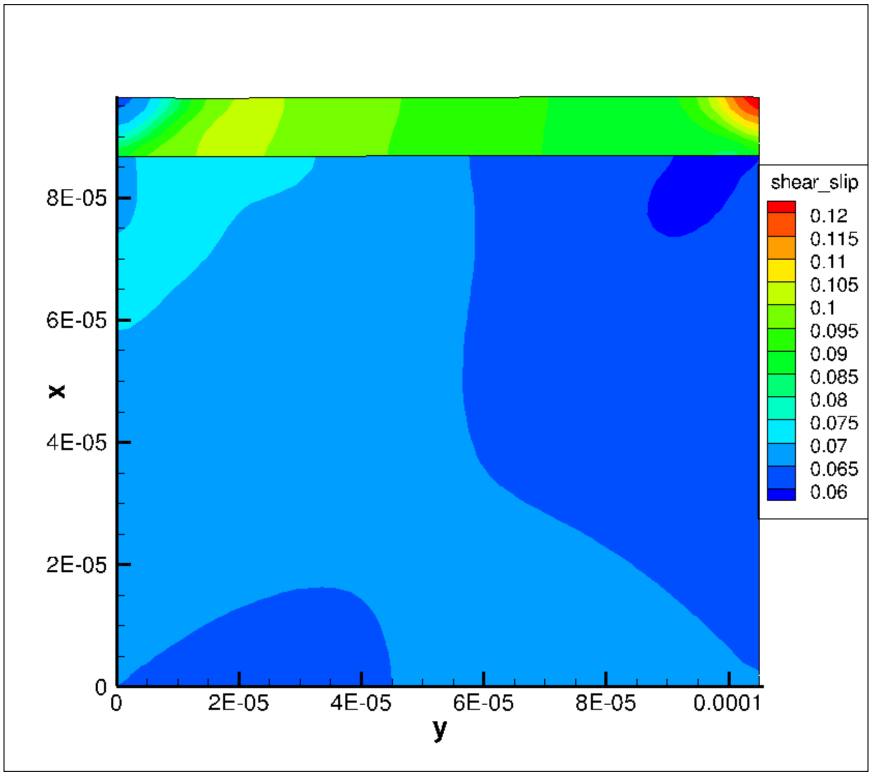

Figure 6.6: **Shear slip comparison in an idealized representation of chromium coated zircalloy.**

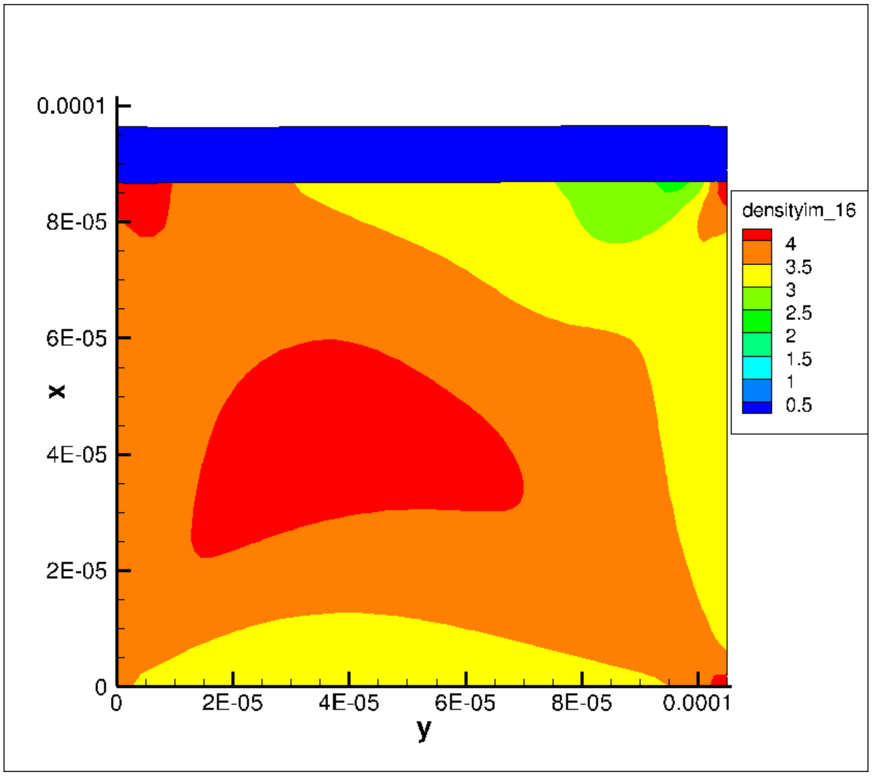

Figure 6.7: **Normalized pyramidal <c+a> (0 $\bar{1}$ 1 1) [$\bar{1}$ 2 $\bar{1}$ 3] immobile slip system activation**. Uneven activation is indicated at the interface with chromium coating and greater dislocation activity on the interior of the zircalloy grain.

CHAPTER 7: RECOMMENDATIONS FOR FUTURE RESEARCH

The following recommendations are suggested for future research:

1. **Develop a link between FEM and experimental electron backscatter diffraction (EBSD) measurements:** Develop databases using FEM meshes directly from EBSD measurements, which could provide new experimental databases directly related to FEM domains. In this manner, a mesh's material fingerprint classification would be derived after the simulation, as opposed to developing a simulation based on a material fingerprint. Difficulties in mesh generation and image classification would need to be addressed, in addition to issues with the computational burden of simulating structures with such a high level of detail. Also, adequately characterizing a highly parametric solution space would require relatively large amounts of data.
2. **Thermo-mechanical behavior as a material fingerprint parameter:** Temperature influences the thermo-mechanical response of hydrided zirconium alloy systems, and the inclusion of temperature as a material parameter could provide insight into hydrided zirconium alloy performance in critical scenarios, such as loss of coolant accidents (LOCA) and high temperature irradiation.
3. **Statistical characterization of crack propagation:** The transition from crack propagation to material failure occurs shortly after crack initiation. Quantitatively characterizing the crack propagation by failure probabilities and ROMs, may help to develop improved materials that are resistant to failure.
4. **Incorporation of twinning in hcp crystal structure:** HCP materials exhibit twinning as a part of their dominant deformation mechanism. A deformation-based

criterion for generating localized twinned hcp matrix material could shed further insight into the hcp material response as it relates to failure.

5. **Extension to other multiphase materials:** The methods developed in this work were purposefully created such that they could be applied to different multiphase, multi-component, or heterogeneous materials to develop verified and validated representations of fracture. These methods could also be used to characterize defects in additively manufactured (AM) materials, semi-coherent body centered cubic (bcc) hydrides in zirconium systems, and viscoelastic systems.
6. **3-D microstructural dynamic models:** A 3-D representation would provide for more fidelity in modeling hydrided systems, particularly in effects related to transient effects and crack tunneling. Accurately modeling these features could come at greater computational cost, and voxel-based representations of material structure may be necessary to develop large databases of material models.

REFERENCES

[1] A. T. Motta *et al.*, "Hydrogen in zirconium alloys: A review," *Journal of Nuclear Materials*, vol. 518, May 2019, doi: 10.1016/j.jnucmat.2019.02.042.

[2] J. Bair, M. Asle Zaeem, and M. Tonks, "A review on hydride precipitation in zirconium alloys," *Journal of Nuclear Materials*, vol. 466, pp. 12–20, Nov. 2015, doi: 10.1016/j.jnucmat.2015.07.014.

[3] B. W. Leitch and M. P. Puls, "Finite element calculations of the accommodation energy of a misfitting precipitate in an elastic-plastic matrix," *Metallurgical Transactions A*, vol. 23, no. 3, Mar. 1992, doi: 10.1007/BF02675557.

[4] R. Birch, S. Wang, V. S. Tong, and T. B. Britton, "The effect of cooling rate and grain size on hydride microstructure in Zircaloy-4," *Journal of Nuclear Materials*, vol. 513, Jan. 2019, doi: 10.1016/j.jnucmat.2018.11.011.

[5] A. Pshenichnikov, J. Stuckert, and M. Walter, "Hydride precipitation, fracture and plasticity mechanisms in pure zirconium and Zircaloy-4 at temperatures typical for the postulated loss-of-coolant accident," *Nuclear Engineering and Design*, vol. 301, May 2016, doi: 10.1016/j.nucengdes.2016.03.024.

[6] S.-Q. Shi and M. P. Puls, "Fracture strength of hydride precipitates in Zr–2.5Nb alloys," *Journal of Nuclear Materials*, vol. 275, no. 3, Nov. 1999, doi: 10.1016/S0022-3115(99)00132-4.

[7] A. T. Motta and L.-Q. Chen, "Hydride Formation in Zirconium Alloys," *JOM*, vol. 64, no. 12, pp. 1403–1408, Dec. 2012, doi: 10.1007/s11837-012-0479-x.

[8] H.-H. Hsu, M.-F. Chiang, and Y.-C. Chen, "The influence of hydride on fracture toughness of recrystallized Zircaloy-4 cladding," *Journal of Nuclear Materials*, vol. 447, no. 1–3, Apr. 2014, doi: 10.1016/j.jnucmat.2013.12.028.

[9] T. Kubo, Y. Kobayashi, and H. Uchikoshi, "Determination of fracture strength of δ-zirconium hydrides embedded in zirconium matrix at high temperatures," *Journal of Nuclear Materials*, vol. 435, no. 1–3, Apr. 2013, doi: 10.1016/j.jnucmat.2012.12.045.

[10] A. Gopalan *et al.*, "Effect of radial hydride on room temperature fracture toughness of Zr-2.5Nb pressure tube material," *Journal of Nuclear Materials*, vol. 544, Feb. 2021, doi: 10.1016/j.jnucmat.2020.152681.

[11] H.-H. Hsu and L.-W. Tsay, "Effect of hydride orientation on fracture toughness of Zircaloy-4 cladding," *Journal of Nuclear Materials*, vol. 408, no. 1, Jan. 2011, doi: 10.1016/j.jnucmat.2010.10.068.

[12] A. T. Motta *et al.*, "Hydrogen in zirconium alloys: A review. Journal of Nuclear Materials," vol. 518, pp. 440–460, 2019.

[13] R. Birch, S. Wang, V. Tong, and B. Britton, "Short communication: The effect of cooling rate and grain size on hydride microstructure in Zircaloy-4," *arXiv*, vol. 513, pp. 221–225, Jan. 2018.

[14] M. R. Louthan and R. P. Marshall, "Control of hydride orientation in zircaloy," *Journal of Nuclear Materials*, vol. 9, no. 2, pp. 170–184, Oct. 1963, doi: 10.1016/0022-3115(63)90132-6.

[15] M. Leger and A. Donner, "The effect of stress on orientation of hydrides in zirconium alloy pressure tube materials," *Canadian Metallurgical Quarterly*, vol. 24, no. 3, pp. 235–243, Jul. 1985, doi: 10.1179/cmq.1985.24.3.235.

[16] Y. Mishima and T. Okubc, “Effect of thermal cycling on the stress orientation and circumferential ductility in Zircaloy-2,” *Canadian Metallurgical Quarterly*, vol. 11, no. 1, pp. 157–164, Jan. 1972, doi: 10.1179/cmq.1972.11.1.157.
[17] J.-S. Kim, T.-H. Kim, D.-H. Kook, and Y.-S. Kim, “Effects of hydride morphology on the embrittlement of Zircaloy-4 cladding,” *Journal of Nuclear Materials*, vol. 456, Jan. 2015, doi: 10.1016/j.jnucmat.2014.09.025.
[18] O. N. Pierron, D. A. Koss, A. T. Motta, and K. S. Chan, “The influence of hydride blisters on the fracture of Zircaloy-4,” *Journal of Nuclear Materials*, vol. 322, no. 1, Oct. 2003, doi: 10.1016/S0022-3115(03)00299-X.
[19] J. L. Feng, A. G. Varias, and Y. K. Sui, “Finite element analysis for steady-state hydride-induced fracture in metals by composite model,” *International Journal of Solids and Structures*, vol. 43, no. 7–8, pp. 2174–2192, 2006, doi: 10.1016/j.ijsolstr.2005.05.001.
[20] S. Q. Shi and M. P. Puls, “Criteria for fracture initiation at hydrides in zirconium alloys I. Sharp crack tip,” *Journal of Nuclear Materials*, vol. 208, no. 3, pp. 232–242, 1994, doi: 10.1016/0022-3115(94)90332-8.
[21] R. K. Sharma, A. K. Bind, G. Avinash, R. N. Singh, A. Tewari, and B. P. Kashyap, “Effect of radial hydride fraction on fracture toughness of CWSR Zr-2.5%Nb pressure tube material between ambient and 300 °C temperatures,” *Journal of Nuclear Materials*, vol. 508, pp. 546–555, 2018, doi: 10.1016/j.jnucmat.2018.06.003.
[22] P. A. Raynaud, D. A. Koss, and A. T. Motta, “Crack growth in the through-thickness direction of hydrided thin-wall Zircaloy sheet,” *Journal of Nuclear Materials*, vol. 420, no. 1–3, pp. 69–82, Jan. 2012, doi: 10.1016/j.jnucmat.2011.09.005.
[23] J. Li *et al.*, “Effect of hydride precipitation on the fatigue cracking behavior in a zirconium alloy cladding tube,” *International Journal of Fatigue*, vol. 129, p. 105230, Dec. 2019, doi: 10.1016/j.ijfatigue.2019.105230.
[24] L. Thuinet, A. Legris, L. Zhang, and A. Ambard, “Mesoscale modeling of coherent zirconium hydride precipitation under an applied stress,” *Journal of Nuclear Materials*, vol. 438, no. 1–3, pp. 32–40, Jul. 2013, doi: 10.1016/j.jnucmat.2013.02.034.
[25] T. W. Heo, K. B. Colas, A. T. Motta, and L.-Q. Chen, “A phase-field model for hydride formation in polycrystalline metals: Application to δ-hydride in zirconium alloys,” *Acta Materialia*, vol. 181, pp. 262–277, Dec. 2019, doi: 10.1016/j.actamat.2019.09.047.
[26] Y. Udagawa, M. Yamaguchi, H. Abe, N. Sekimura, and T. Fuketa, “Ab initio study on plane defects in zirconium–hydrogen solid solution and zirconium hydride,” *Acta Materialia*, vol. 58, no. 11, pp. 3927–3938, Jun. 2010, doi: 10.1016/j.actamat.2010.03.034.
[27] R. Liu, A. Mostafa, and Z. Liu, “Modeling of structural failure of Zircaloy claddings induced by multiple hydride cracks,” *International Journal of Fracture*, vol. 213, no. 2, pp. 171–191, Oct. 2018, doi: 10.1007/s10704-018-0312-9.
[28] A. G. Varias and A. R. Massih, “Hydride-induced embrittlement and fracture in metals - Effect of stress and temperature distribution,” *Journal of the Mechanics and Physics of Solids*, vol. 50, no. 7, pp. 1469–1510, 2002, doi: 10.1016/S0022-5096(01)00117-X.
[29] L. O. Jernkvist, “Multi-field modelling of hydride forming metals Part II: Application to fracture,” *Computational Materials Science*, vol. 85, Apr. 2014, doi: 10.1016/j.commatsci.2013.11.035.

[30] S. Suman, Mohd. K. Khan, M. Pathak, and R. N. Singh, "3D simulation of hydride-assisted crack propagation in zircaloy-4 using XFEM," *International Journal of Hydrogen Energy*, vol. 42, no. 29, Jul. 2017, doi: 10.1016/j.ijhydene.2017.04.163.
[31] P. A. T. Olsson, K. Kese, M. Kroon, and A.-M. A. Holston, "Ab initio-based fracture toughness estimates and transgranular traction-separation modelling of zirconium hydrides," *Modelling and Simulation in Materials Science and Engineering*, vol. 23, no. 4, Jun. 2015, doi: 10.1088/0965-0393/23/4/045015.
[32] I. Mohamed, T. Hasan, and M. A. Zikry, "Thermomechanical Microstructural Predictions of Fracture Nucleation of Zircaloy-4 Alloys With δ and ε Hydride Distributions," *Journal of Engineering Materials and Technology*, vol. 144, no. 1, Jan. 2022, doi: 10.1115/1.4051687.
[33] Q. Wu and M. A. Zikry, "Microstructural modeling of crack nucleation and propagation in high strength martensitic steels," *International Journal of Solids and Structures*, vol. 51, no. 25–26, pp. 4345–4356, Dec. 2014, doi: 10.1016/j.ijsolstr.2014.08.021.
[34] H. Salmenjoki, M. J. Alava, and L. Laurson, "Machine learning plastic deformation of crystals," *Nature Communications*, vol. 9, no. 1, 2018, doi: 10.1038/s41467-018-07737-2.
[35] A. Hunter *et al.*, "Reduced-order modeling through machine learning and graph-theoretic approaches for brittle fracture applications," *Computational Materials Science*, vol. 157, pp. 87–98, 2019, doi: 10.1016/j.commatsci.2018.10.036.
[36] Z. Nie, H. Jiang, and L. B. Kara, "Stress field prediction in cantilevered structures using convolutional neural networks," *Journal of Computing and Information Science in Engineering*, vol. 20, no. 1, 2020, doi: 10.1115/1.4044097.
[37] Z. Wang and Z. Zhang, "A mesh-free method for interface problems using the deep learning approach," *Journal of Computational Physics*, vol. 400, 2020, doi: 10.1016/j.jcp.2019.108963.
[38] R. J. Asaro and J. R. Rice, "Strain localization in ductile single crystals," *Journal of the Mechanics and Physics of Solids*, vol. 25, no. 5, pp. 309–338, Oct. 1977, doi: 10.1016/0022-5096(77)90001-1.
[39] M. A. Zikry, "An accurate and stable algorithm for high strain-rate finite strain plasticity," *Computers and Structures*, vol. 50, no. 3, pp. 337–350, 1994, doi: 10.1016/0045-7949(94)90004-3.
[40] M. A. A. Zikry and M. Kao, "Inelastic microstructural failure mechanisms in crystalline materials with high angle grain boundaries," *Journal of the Mechanics and Physics of Solids*, vol. 44, no. 11, pp. 1765–1798, Nov. 1996, doi: 10.1016/0022-5096(96)00049-X.
[41] P. Shanthraj and M. A. Zikry, "Dislocation density evolution and interactions in crystalline materials," *Acta Materialia*, vol. 59, no. 20, pp. 7695–7702, Dec. 2011, doi: 10.1016/j.actamat.2011.08.041.
[42] P. Franciosi, M. Berveiller, and A. Zaoui, "Latent hardening in copper and aluminium single crystals," *Acta Metallurgica*, vol. 28, no. 3, pp. 273–283, Mar. 1980, doi: 10.1016/0001-6160(80)90162-5.
[43] B. Devincre, T. Hoc, and L. Kubin, "Dislocation Mean Free Paths and Strain Hardening of Crystals," *Science (1979)*, vol. 320, no. 5884, pp. 1745–1748, Jun. 2008, doi: 10.1126/science.1156101.
[44] S. Ziaei and M. A. Zikry, "Modeling the Effects of Dislocation–Density Interaction, Generation, and Recovery on the Behavior of H.C.P. Materials," *Metallurgical and*

Materials Transactions A: Physical Metallurgy and Materials Science, vol. 46, no. 10, pp. 4478–4490, Oct. 2015, doi: 10.1007/s11661-014-2635-0.

[45] T. Vegge, T. Rasmussen, T. Leffers, O. B. Pedersen, and K. W. Jacobsen, "Determination of the of Rate Cross Slip of Screw Dislocations," *Physical Review Letters*, vol. 85, no. 18, pp. 3866–3869, Oct. 2000, doi: 10.1103/PhysRevLett.85.3866.

[46] S. Ziaei, Q. Wu, and M. A. Zikry, "Orientation relationships between coherent interfaces in hcp-fcc systems subjected to high strain-rate deformation and fracture modes," *Journal of Materials Research*, vol. 30, no. 15, pp. 2348–2359, 2015, doi: 10.1557/jmr.2015.207.

[47] K. UNE, K. NOGITA, S. ISHIMOTO, and K. OGATA, "Crystallography of Zirconium Hydrides in Recrystallized Zircaloy-2 Fuel Cladding by Electron Backscatter Diffraction," *Journal of Nuclear Science and Technology*, vol. 41, no. 7, pp. 731–740, Jul. 2004, doi: 10.1080/18811248.2004.9715540.

[48] Z. Guo, C. S. Lee, and J. W. Morris, "On coherent transformations in steel," *Acta Materialia*, vol. 52, no. 19, pp. 5511–5518, Nov. 2004, doi: 10.1016/j.actamat.2004.08.011.

[49] Q. Wu and M. A. Zikry, "Microstructural modeling of crack nucleation and propagation in high strength martensitic steels," *International Journal of Solids and Structures*, vol. 51, no. 25–26, Dec. 2014, doi: 10.1016/j.ijsolstr.2014.08.021.

[50] D. M. Bond and M. A. Zikry, "Differentiating between intergranular and transgranular fracture in polycrystalline aggregates," *Journal of Materials Science*, vol. 53, no. 8, pp. 5786–5798, Apr. 2018, doi: 10.1007/s10853-017-1847-2.

[51] M. A. Zikry, "An accurate and stable algorithm for high strain-rate finite strain plasticity," *Computers & Structures*, vol. 50, no. 3, pp. 337–350, Feb. 1994, doi: 10.1016/0045-7949(94)90004-3.

[52] D. P. Flanagan and T. Belytschko, "A uniform strain hexahedron and quadrilateral with orthogonal hourglass control," *International Journal for Numerical Methods in Engineering*, vol. 17, no. 5, pp. 679–706, May 1981, doi: 10.1002/nme.1620170504.

[53] P. Virtanen *et al.*, "SciPy 1.0: fundamental algorithms for scientific computing in Python," *Nature Methods*, vol. 17, no. 3, pp. 261–272, Mar. 2020, doi: 10.1038/s41592-019-0686-2.

[54] F. Pedregosa *et al.*, "Scikit-learn: Machine Learning in Python," *Journal of Machine Learning Research*, vol. 12, no. 85, pp. 2825–2830, 2011, [Online]. Available: http://jmlr.org/papers/v12/pedregosa11a.html

[55] M. D. Morris, "Factorial Sampling Plans for Preliminary Computational Experiments," *Technometrics*, vol. 33, no. 2, p. 161, May 1991, doi: 10.2307/1269043.

[56] J. Herman and W. Usher, "SALib: An open-source Python library for Sensitivity Analysis," *The Journal of Open Source Software*, vol. 2, no. 9, p. 97, Jan. 2017, doi: 10.21105/joss.00097.

[57] T. M. Hatem and M. A. Zikry, "Modeling of Lath Martensitic Microstructures and Failure Evolution in Steel Alloys," *Journal of Engineering Materials and Technology*, vol. 131, no. 4, Oct. 2009, doi: 10.1115/1.3183780.

[58] M. M. A. Zikry, "Modeling of the microstructural behavior of hydrided zirconium alloys," *Computational Mechanics*, 2021, doi: 10.1007/s00466-020-01970-7.

[59] M. A. Vicente Alvarez, J. R. Santisteban, P. Vizcaíno, G. Ribárik, and T. Ungar, "Quantification of dislocations densities in zirconium hydride by X-ray line profile

analysis," *Acta Materialia*, vol. 117, pp. 1–12, Sep. 2016, doi: 10.1016/j.actamat.2016.06.058.

[60] K. I. Elkhodary and M. A. Zikry, "Dynamic crack nucleation, propagation, and interactions with crystalline secondary phases in aluminum alloys subjected to large deformations," *Philosophical Magazine*, vol. 92, no. 32, pp. 3920–3949, Nov. 2012, doi: 10.1080/14786435.2012.700126.

[61] Tin Kam Ho, "Random decision forests," in *Proceedings of 3rd International Conference on Document Analysis and Recognition*, pp. 278–282. doi: 10.1109/ICDAR.1995.598994.

[62] X. Zhang, M. Trame, L. Lesko, and S. Schmidt, "Sobol Sensitivity Analysis: A Tool to Guide the Development and Evaluation of Systems Pharmacology Models," *CPT: Pharmacometrics & Systems Pharmacology*, vol. 4, no. 2, pp. 69–79, Feb. 2015, doi: 10.1002/psp4.6.

[63] C. Tang, M. Stueber, H. J. Seifert, and M. Steinbrueck, "Protective coatings on zirconium-based alloys as accident-tolerant fuel (ATF) claddings," *Corrosion Reviews*, vol. 35, no. 3, pp. 141–165, Aug. 2017, doi: 10.1515/corrrev-2017-0010.

[64] J. C. Brachet *et al.*, "On-Going studies at CEA on chromium coated zirconium based nuclear fuel claddings for enhanced accident tolerant LWRS fuel," 2015.